Double-energy Double-velocity Measurement System for Fission Fragments and Its Application

Ikuo Kanno

Double-energy Double-velocity Measurement System for Fission Fragments and Its Application

1987

Ikuo Kanno

Double-energy Double-velocity Measurement System for Fission Fragments and its Application

Ikuo Kanno

A new system of double-energy double-velocity (DEDV) measurement for fission fragments has been developed. In this system, the energies of fission fragments are measured by silicon surface barrier detectors (SSB) and the velocities by the time-of-flight (TOF) method utilizing thin film detectors (TFD) as start detectors and SSBs as stop detectors of TOF. Theoretical and experimental studies on TFDs and SSBs have been performed before the construction of the DEDV measurement system.

The TFD consists of a thin plastic scintillator film and light guide. The author proposes a new model of the luminescence production in a scintillator film. This model takes into account the thickness of the scintillator film and uses only one parameter. The calculated TFD response to charged particles shows good agreement with other experiments The dependence of the TFD response to the thickness of the scintillator film has been studied experimentally and analyzed by the luminescence production model. The results of this analysis shows the validity of the luminescence production model.

As a charged particle detector, the SSB has many merits. However, heavy ion measurements exposed two demerits of SSBs; pulse height defect and plasma delay. The recombination effect is the main effect of the pulse height defect. The recombination effect and the plasma delay are caused by the plasma column filling with dense electron-hole pairs. For an explanation of these phenomena, models of the formation and erosion of the plasma column are considered. The radius and the electron-hole density of the plasma column have been described only qualitatively and the cause of the plasma

column erosion has not been discussed by other researchers. With a model of the plasma column formation, the volume, length, radius and electron-hole density of the plasma column are calculated. In the model of the erosion of the plasma column, the cause is attributed to the change of the electric quality of the plasma column. The electric field strength inside the plasma column is determined as a function of time. The plasma delay derived from this model explains other author's experiments fairly well. The recombination effect should be calculated as a product of the recombination rate and the plasma delay. However, it is not practicable in this stage, because of the lack of data. As a practical method for the estimation of the recombination effect, two parameters concerned with the electron-hole density and surface area of the plasma column are proposed. With these parameters, the recombination effect is predicted well.

The time resolution of the DEDV measurement system using TFDs and SSBs was 133ps. As an application of this system, the DEDV measurement for the thermal neutron induced fission of ^{233}U has been carried out at the super mirror neutron guide tube facility of Kyoto University Reactor (KUR) The energy and velocity of each fission fragment have been stored on magnetic disk event by event in a list mode. The analyzed results of masses, energies and velocities of light and heavy fragments agree well with other authors' works. The value of the total neutron emission number is 2.53 and shows good agreement within experimental error, with the JENDL-2 value, 2.49. The light fragment shows a slightly greater number of neutrons emitted than the other works. This suggests the possibility of larger deformation of lights fragment at the scission point

The DEDV measurement system and the data stored on magnetic disk are useful for the study of fission phenomena. By utilizing this system and data, the fission barrier shape and the deformation state of fission fragments at the scission point will be studied efficiently and precisely.

Contents

1. Introduction

1.1 History of the research of nuclear fission

Nuclear fission was discovered by Hahn and Strassmann[1] 50 years ago. The splitting of nucleus into two fragments makes this reaction completely distinct from others. In Fig.1.1, the fission process is illustrated according to the manner of Weinberg *et al.*[2]. Upon capturing a neutron, a fissile nucleus is excited and deformed. During this stage, the Coulomb repulsion force encourages the deformation, while the nuclear surface tension resists it. When the Coulomb force surpasses the nuclear surface tension, the fissioning nucleus breaks into two fragments This break is called scission. By this stage, the two fragments have accelerated to 90% of their final velocities. After scission, the two fragments de-excite rapidly by emitting prompt neutrons in 10^{-17}s and prompt gamma rays in 10^{-14}s.

For application of nuclear fission, precise study of the phenomenon is required. Soon after the discovery of nuclear fission, researchers discovered both the large amount of energy it releases (about 200MeV), and its emission of neutrons, which permits neutron chain reactions. In 1942, the first pile was constructed at the University of Chicago by E. Fermi as the beginning of nuclear reactors. Today, about a quarter of the electricity of Japan is produced by nuclear power reactors.

For the design of nuclear reactors, various data on the fission phenomena are needed. The released energy in one fission event is important for the estimation of the thermal power of nuclear reactor. The mass distribution of the fission fragments is indispensable for the calculation of the decay heat and radioactivity of fission product. For criticality and fuel cycle evaluations to be made, the value of fission neutron yields must be measured.

In the same year as the discovery of nuclear fission, Bohr

and Wheeler[3] performed the first theoretical analysis on it. They regarded the fissioning nucleus as a liquid drop (liquid drop model) and proposed a fission barrier. This fission barrier was calculated by adding the Coulomb and surface tension potentials A representation of this fission potential is shown in Fig.1.2. Using this liquid drop model, the systematics of the barrier height for many fissioning nuclei could be explained to some extent.

Improvement of experimental techniques led to the discovery of shape isomers and the bunch structure of fission cross sections. The shape isomer has a high probability of spontaneous fission. The bunch structure of fission cross section is composed of narrow resonance peaks at a subthreshold energy. Strutinski[4] introduced a shell correction method to the liquid drop model and proposed a double-humped fission barrier model as shown in Fig.1.3. The peaks and wells of the double-humped model are formed by three parabolas. The curvatures, heights and depths of the parabolas have been determined by cross section data. Using this model, the lifetime of spontaneous fissions and fission cross sections were calculated successfully for many nuclides.

Unpredicted structures, however, were observed at energies just below the threshold in the neutron-induced fission cross sections of ^{230}Th and ^{232}Th. These phenomena suggested the existence of a third peak in the fission barrier. Experimental study has been carried out by Blons, *et al.*[5] to support this.

Although the structure of the fission barrier has been studied in detail, the fission process from the barrier peak (saddle) to the scission has not. In this part of the potential, the large deformation causes difficulty in determining the effective mass of the fissioning nucleus. Furthermore, still unknown is the viscosity of the nuclear matter, which affects important parameters such as the effective mass and the neck distance between two fragments at scission.

Recently, study of the process between the saddle and scission has been started with respect to the reverse process of the heavy ion fusion reaction. These two processes are, however, not the complete reverse of each other, but are misaligned as shown in Fig 1.4[6]. In the fission process, the deformation is thought to proceed from points H to S to B to C, then come into "two-fragment valley". In the heavy ion fusion reaction, two ions come from D to A and change their state to B. Berger, *et al.*[7] analyzed the process based on the Hartree-Fock-Bogolyubov method and derived a three dimensional potential surface with two valleys as shown in Fig.1.5. Their result indicates that the point of scission has a spread area, as shown by the slashed lines in the figure. This might be the reason that the kinetic and excitation energies of fission fragments have a wide spread distribution. The model which predicted the mass distribution of the fission fragments[8] introduces a distinct scission point, however. A consistent model of the fission barrier must be proposed.

With active and extensive studies on nuclear fission, many accurate data were obtained and various theories were proposed. However, the mechanism of nuclear fission is still unknown.

To understand nuclear fission, the process between the saddle and the scission should be studied extensively. The excitation energy and the deformation state of the fragments are the clues of this study The measurement of kinetic energy, velocity and the number of prompt neutrons for each fission event provide for the precise analysis of nuclear fission.

1.2 The purpose of this study

This study has been carried out to establish a system for measuring the kinetic energy and velocity of fission fragments. By means of this system, the mass number, kinetic

energy, velocity and the number of prompt neutrons are stored on a magnetic disk, event by event. The data set described above will be utilized for the mechanism study of nuclear fission.

For the measurement of the kinetic energy and velocity, the double-energy double-velocity (DEDV) method was employed Using the DEDV method, the energy and time-of-flight (TOF) of two fission fragments can be measured simultaneously. In the TOF measurement, the key problem is how to take start pulses.

The DEDV method was employed by Andritosopoulos[9] for the thermal neutron induced fission of ^{235}U. In his experiment, delta rays were converted to start pulses The delta rays were emitted from a gold foil when a fission fragment passed through it, and were focused and accelerated onto a plastic scintillator. In 1979, Patin, *et al.*[10] carried out a DEDV measurement for the $^{233}U(d,pf)$ reaction. Mueller, *et al.*[11] performed a DEDV measurement for fast neutron induced fission utilizing $^{7}Li(p,n)$ and $^{3}H(d,n)$ reactions in 1984. In the DEDV method for charged particle induced fission and fast neutron induced fission using charged particle reactions, start pulses are obtained from an accelerator. However, such start pulses can be used in neither thermal neutron induced fission nor spontaneous fission. The delta ray method of Andritosopoulos is mechanically very complex. To measure energies and velocities of the thermal neutron induced fission event, a new DEDV measurement system has been developed in this study.

This system has been designed for use in spontaneous fission events and thermal neutron induced fission events. Hence, thin film detectors have been utilized as start detectors for the TOF measurement.

1.3 Detectors used in this study

In this study, thin film detectors (TFD) were employed as start detectors for TOF and silicon surface barrier detectors (SSB) were used as energy detectors and stop detectors for TOF.

In 1970, the TFD was developed for the study of the stopping power of heavy ions[12]. It utilizes a very thin (about 1μm) plastic scintillator film through which heavy ions are able to pass. It has been used as a ΔE type detector and a timing detector for heavy ions. The author is the first to use TFDs as start detectors for DEDV measurements

The response characteristics of TFDs were studied in advance of the DEDV measurement. To determine the appropriate thickness of the thin plastic scintillator film for the DEDV measurement, the author carried out a study of the dependence of pulse height on the thickness of a scintillator film. However, there were few experiments on the dependence of pulse height on the film thickness. Concerned with the model of luminescence production, the thickness of the scintillator film was ignored. In order to predict the luminescence production for a scintillator film of arbitrary thickness, the author first made a model of luminescence production which took into account the thickness of the scintillator film. Furthermore, an experimental study on the dependence of the pulse height spectrum of the fission fragments of the spontaneous fission of ^{252}Cf was carried out.

For the measurement of the fragment energy, ionization chambers were used in early days. Since their development, silicon surface barrier detectors (SSB) have replaced ionization chambers. An SSB is easy to handle, has excellent energy response, has fast pulse rise time and can be used as a stop detector. However, SSBs show some demerits in energy response and pulse timing when used for the measurement of heavy ion like fission fragments These defects have been attributed to the high density plasma column of electron-hole

pairs formed in the silicon crystal by heavy ions. The defects of the energy response and time delay of SSB have been explained only qualitatively.

The defect of the energy response is called the pulse height defect (PHD). The PHD is thought to be caused by three mechanisms; (1) the energy loss of heavy ions in the gold SSB window, (2) the energy loss caused nuclear collisions with silicon nuclei, and (3) the energy loss caused by the recombination of the electron-hole pairs. Of these three sources, the first two have been estimated by calculations. The recombination effect, however, has been explained only qualitatively. To correct for the PHD phenomenologically, Schmitt *et al.*[13] reported an empirical formula. Still today, improved formulae have been proposed by many reseachers.

The defect in the timing property is called the plasma delay. Self shielding against external electric fields, caused by the density of electrons and holes in the plasma column, prevents their collection Many studies of this have been carried out with various incident particles. In theoretical studies, a few models of the plasma delay have been proposed. However, they cannot explain the recent results of experiments performed by Bohne, *et al.*[14], which demonstrate the new electric field strength dependence of the plasma delay.

In order to estimate the recombination effect quantitatively and to explain the electric field strength dependence of the plasma delay, the author made new models of the formation and erosion of the plasma column in an SSB. With this model of the plasma column formation, the volume, the surface area of the plasma column and the density of the electron-hole pairs can be calculated. In the model of plasma column erosion, the electric field strength of the plasma column is determined as a function of time.

1.4 Construction of this thesis

The outline of this thesis is as follows: In Chapter 2, the system of the DEDV measurement is described. In this chapter, the calibration methods for energy and time are presented. The start detector, TFD, is introduced in Chapter 3. First, the model of the luminescence production is proposed. An application of this model leads to the experiment determining the dependence of the pulse height spectrum of the ^{252}Cf spontaneous fission fragment on the thickness of the scintillator film. The recombination effect and the plasma delay are discussed in Chapter 4. Models of plasma column formation and plasma column erosion are described. Model calculations are compared with other authors' experimental results. The validity of the correction method of the PHD proposed by Schmitt, *et al* [13] is checked. In Chapter 5, the experiment giving the DEDV measurement of the ^{233}U thermal neutron induced fission fragment is described as an application of the system. The energy spectrum and the TOF spectrum of the fission fragments are shown. The mean energies and velocities of the light and heavy fragments and their deviations are calculated. The prompt neutron distribution is derived from the data taken by the DEDV measurement. In Chapter 6. some concluding remarks and studies which should be performed in the future are described.

References

1) Hahn, O. and Strassmann, F.: Naturwissenschaften, **26**, 755 (1938).
2) Weinberg, A. M. and Wigner, E. P.: "The Physical Theory of Neutron Chain Reactors", The University of Chicago Press (1958)
3) Bohr, N. and Wheeler, J. A.: Phys Rev., **56**, 426 (1939).
4) Strutinsky, V. M.: Nucl. Phys., **A95**, 420 (1967).
5) Blons, J., Mazur, C. and Paya, D.: Phys. Rev. Lett., **35**, 1749 (1975).
6) Swiatecki, W J. and Bjornholm, S. B.: Phys Rep.,**4C**, 327 (1972)
7) Berger, J. F., Girod, M. and Gogny, D : Nucl. Phys., **A428**, 23C (1984).
8) Fong, P.: "Statistical Theory of Nuclear Fission", Gordon & Breach, New York (1969).
9) Andritosopoulos, G.: Nucl. Phys., **A94** 537 (1967).
10) Patin, Y., Cierjacks, S., Lachkar, J., Sigaud, J., Haouat, G. and Cocu, F.: Nucl. Instr and Meth., **160**, 471 (1979).
11) Mueller, R., Naqvi, A. A., Kaeppeler, F. and Dickmann, F.: Phys. Rev. C, **29**, 855 (1984).
12) Muga, M. L., Burnsed, D. J , Steeger, W. E. and Taylor, H. E.: Nucl. Instr. and Meth., **83**, 135 (1970).
13) Schmitt, H. W., Gibson, W. M., Neiler, J. H., Walter, F. J. and Thomas, T. D.: "Proceedings of the Symposium on Physics and Chemistry of Fission", Salzburg, IAEA, Vienna, Vol.I, p.531 (1965)
14) Bohne, W., Galster, W., Grabisch, K. and Morgenstern, H.: Nucl. Instr. and Meth., **A240**, 145 (1985)

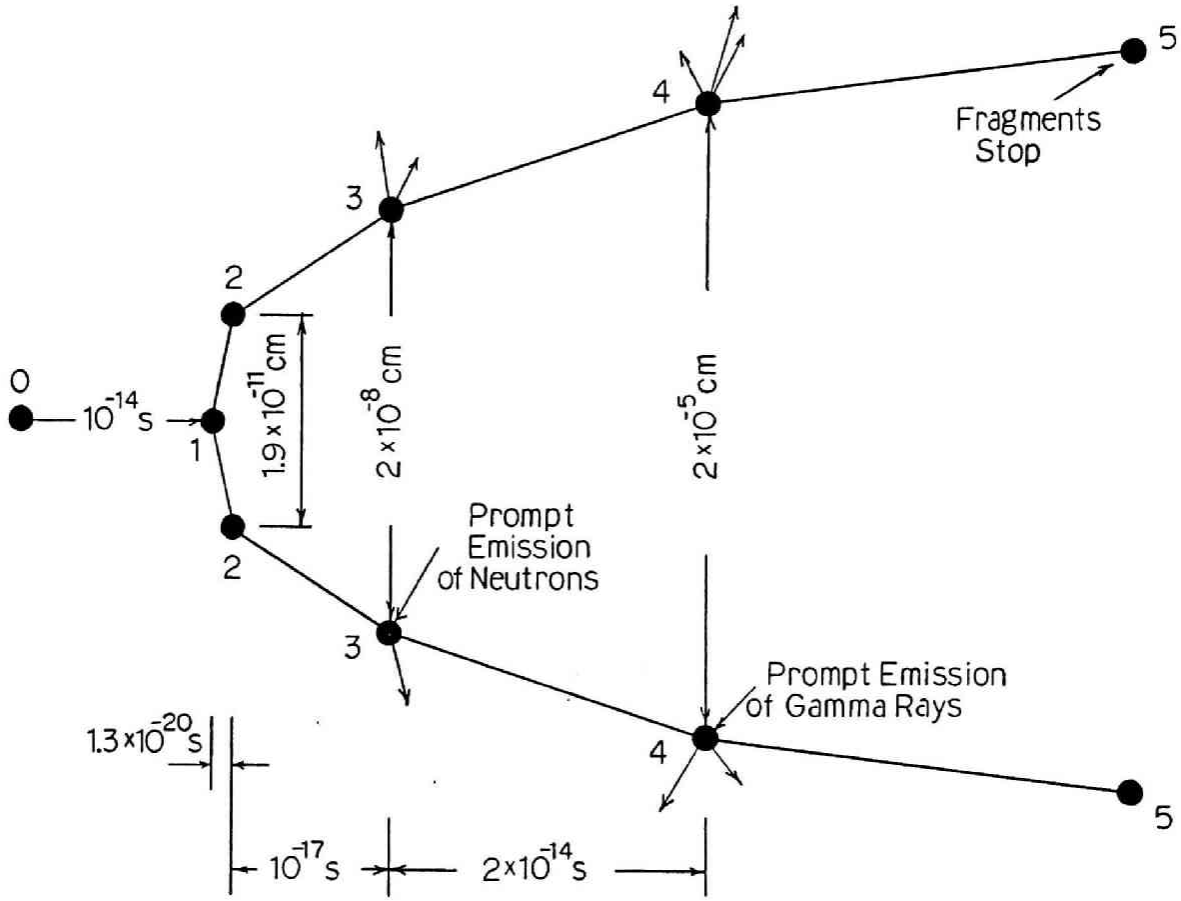

Fig.1.1 Graphic representation of the fission process The events are: 0 – Formation of the initial state, 1 – Fission (or, more specially, scission), 2 – Fragments acquire 90% of their kinetic energy, 3 – Prompt neutron emission, 4 – Prompt gamma ray emission, 5 – Fragments stop and decay by delayed processes. The horizontal scale indicates the durations of the various phases of the fission process whereas the vertical scale indicates the distance between the fission fragments. (taken from Ref.(2))

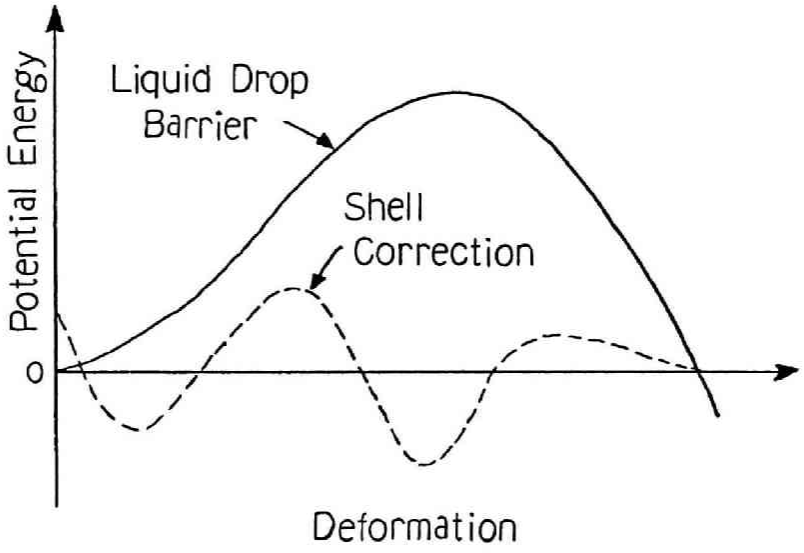

Fig.1.2 Single-humped fission barrier introduced by the liquid drop model. Dashed line shows the shell correction introduced by Strutinski.

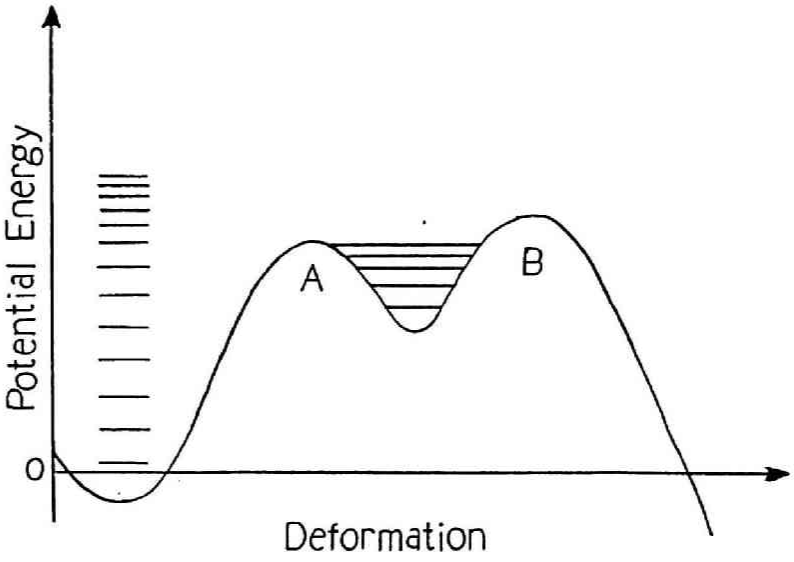

Fig.1.3 Double-humped fission barrier which was obtained by introducing the shell correction (see Fig.1.2) into the single-humped fission barrier.

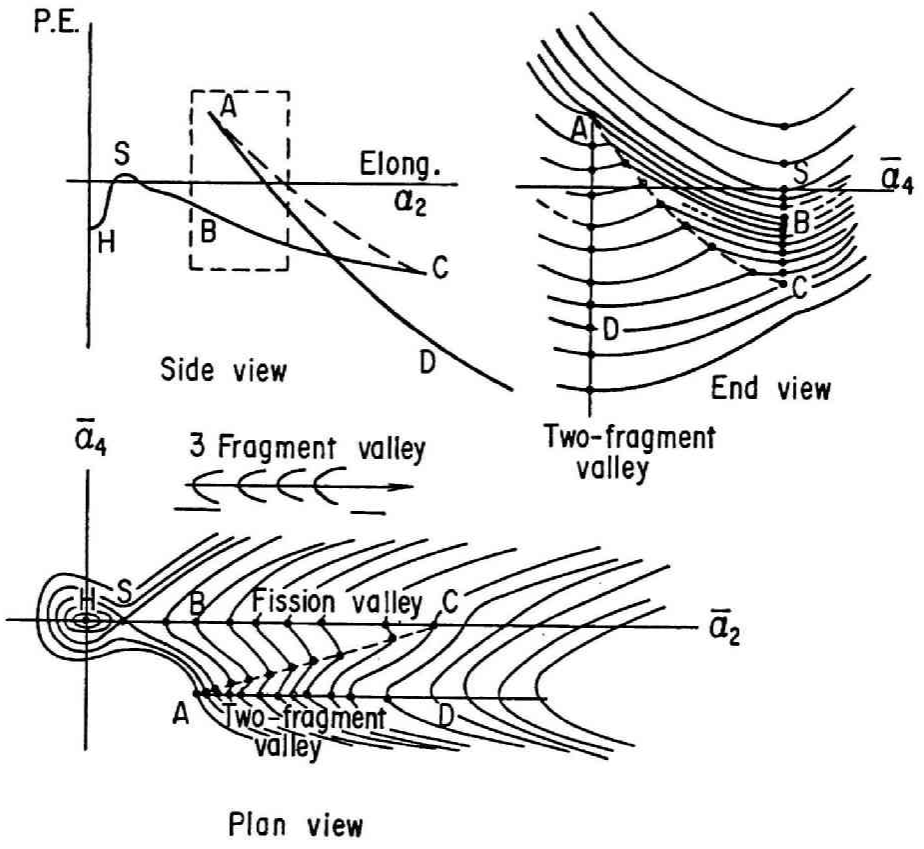

Fig.1.4 Schematic energy contour diagrams of the two-fragment-valley and the fission valley (taken from Ref.(6)).

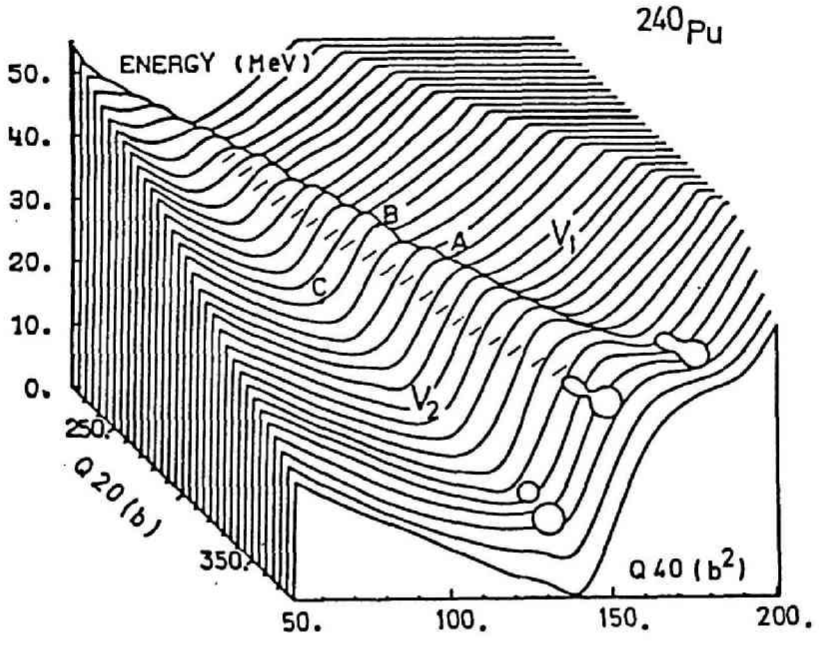

Fig.1.5 Deformation potential surface from the saddle to the scission. $\langle Q_{20} \rangle$ and $\langle Q_{40} \rangle$ are the deformation parameters for the elongation and necking-in, respectively (taken from Ref.(7)).

2. Double-energy double-velocity measurement system[1)]

2.1 Introduction

For the purpose of measuring the kinetic energy and the velocity of the fission fragment simultaneously, the double-energy double-velocity (DEDV) method, which measures the energies and velocities of both two fragments in fission event, is the most effective method.

The DEDV method was carried out by Andritosopoulos[2)] for the fragments of the thermal neutron induced fission of ^{235}U for the first time twenty years ago. He used silicon surface barrier detectors (SSB) to measure the kinetic energy of the fission fragments. The velocity of the fragment was determined by the time-of-flight (TOF) method. The SSBs were also used as stop detectors for the TOF. As a start detector for the TOF, he used the delta rays emitted from a gold foil by the fission fragment's interaction. The delta rays were accelerated, focused and finally impinged on a plastic scintillator.

Apart from the thermal neutron induced fission, Patin, *et al.*[3)] carried out the DEDV measurement for $^{233}U(d,pf)$ in 1979. In 1984, Mueller, *et al.*[4)] performed the DEDV measurement for the fast neutron induced fission of ^{235}U making use of $^{7}Li(p,n)$ and $^{2}H(d,n)$ reactions. In these two experiments, SSBs were used for energy and stop time detection. The start signals for the TOF were taken from the trigger pulse of the accelerators.

The DEDV method for charged particle induced fission and fast neutron induced fission described above cannot be applied to either thermal neutron induced fission or spontaneous fission because of the difficulty in taking start pulses The system used by Andritosopoulos can be used both for thermal neutron induced fission and for spontaneous fission. However, his start detector was large and complex. In order to make the start detector simpler and to apply the DEDV

measurement system to various fission phenomena, e.g., spontaneous fission, thermal and fast neutron induced fission and charged particle induced fission, the author chose a thin film detector as a start detector.

The thin film detector (TFD) was developed by Muga, *et al.*[5] in 1970. It makes use of a thin plastic scintillator film and has been used as a ΔE type detector[6] and timing detector[7] for heavy ions The luminescence production and its dependence on the thickness of the scintillator film were studied by the author[8),9)] and will be described in Chapter 3.

For the determination of energy and the detection of stop signals, SSBs were used in a similar fashion as other authors[2)-4)].

In this chapter, a newly developed DEDV measurement system is described.

2.2 Apparatus

2.2.1 General

The experimental chamber used in this measurement system is shown in Fig.2.1. The central part of this chamber is a 4mm thick stainless steel octagonal column which consists of eight plates 9cm in width and 20cm in height, and two octagonal plates. Each side plate has flanges for target insertion, neutron entrance and photomultiplier mounting. The target holder is set at the vertical center of the octagonal column. The cross section of this octagonal column is shown in Fig.2.2. Two photomultipliers are mounted to the octagonal column, inclined 45 degrees from the target holder. The photomultiplier is attached to an aluminum holder by chemical adhesive and the aluminum holder is made air tight with a double O-rings system. A TFD is sandwiched between two photomultipliers and coupled to them with optical grease. The thin plastic scintillator films are 3cm from the target

holder. The combination of a TFD and two photomultipliers are set on both sides of the target holder to detect the two fission fragments simultaneously.

Flight tubes are arranged on the two octagonal plates. At the end of the flight tubes, caps are attached by flanges to hold the SSBs. A maximum of three SSBs can be placed on one cap.

The evacuation tubes are three in total; one on the octagonal column and one on each flight tube. A leak valve is attached to the evacuation tube column. The air in the octagonal column and flight tubes is evacuated to about 10^{-4} Torr by a rotary pump through a high efficiency HEPA filter. In order to check the vacuum, a Geissler tube is attached next to one photomultiplier.

2.2.2 Thin film detector

A thin film detector consists of a thin plastic scintillator film and two hemicylindrical light guides with holes bored in them, as shown in Fig.2.3.

The thin plastic scintillator film is made by the following method reported by Muga, et al.[2]: A 6.0g quantity of NE102 plastic scintillator chips is added to a solution made of 50ml ethyl acetate plus 4ml amyl acetate The mixture is allowed to stand with occasional stirring until complete dissolution occurs. A thin plastic scintillator film is formed by dropping this solution onto the surface of distilled water in a photographic developing pan with a depth of a few centimeters. The scintillator film is attached by softly contacting it to the plain surface of a light guide painted with optical grease, and the TFD is completed by sandwiching the scintillator film between two light guides.

For the purpose of taking a start pulse without fail, a thick scintillator film is preferred. However, with respect to measuring an accurate fission fragment velocity, a thin plastic scintillator film is favorable because it minimizes

energy loss of the fragment. The author studied the thickness dependence of the luminescence production described in Chapter 3, and decided to use 20$\mu g/cm^2$ scintillator films. The uncertainty of the film thickness was ±10%. The light guide was 4cm in diameter and 7cm in height. A hole of 1cm diameter was bored for fragment passing. Two TFDs were set at the same distance from the target holder but on opposite sides so that each TFD could detect the fission fragments which were emitted linearly in opposite directions.

2.2.3 Silicon surface barrier detector

For the detection of the energy and stop signal for the TOF of fission fragments, silicon surface barrier detectors (SSBs) were employed. It is well known that the pulse height defect[10], and the plasma delay[11] occur when the SSB is used for heavy ion measurements like fission fragments. The author proposes new quantitative models of the phenomena described above in Chapter 4.

The SSBs were made by ORTEC (BF-030-400-60), and had sensitive area of 400mm^2. At the end of the flight tube, a maximum of three SSBs could be mounted to make the solid angle larger. In the case of mounting more than one SSBs, the output pulses of each SSB were summed. The energy spectrum of the spontaneous fission fragments of ^{252}Cf did not change visibly when the fragments were detected by three SSBs compared to the measurement with one SSB

2.2.4 Electronics

The electronic circuits used in the experiment are shown in Fig.2.4. The signal taken by each TFD was amplified by photomultipliers and preamplifiers. For the photomultipliers (HAMAMATSU R580), a voltage of 1400V was supplied by a high voltage power supply (Fluke 415B). The pulses from two TFDs were summed and fed to a timing amplifier (ORTEC 574) and

then to a constant fraction discriminator (CFD, ORTEC 473A) as a start pulse and finally to a time-to-amplitude converter (TAC, Tokyo Atomic 724-1). The pulses from the SSBs were split into timing and energy signals in the preamplifiers (ORTEC 142A). The timing signals were fed in the same way as those from the TFDs. The output signal of the CFDs were split in two. One was fed to the TAC as a stop signal and the other was fed to a coincidence circuit (ORTEC 418A) to discriminate the pulses from SSBs at both ends caused by the same fission event. The energy signals were fed to amplifiers and finally to analog-to-digital converters (ADC, ND-560). The output signals of the TACs were also fed to the ADCs. The four ADCs were gated so that they received the time and energy signals only when the two fragments were detected within 1μs of each other The four output signals from the ADCs were finally taken by the Multi-Parameter Data Acquisition System[12] developed at Research Reactor Institute, Kyoto University (KURRI). With this system, the data were stored in 1024 channels with four parameters. The data accumulated could be shown on a two parameter display with arbitrary combination of the parameters. The data were stored on a floppy disk event by event in a list mode.

2.3 Calibrations and corrections

2.3.1 Energy calibration

As described in Chapter 2.2.3, the energies of the fission fragments were measured by the SSBs. In the measurement of the energy of a heavy ion like fission fragments, it is well known that the pulse height obtained from an SSB is not proportional to the incident energy of the particle. This phenomenon is called pulse height defect and will be described in Chapter 4. As a correction method for the pulse height defect, a calibration method proposed by Schmitt, *et al.*[10]

was employed in the analysis. They assumed a mass dependent energy formula;

$$E = (a + a'm)\cdot x + b + b'm \ , \qquad (2-1)$$

where E and m are the energy and mass number of the fragment, x is the pulse height. a, a', b and b' are constants given as;

$$a = \frac{c_1}{(P_L - P_H)} \ , \qquad (2-2)$$

$$a' = \frac{c_2}{(P_L - P_H)} \ , \qquad (2-3)$$

$$b = d_1 - aP_L \ , \qquad (2-4)$$

$$b' = d_2 - a'P_L \ . \qquad (2-5)$$

In the above relations, P_L and P_H are the channel numbers of light and heavy fragment peaks, c_1, c_2, d_1 and d_2 are constants determined experimentally for each fissile They utilized ^{79,81}Br and ^{127}I ions to determine the energies corresponding to channels for heavy and light fragment peaks In the measurement of fission fragments of ^{252}Cf spontaneous fission, Schmitt, *et al.* determined the values of constants c_1, c_2, d_1 and d_2 as 24.0203, 0.03574, 89.6083 and 0.1370, respectively The validity of the calibration method of Schmitt, *et al.* will be discussed in Chapter 4.

2.3.2 Time calibration

The relation between the pulse height x, which is fed from the TAC, and the flight time T is given as;

$$T = Ax + B \ , \qquad (2-6)$$

where A and B are constants. The measurements of the flight time of the light fragments of ^{252}Cf were carried out with two flight paths, L_1 and L_2 to determine A and B. Assigning the pulse heights of the TAC which correspond to the averaged light fragments for the flight paths L_1 and L_2 as $\bar{x}_1$ and $\bar{x}_2$, respectively, we obtain the relations;

$$\frac{L_1}{\bar{v}} = A\cdot\bar{x}_1 + B \ , \qquad (2-7)$$

$$\frac{L_2}{\bar{v}} = A\cdot\bar{x}_2 + B \ , \qquad (2-8)$$

where $\bar{v}$ is the average velocity of the light fragments. With Eqs (2-7) and (2-8), B is determined;

$$B = \frac{A(L_1\bar{x}_2 - L_2\bar{x}_1)}{L_2 - L_1} . \qquad (2-9)$$

In order to deduce A, we measured another flight time of the light fragments of ^{252}Cf, $\bar{x}_3$, with the flight path L_1 employing a delay line Writing the delay time due to the cable T_d, the following relation is obtained.

$$\frac{L_1}{\bar{v}} + T_d = A\cdot\bar{x}_3 + B \ . \qquad (2-10)$$

From Eqs.(2-7) and (2-10), A is determined;

$$A = \frac{T_d}{\bar{x}_3 - \bar{x}_1} \ , \qquad (2-11)$$

A delay line of 5m was used in our measurement. The delay time due to this cable was measured with a time calibrator (ORTEC 462) and was found to be 26.302ns.

2.3.3 Time resolution

The time resolution of the TFD-SSB system was determined by the following method using 6.118MeV α particles of ^{252}Cf.

(1) Measurement of the TOF spectrum of α particles

The TOF spectrum of the α particle of ^{252}Cf was measured with a flight path of 295mm. The time corresponding to the full width at half maximum (FWHM) of the α peak was found to be,

$$\Delta t = 1.33\times10^{-10}(\mathrm{s}). \qquad (2-12)$$

(2) Determination of the energy distribution of α particles

The energy distribution of the α particles after passing through the TFD was calculated by the Bethe's formula. This distribution was caused by the uncertainty of the scintillator film thickness and was determined to be 4keV.

(3) Calculation of the time resolution

The relation between the energy resolution and the time

resolution is as follows,

$$\left|\frac{\Delta E_\alpha}{E_\alpha}\right| = 2\left|\frac{\Delta v_\alpha}{v_\alpha}\right| = 2\left|\frac{\Delta t_\alpha}{t_\alpha}\right| . \qquad (2-13)$$

The time t_α needed by the α particle for a flight path 295mm is calculated as,

$$t_\alpha = \frac{29.5}{(2E_\alpha/km_\alpha)^{1/2}} , \qquad (2-14)$$

where k is the constant 1.0365 when the length, mass, time and energy are described in cm, a.m.u., ns and MeV. Time resolution is given as,

$$\Delta t = \left\{(\Delta t_\alpha)^2 + (\Delta t_s)^2\right\}^{1/2} . \qquad (2-15)$$

Here Δt_α and Δt_s are the time resolution attributed to the uncertainty of energy loss in a scintillator film and the time resolution of this system. Δt_α is calculated using Eqs.(2-13) and (2-14) and determined to be Δt_α = 0.00561ns. With this value and Eq.(2-15), Δt_s is calculated as,

$$\Delta t_s = 1.329\times10^{-10}(\mathrm{s}). \qquad (2-16)$$

We notice here that the uncertainty of the energy loss in the scintillator film does not affect the time resolution much.

2.4 Conclusion

The DEDV measurement system using thin film detectors as start detectors was built. The use of TFD permitted the start detector to be simple. This measurement system is applicable to spontaneous fission, thermal neutron induced fission, fast neutron induced fission and charged particle induced fission. The time resolution of this system was 133ps which is between the value of Mueller, *et al.*, 15ps[4] and Patin, *et al.*, about 300ps[3]. With this system, the data on the energies and flight times of the fission fragment are stored on a magnetic disk event by event in list mode.

References

1) Kanno, I., Nakagome, Y. and Kimura, I.: J. Nucl. Sci. Technol., to be published.

2) Andritosopoulos, G.: Nucl. Phys., **A94** 537 (1967).

3) Patin, Y., Cierjacks, S., Lackar, J , Sigaud, J., Haouat,G. and Cocu,F.: Nucl. Instr. and Meth., **160**, 471 (1979).

4) Muller, R., Naqvi, A. A., Kaeppeler, F. and Dickmann, F.: Phys. Rev., **C29**, 885 (1984).

5) Muga, M. L., Burnsed, D. J., Steeger, W. E. and Taylor, H. E.: Nucl. Instr. and Meth., **83**, 135 (1970)

6) Muga, M. L.: Nucl. Instr. and Meth., **95**, 349 (1971).

7) Ettling, K. and von Witsh, W.: Nucl. Instr and Meth., **148**, 299 (1978).

8) Kanno, I. and Nakagome, Y.: Nucl Instr. and Meth., **A244**, 551 (1986).

9) Kanno, I. and Nakagome, Y.: Nucl. Instr. and Meth., **A245**, 108 (1986).

10) Schmitt, H. W., Gibson, W. M., Neiler, J. H., Walter, F. J. and Thomas, T. D.: "Proceedings of the Symposium on Physics and Chemistry of Fission", Salzburg, IAEA, Vienna, Vol.I, p.531 (1965).

11) Quaranta, A. A., Taroni, A. and Zanarini, G.: Nucl. Instr. and Meth., **72** (1969) 72.

12) Uehara, S., Seo. T., Iimura, H. and Yamada, S : Ann. Rep. Res. Reactor Inst Kyoto Univ., **18**, 178 (1985).

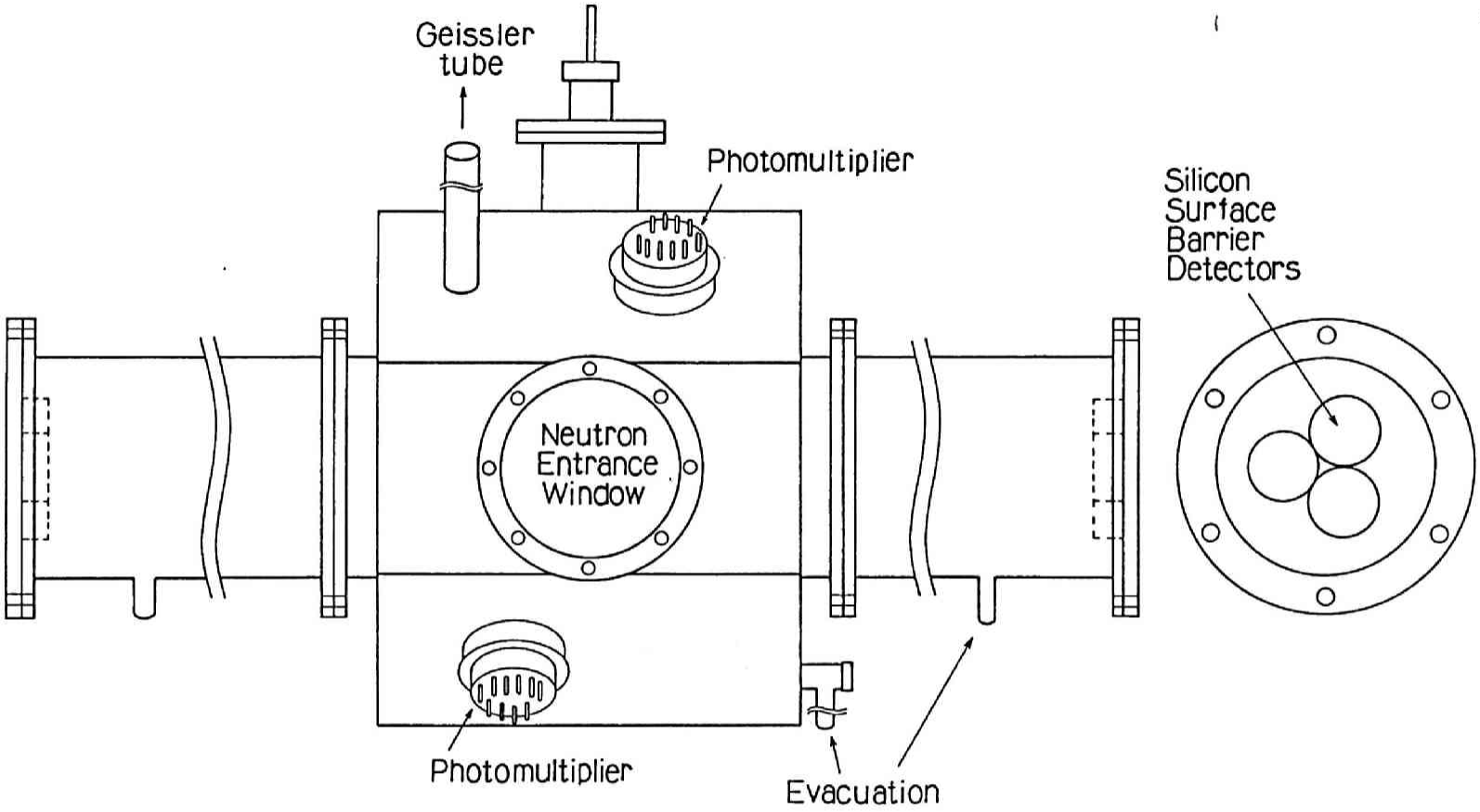

Fig.2.1 The experimental chamber. Four photomultipliers are mounted on an octagonal chamber placed at the center of the fission fragment flight tube. Two 1mm thick aluminum plates, for neutron entrance, are mounted on the chamber. At the end of the flight tube are three silicon surface barrier detectors.

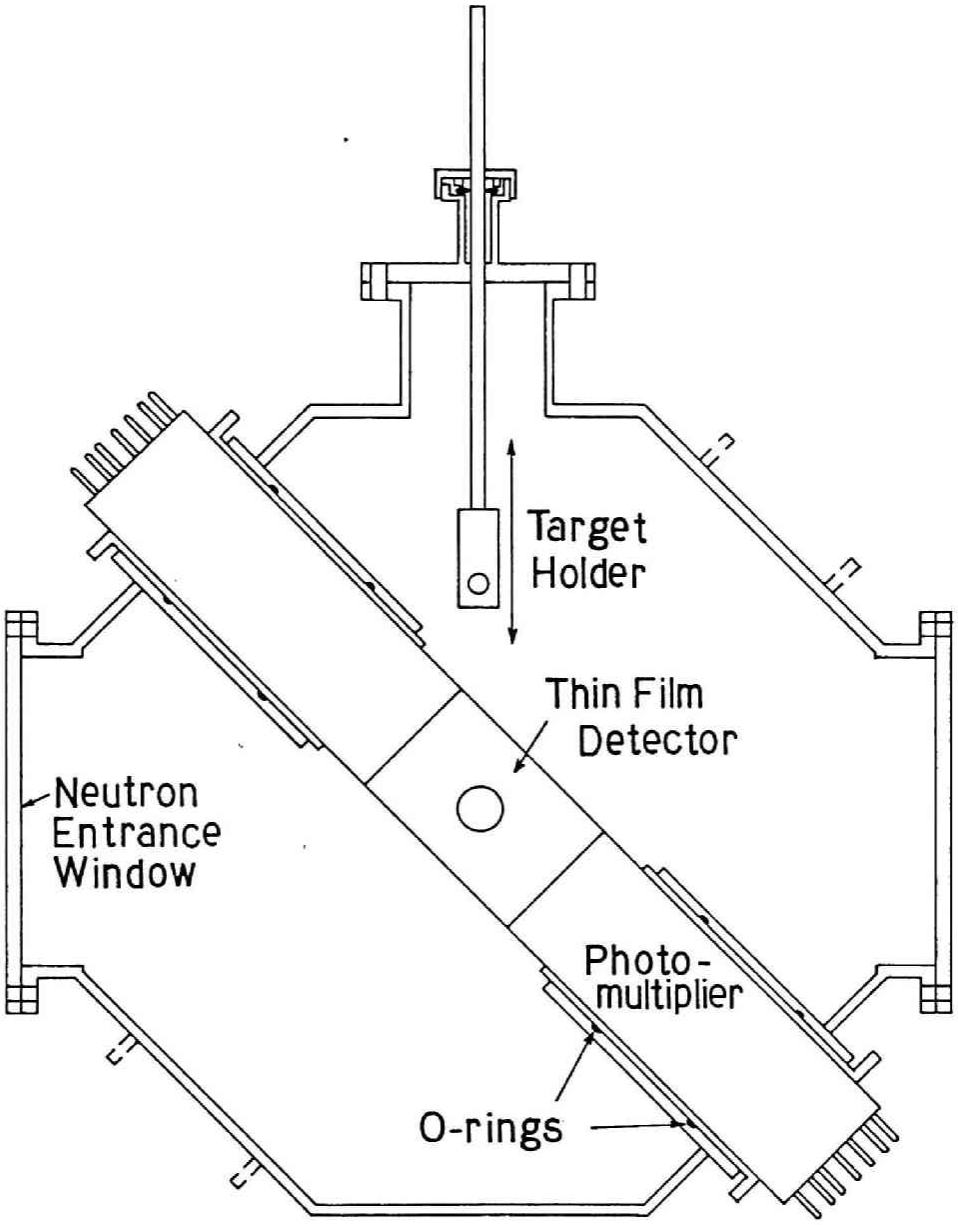

Fig.2.2 Cross section of the octagonal column. A thin film detector is placed at the center of the column between two photomultipliers. Photomultipliers are attached to an aluminum holder by chemical adhesive and the holder is made air tight by the double O-ring system. The uranium target can be moved manually Neutrons enter the chamber through an aluminum window on left side.

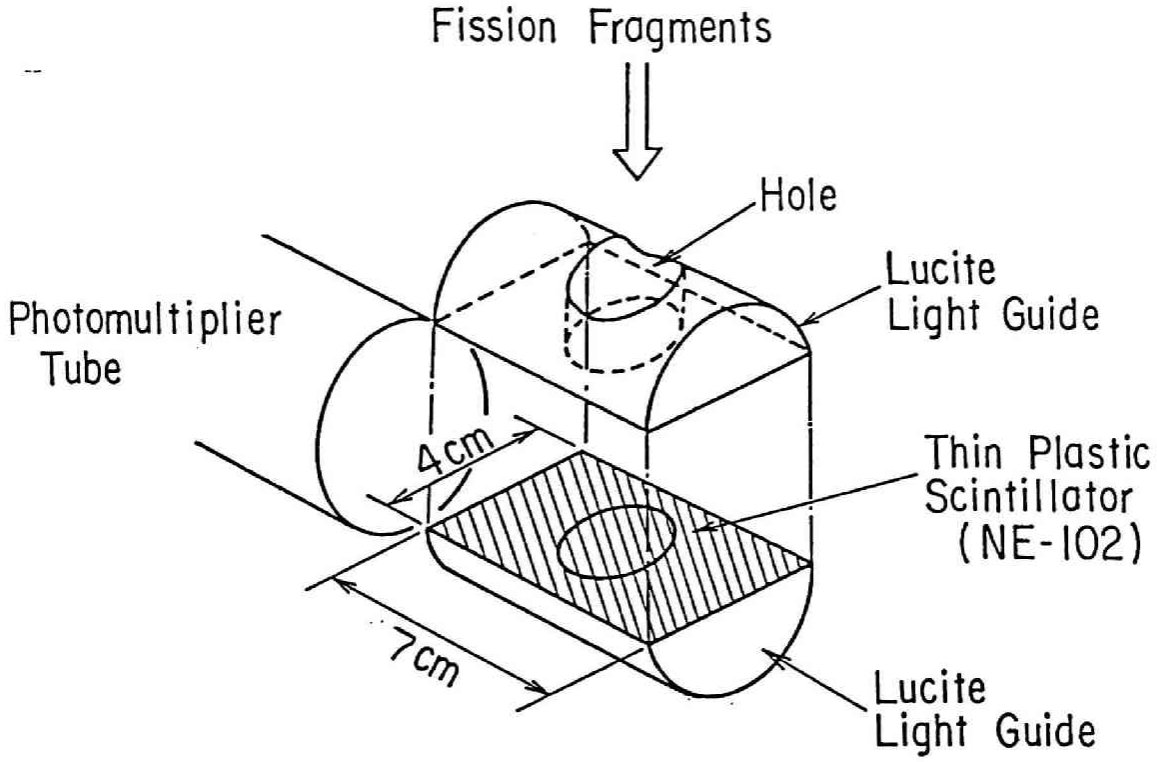

Fig 2.3 Thin film detector (TFD). The thin plastic scintillator film is shown by the shaded region. The film was made of NE102 and was sandwiched between two hemicylindrical light guide made of lucite. Fission fragments pass through holes bored at the center of the light guides.

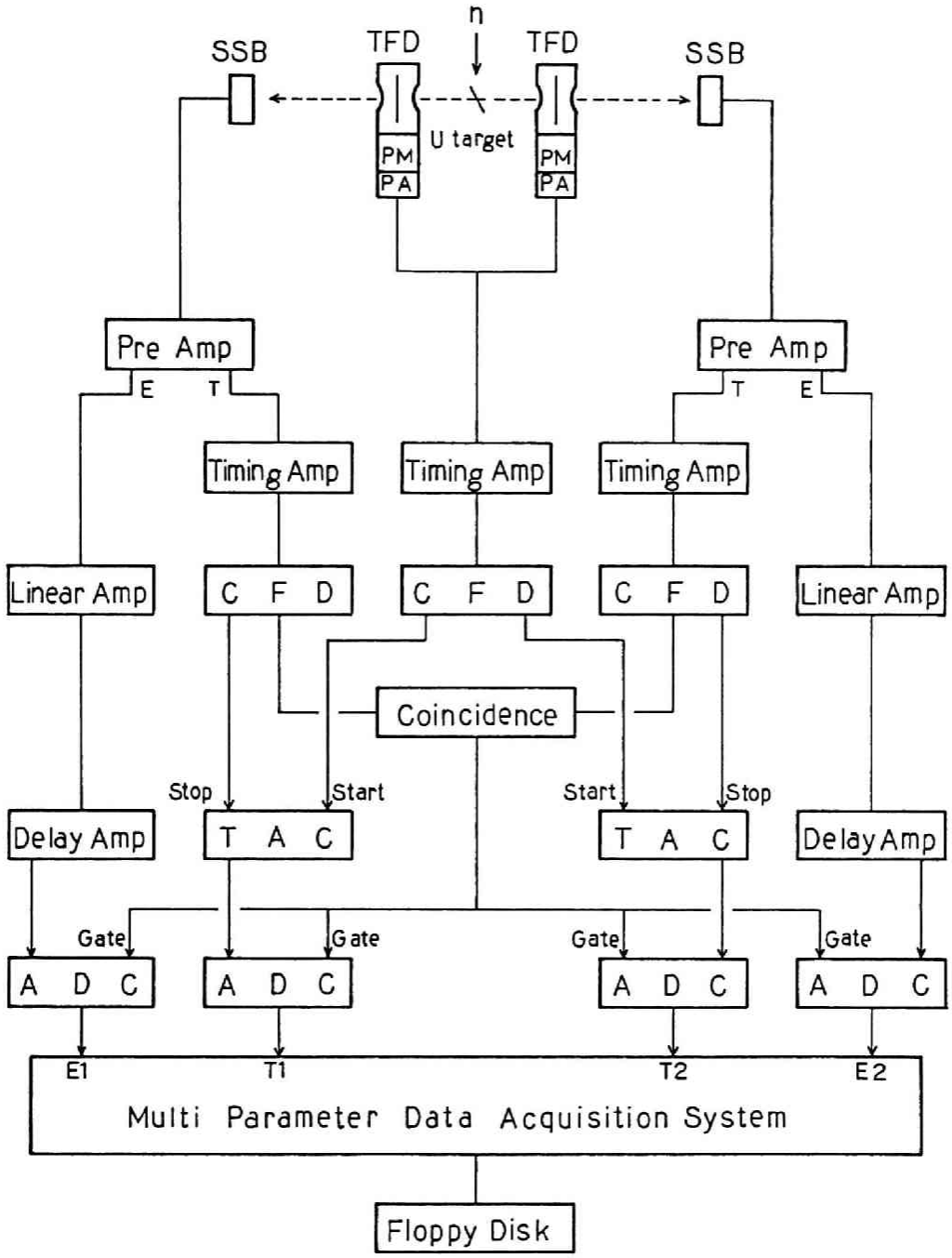

Fig.2.4 The electronic circuits for the double-energy double-velocity measurement. TFD: thin film detector; SSB: silicon surface barrier detector; PM: photomultiplier; PA and Pre Amp: preamplifier; Timing Amp: timing amplifier; CFD: constant fraction discriminator; Linear Amp: linear amplifier; Delay Amp: delay amplifier; Coincidence: coincidence circuit; TAC: time to amplitude converter; ADC: analog to digital converter.

3. Thin film detector as a start detector

3.1 Introduction

A thin film detector (TFD) has been developed by Muga, *et al.*[1]. An outline of a TFD is shown in Fig.3.1. The TFD makes use of a thin plastic scintillator film some tens to hundreds of $\mu g/cm^2$ thick, which is shown by the hatched area in Fig.3.1, and a pair of hemicylindrical light guides which have holes to let charged particles pass.

The TFD has some merits because of its small thickness; it is insensitive to gamma rays and neutrons and it suits in-beam experiments for heavy charged particles. Because of these features, the TFD has been used as a ΔE-type detector[2] and a timing detector[1] for these particles. The response of the TFD to heavy charged particles like ^{16}O, $^{35,37}Cl$, ^{40}Ar, $^{79,81}Br$ and ^{127}I was measured[3] and analyzed by the models of luminescence production developed by Muga, *et al.*[4] and Ajitanand[5]. However, the relationship between the TFD response to heavy charged particles and the thickness of the scintillator film has not been discussed previously. The pulse height spectrum of the TFD for fission fragments was measured by Batra, *et al.*[6] and Ajitanand *et al* [7] but its dependence on the scintillator film thickness and on the incident beam position in the scintillator film were scarcely discussed.

In order to understand the characteristics of the TFD, the author made a new model of luminescence production in a very thin plastic scintillator film. In Chapter 3.2, the model of luminescence production is described. Experimental measurements of the dependence of the luminescence production on the scintillator film thickness and on the incident beam position are presented in Chapter 3.3.

3.2 A new model of luminescence production in a very thin plastic scintillator film[8]

3.2.1. Introduction

The specific luminescence (dL/dx) in a plastic scintillator has been studied by many researchers such as Birks[9] and Smith, *et al.*[10),11)] on electrons, protons and alpha particles as a function of specific energy loss (dE/dx). However, the specific luminescence of heavy ions with low energy has not been studied much because of the difficulty in deriving dL/dx from the integrated scintillator response for the large dE/dx of heavy ions in a scintillator with typical dimensions. In order to measure the specific luminescence of heavy ions directly, very thin fluorescent material is needed through which heavy ions can pass. With the development of a thin plastic scintillator film[1], direct measurement of the specific luminescence became possible. Muga, *et al* measured the response of a plastic scintillator 100μg/cm^2 thick to ^{16}O, ^{35,37}Cl, ^{40}Ar, ^{79,81}Br and ^{127}I ions and defined these responses as the specific luminescence of the ions[3].

Muga, *et al.*[3),4)] and Ajitanand[5] reported on models of the luminescence production in a plastic scintillator film. However, the one proposed by Muga, *et al.* required cumbersome numerical integrals and parameters which had unobvious physical meanings to fit to experiments, and Ajitanand's model was a semiempirical formula in which five parameters were indispensable. Common to these two models, the thickness of the plastic scintillator film, which characterizes the thin plastic scintillator film, was not taken into account. Although these two models explain the experimental data of the luminescence production for the 100μg/cm^2 scintillator film, it is not valid to apply these models to the data of scintillator films with other thicknesses, especially to thinner scintillator films.

In order to improve the luminescence production model

and to make clear the relation between the luminescence production and the thickness of the plastic scintillator films, a model of luminescence production was made by the author. This model explicitly contains the thickness of the plastic scintillator film and needs only one parameter called the "effective range of the electron", which is determined experimentally.

In this chapter, the luminescence production model and its application are described. First, the luminescence production model which takes into account the thickness of the scintillator film is described in Chapter 3.2.2. Secondly, by applying this model, calculated values of the luminescence production for the ^{16}O, $^{35,37}Cl$, ^{40}Ar, $^{79,81}Br$ and ^{127}I ions are compared with the experimental data obtained by Muga, *et al.*[3]. The double-valuedness of the luminescence production on the stopping power of the ^{16}O ion, which was measured by Muga, *et al.*[12], is also analyzed in this model.

3.2.2 A new model of luminescence production in plastic scintillator film

The luminescence production can be considered in three steps: (1) free electrons in the scintillator film recoil by heavy ion impact (recoiling primary electrons); (2) recoiled electrons excite π-electrons (π-electron excitation); and (3) photons are emitted when the π-electrons deexcite (deexcitation of π-electron and photon emission).

For each step we can deal with the following procedures.

(1) Recoiling primary electrons

The heavy ion makes electrons in the plastic scintillator film recoil according to the Rutherford scattering cross section $d\sigma$,

$$d\sigma = \frac{1}{4}\left(\frac{e^2 Z_{eff}}{\mu V^2}\right)^2 \frac{d\theta}{\sin^4(\theta/2)} = \sigma f(\theta) d\theta,$$

$$\sigma = \frac{1}{4}\left(\frac{e^2 Z_{eff}}{\mu V^2}\right)^2. \qquad (3-1)$$

In Eq.(3-1), V and Z_{eff} are the velocity and the effective charge of the heavy ion, respectively, and μ is the reduced mass of the heavy ion with mass M and the electron mass m which nearly equals m. The effective charge Z_{eff} is given by[13],

$$Z_{eff} = Z\left[1-exp(-125\beta/Z^{2/3})\right]. \tag{3-2}$$

where β is the ratio of the velocity of the heavy ion to the light velocity. Eq (3-1) is rewritten using the relation

$$E = \frac{1}{2}kMV^2, \tag{3-3}$$

as

$$\sigma = \frac{1}{4}\left(\frac{kMe^2Z_{eff}}{2mE}\right)^2 \propto \left(\frac{MZ_{eff}}{E}\right)^2. \tag{3-4}$$

where E is the energy of the heavy ion in MeV and k is the conversion constant 1.0365 from MKS units to cm, amu, ns and MeV in energy.

The electron energy E_e recoiled with an angle θ is given as[14]

$$E_e = 2m\left(\frac{M}{M+m}V\cos\theta\right)^2 = \frac{4mE}{kM}\cos^2\theta. \tag{3-5}$$

The range of the primary electron R can be given by

$$R = gE_e = R_0\cos^2\theta, \tag{3-6}$$

$$R_0 = R_0(E,M) = g\frac{4mE}{kM} \tag{3-7}$$

In Eq.(3-7), g=9.62×10^{-3}cm/MeV[15] and R_0 is the primary electron range for the case of θ=0.

The primary electrons move from the recoil point x to the end of their range. The region in which primary electrons are able to move is shown in Fig.3.2(a). This region is called $P(R_0,x)$ in this chapter.

Second generation of scattered electrons is not considered here, because the number of secondary electrons is considered to be proportional to that of primary electrons.

(2) π-electron excitation

In order to calculate the number of π-electrons excited

by the primary electrons, we propose the following assumptions.

1) The π-electron density in the plastic scintillator is uniform and the primary electrons transfer a constant energy to π-electrons.

2) Most of the primary electrons transit towards the recoil direction statistically and the number of electrons scattered by the primary electrons is negligible.

3) The primary electrons cannot excite π-electrons at the beginning of their range because their energy is too high, but can excite them when their energy is low enough, i.e , when their range is less than the "effective range R_e" and greater than zero. The effective range is shown in Fig.3.2(b) and the region where π-electrons are excited is shown by the hatched area.

4) For the calculation of the volume of this hatched region, for simplicity, we calculate $P(R_0,x)-P(R_0-R_e,x)$ instead of the exact volume of the region where π-electrons are excited. A drawing of $P(R_0,x)-P(R_0-R_e,x)$ is shown in Fig.3.2(c). The largest difference between these two volumes in Fig.3.2(b) and (c) is less than 20%. This region is hereafter called the effective region, $P_{eff}(R_0,x)$.

5) The total number of the excited π-electrons can be calculated by integrating the product of $d\sigma$ and $P_{eff}(R_0,x)$. Here the angular part of $d\sigma$ is neglected as a first approximation With this assumption, only the volume of the effective region is required for the calculation.

For the calculation of the effective region $P_{eff}(R_0,x)$, we must first calculate $P(R_0,x)$. From Fig.3.2(a) the following relations are obtained.

$$h = R\cos\theta = R_0\cos^3\theta, \tag{3-8}$$

$$r^2 = R^2 - h^2 = R_0^{2/3}h^{4/3} - h^2. \tag{3-9}$$

$P(R_0,x)$ must be calculated taking into account the relationship of the primary electron range R_0, the thickness of the scintillator film T and the position of the heavy ion x in the film. In the case of

(a) $0 < x \leqq T - R_0$ (Fig.3.3(a)),

$$P_a(R_0, x) = \int_0^{R_0} \pi(R^2 - h^2)dh = \frac{2}{21}\pi R_0^3. \quad (3\text{-}10)$$

(b) $T - R_0 < x \leqq T$ (Fig.3.3(b)),

$$P_b(R_0, x) = \int_0^{T-x} \pi(R^2 - h^2)dh$$

$$= \frac{3}{7}R_0^{2/3}(T - x)^{7/3} - \frac{1}{3}\pi(T - x)^3. \quad (3\text{-}11)$$

For the calculation of the effective volume, we consider the following three cases; $R_0 \leqq T$, $R_0 - R_e \leqq T < R_0$ and $T < R_0 - R_e$.

In the case of $R_0 \leqq T$ and

1) $0 < x \leqq T - R_0$,

$$P_{eff,1}(R_0, x) = P_a(R_0, x) - P_a(R_0 - R_e, x)$$

$$= \frac{2}{21}\pi\{R_0^3 - (R_0 - R_e)^3\}, \quad (3\text{-}12)$$

2) $T - R_0 < x \leqq T - (R_0 - R_e)$,

$$P_{eff,2}(R_0, x) = P_b(R_0, x) - P_a(R_0 - R_e, x)$$

$$= \frac{3}{7}\pi R_0^{2/3}(T - x)^{7/3} - \frac{1}{3}\pi(T - x)^3$$

$$- \frac{2}{21}\pi(R_0 - R_e)^3, \quad (3\text{-}13)$$

3) $T - (R_0 - R_e) < x \leqq T$,

$$P_{eff,3}(R_0, x) = P_b(R_0, x) - P_b(R_0 - R_e, x)$$

$$= \frac{3}{7}\pi(T - x)^{7/3}\{R_0^{2/3} - (R_0 - R_e)^{2/3}\}. \quad (3\text{-}14)$$

In the case of $R_0 - R_e \leqq T < R_0$ and

4) $0 < x \leqq T - (R_0 - R_e)$,

$$P_{eff,4}(R_0, x) = P_b(R_0, x) - P_a(R_0 - R_e, x)$$

$$= \frac{3}{7}\pi R_0^{2/3}(T - x)^{7/3} - \frac{1}{3}\pi(T - x)^3$$

$$- \frac{2}{21}\pi(R_0 - R_e)^3, \quad (3\text{-}15)$$

5) $T - (R_0 - R_e) < x \leqq T$,

$$P_{eff,5}(R_0, x) = P_b(R_0, x) - P_b(R_0 - R_e, x)$$

$$= \frac{3}{7}\pi(T - x)^{7/3}\{R_0^{2/3} - (R_0 - R_e)^{2/3}\}. \quad (3\text{-}16)$$

6) In the case of $T < R_0 - R_e$,

$$P_{eff,6}(R_0, x) = P_b(R_0, x) - P_b(R_0 - R_e, x)$$
$$= \frac{3}{7}\pi(T - x)^{7/3}\{R_0^{2/3} - (R_0 - R_e)^{2/3}\}. \quad (3-17)$$

(3) Deexcitation of π-electrons and photon emission

The total number of emitted photons, i.e., the luminescence L, is proportional to the integral of the product of the density of the π-electrons in the scintillator film ρ, the recoiling cross section of an electron σ and the effective volume $P_{eff}(R_0, x)$ along the heavy ion path x,

$$L = \int_0^T \rho\sigma P_{eff}(R_0, x)dx, \quad (3-18)$$

where R_0 is also a function of the integrand, since the heavy ion energy decreases as it traverses the plastic scintillator film. Instead of integration, we divided the thickness of the scintillator film into 100 regions, and summed up the luminescence productions in each region. The energy loss of the heavy ion was calculated by Bethe's formula in each region.

3.2.3 Application

Using the model described above, the luminescence production for ^{16}O, $^{35,37}Cl$, ^{40}Ar, $^{79,81}Br$ and ^{127}I ions were calculated. The calculated results are compared with the experimental data of a scintillator film of 100μg/cm^2 thickness as measured by Muga, *et al.*[4] and is shown in Fig 3.4. The effective range R_e was determined to be 12.5μg/cm^2 by fitting to the data. The calculated result was normalized to the experimental data for the ^{16}O ion at an energy of 28.8MeV. The experimental and calculated data agree well within the error bars. However, of these five nuclides, $^{35,37}Cl$ and ^{40}Ar do not show a very good fit. These rather poor agreements might be attributed to the thickness of the plastic scintillator film. In the experiment of Muga, *et al.*, the uncertainty of the film

thickness was about 25%[16]. Calculations have been done with a thickness of 100$\mu g/cm^2$ for all the nuclides, and if the film thickness is set to 120$\mu g/cm^2$ in the calculation of $^{35,37}Cl$ and ^{40}Ar, the agreement becomes much better.

The double-valuedness of the luminescence production on the stopping power for the ^{16}O ion, which Muga, *et al.* originally presented[12] was investigated using this new model of luminescence production, and the calculated result agrees satisfactorily with the measured values, as shown in Fig.3.5. The double-valuedness can be understood by using the drawing of the effective region as shown in Fig.3.6. With high energy, R_0 given by Eq.(3-7) is long enough to transmit primary electrons to outside the scintillator film, and only a small part of effective region is effective for the luminescence production.

Birks has derived a relation of the specific luminescence dL/dx and the specific energy loss dE/dx, given by[9]

$$\frac{dL}{dx} = S\cdot\frac{dE/dx}{1+kB(dE/dx)}, \qquad (3-19)$$

where S and kB are the parameters that fit this formula to the experimental data. This relation has been obtained by studying the specific luminescence of light particles such as electrons, protons and alpha particles and shows that the specific luminescence is approximately proportional to the specific energy loss. From the experiment of Muga, *et al.* and the calculation the author carried out, this proportionality is not shown (see Fig.3 5). So, we can conclude that Birks' relationship is not applicable for heavy ions with low energy.

3.3 Response characteristics of thin film detectors to fission fragments[17]

3.3.1 Introduction

In Chapter 3.2, a new model of luminescence production, which includes the thickness of the scintillator film, was proposed. This model satisfactorily explained the response of the TFD with the scintillator film thickness of 100$\mu g/cm^2$ to heavy charged particles as described above. It is the purpose of this chapter to study the dependence of the TFD response on the thickness of the scintillator film and on the incident beam position in the film quantitatively, making use of this new model of luminescence production.

The author measured the pulse height spectra of the spontaneous fission fragment of ^{252}Cf using four TFDs with different thicknesses of the scintillator films at five positions in each film. In Chapter 3.3.2, the details of the experiment are described The result and its quantitative analysis are described in Chapter 3.3.3. In Chapter 3.3.4, the theoretical treatment of the experimental spectra by using the model of luminescence production and the dependence of the TFD pulse height spectrum on the thickness of the scintillator film and on the incident beam position are discussed.

3.3.2 Experimental details

The outline of the TFD used in this experiment is shown in Fig.3.1. Two hemicylindrical light guides with holes of 20mm diameter sandwich a scintillator film. The scintillator film was made of NE102 following the method developed by Muga, *et al.*[18]. The film thicknesses used were about 50, 100, 200 and 300$\mu g/cm^2$. The thickness of these films was determined by the energy loss of alpha particles from the ^{252}Cf source at five positions along the diameter of the films, as shown in Fig.3.7, and the deviation of the thicknesses from

the mean value were within 25%.

The experimental arrangement and the electric circuit are shown in Fig.3.8. The fission fragments from a ^{252}Cf source (1μCi) were collimated to 3mm in diameter. The fission fragments passed through the scintillator film and finally impinged upon a silicon surface barrier detector (SSB). The light produced in the scintillator was transmitted to a Hamamatsu R580 photomultiplier by the light guide. The TFD output signal was gated by the signal from the SSB to eliminate background noise. The pulse height spectrum from the TFD was measured by this method at five positions as shown in Fig 3 7.

3.3.3 Experimental results and quantitative analysis

The experimental results are shown in Fig.3.9. With the films of 200 and 300$\mu g/cm^2$ thickness, each spectrum has two peaks. The peak in the higher channel corresponds to the light fission fragment of ^{252}Cf. The two peaks clearly separated for the 300$\mu g/cm^2$ thick film, while they become closer to each other as the thickness of the film decreased and are finally superimposed for the case of the 50$\mu g/cm^2$ thick film. As the incident beam position moves further from the photomultiplier, the two peaks become closer for all film thickness.

To investigate the experimental results quantitatively, we decomposed each of these TFD pulse height spectra into two Gaussians, as shown in Fig.3.10, and then characterized these decomposed spectra by the peak channels of heavy and light fragment groups, H_p and L_p, respectively, and their ratio H_p/L_p; the peak heights, H_h and L_h, and their ratio H_h/L_h; and the ratio of the areas of the two Gaussians, H_a/L_a. The results of the analysis of these values are shown in Table 3.1

H_p and L_p become smaller as the incident beam position becomes further from the photomultiplier: the longer the paths of the photons to reach the photomultiplier, the more the

attenuation of the photons. This position dependence is discussed in Chapter 3.3.4 (3).

If we compare the area ratio H_a/L_a at position 1 for each film thickness in Table 3.1, this ratio decreases as the film becomes thinner. This means that the heavy fragment group fails to be counted when the scintillator film is thin: the heavy fragment group cannot produce enough photons to be detected by the photomultiplier in a thin scintillator film. With this miscounting and the attenuation of photons described above, the position dependence of the area ratio is explained. In the cases of the 200 and 300$\mu g/cm^2$ thick films, both the heavy and the light fragment groups produce enough photons to be detected by the photomultiplier even though the photons attenuate, and the area ratio shows little position dependence. With the 100$\mu g/cm^2$ thick film, the area ratio shows an interesting change according to the incident beam position. As the beam position becomes further from the photomultiplier, the photons produced by the heavy fragments fail to be counted by the photomultiplier because of the attenuation of the photons in the scintillator film, and the area ratio changes and becomes smaller. In the case of the 50$\mu g/cm^2$ thick film, even the photons produced by the light fragments fail to be counted by the photomultiplier, and the area ratio shows little dependence on the incident beam position.

The peak height ratio H_h/L_h becomes smaller as the film becomes thinner. This shows that the heavy fragments are unable to produce enough photons to be counted as an event with a thinner scintillator film.

3.3.4 Theoretical analysis of pulse height spectrum

In order to analyze the pulse height spectrum of the TFD for the ^{252}Cf spontaneous fission fragments theoretically, we took the following steps: (1) calculation of the yield of photons produced by fission fragments in the scintillator film, (2) derivation of the TFD pulse height spectrum at

incident beam position 1 as a standard spectrum in each film, and (3) calculation of the TFD pulse height spectra at other beam positions using the standard spectrum. The details of each step are described below.

(1) Yield of photons

The yield of photons produced by the fission fragments from ^{252}Cf spontaneous fission can be obtained as a superposition of the number of photons produced by heavy ions with mass M, proton number Z and kinetic energy E.

We assume that the fission fragment with mass M has a yield distribution which is a function of the number of protons and kinetic energy as follows:

$$Y(M,Z,E) = c \cdot Y(M) \cdot \exp\left(-\frac{(Z-Z_p)^2}{1.5}\right) \cdot \exp\left(-\frac{(E-E_p)^2}{128}\right), \qquad (3\text{-}20)$$

where Z_p and E_p are the most probable proton number and kinetic energy, respectively, $Y(M)$ is the yield of fission fragments with mass M and c is a normalization factor to make the total yield unity The most probable proton number is assumed to be the same ratio of the proton number to the mass number as in the fissioning nucleus ^{252}Cf. We assume that the experimental kinetic energy taken from the work of Schmitt, *et al.*[19] is the most probable kinetic energy. Half of the values of 1.5 and 128 are the standard deviation of the proton number[20] and kinetic energy[19] distributions, respectively.

We calculated the number of protons for all possible combinations of M, Z and E with the model of luminescence production in a thin scintillator film and derived the yield of photons from the fission fragments. The calculated result is shown in Fig.3.11.

(2) TFD pulse height spectrum at beam position 1

In order to calculate the TFD pulse height spectrum at beam position 1 from the yield of photons derived above, we first transform the abscissa of the yield of photons into that

of the experimental pulse height spectrum: the abscissa of the yield of photons is transformed so that the peak channels of the heavy and light fragments correspond between calculated and experimental spectra.

– The photons produced by the luminescence pass through the scintillator film to the light guide and the photomultiplier During their transmission, a large number of photons are lost through escape from the inside to the outside of the film and by absorption in the film. Therefore, we consider the broadening of the spectrum next. We distributed the yields of photons according to the abscissa of the experiment, so that the full width at half maximum (FWHM) of the peaks of the heavy and light fragment groups fit to the experiment. The resulting FWHM at the channel numbers of the heavy and light fragment peaks were 30% and 16%, respectively. The calculated results are shown in Fig.3.12. (3) TFD pulse height spectra at other beam positions

The relative numbers of photons produced by the fission fragments at incident beam positions 2, 3, 4 and 5 are listed in Table 3.2 as the ratio to those of position 1 in each film thickness. We call this ratio the photon attenuation factor. The TFD pulse height spectra have been obtained in the same manner as described above, by multiplying the photon attenuation factors in Table 3 2 with the spectra at position 1 for each film thickness. Examples of calculated results compared with experimental data are shown in Figs.3 13 and 3 14

The photon attenuation factor can be separated into two factors: the attenuation of photons in the scintillator film and the geometry of the light guide, which depends on the distance from the photomultiplier surface. The attenuation of photons in the scintillator film is explained as follows: the photons encounter the surface of the scintillator film many times before they reach the light guide. During these encounters, some photons escape from the inside to the outside of the scintillator film. Here we assume that the attenuation of the photon in the film is expressed as $\exp(-\sigma l)$, where l

is the photon path length and σ is the attenuation constant, determined experimentally.

Next, we consider the geometry of the light guide. The photons are detected more effectively when they reach the light guide at the edge closest to the photomultiplier rather than at the furthest edge. We assign a geometrical factor of 1 at the edge of the light guide nearest to the photomultiplier and a factor q ($q<1$) for the furthest edge (2cm further from the closest edge), where q is determined by fitting to the experimental data. The geometrical factor f at the edge at distance d from the nearest edge is assumed to be given by linear interpolation;

$$f=0.5(q-1)d+1. \qquad (3-21)$$

One photon which reaches the edge of the light guide with f after transmitting a path l in the film is detected as $f\exp(-\sigma l)$ by the photomultiplier.

By fitting the experimental data given in Table 3.2, the photon attenuation constant and the geometrical factor can be obtained, respectively, as $1.6\mathrm{cm}^{-1}$ and 0.6 on the average

3.3.5 Summary

The dependence of the TFD pulse height spectrum on the thickness of the scintillator film and on the incident beam position in the film were obtained experimentally. The experimental results were analyzed theoretically by using the luminescence production model described in Chapter 3.2, and were in good agreement with the model. It is concluded that this model is applicable to the analysis of the pulse height spectrum of the TFD with films of various thicknesses. The calculated spectra of beam positions of 3 and 5 shown in Figs.3.13 and 3.14 do not show a very good fit to the experimental spectra. There might be something wrong in the method of transforming the abscissa of the calculated yield of photons into those of experimental pulse height spectra when photon

attenuation must be considered. Further study on the dependence of the pulse height spectrum of the TFD on the diameter of the hole of the light guide should be carried out.

3.4 Conclusion

(1) A new model of luminescence production in a very thin plastic scintillator film which contains the thickness of the film is proposed. This model has a clear physical meaning compared with the models reported by other authors and needs only one parameter. The calculated results of the luminescence production for the ^{16}O, $^{35,37}Cl$, ^{40}Ar, $^{79,81}Br$ and ^{127}I ions agreed well with experimental ones.

(2) The model of luminescence production explained the double-valuedness of the luminescence production of the ^{16}O ion on the basis of stopping power, which could not be understood using the formula of Birks. For large thicknesses, a new formula of specific luminescence production will be considered as a function of specific energy loss

(3) The dependence of the pulse height spectrum of ^{252}Cf spontaneous fission fragment on the thickness of the scintillator film and on the position in the scintillator film was studied experimentally and theoretically. This study calculated the pulse height spectrum of the TFD for a scintillator film of any thickness.

(4) A method for calculating the pulse height spectrum of the fission fragments which are composed of various particles with different masses, proton numbers and kinetic energies is developed.

References

1) Muga, M. L., Burnsed, D. J., Steeger, W. E. and Taylor, H. E.: Nucl. Instr. and Meth., 83, 135 (1970).
2) Muga, M. L.: Nucl. Instr. and Meth., **95**, 349 (1971).
3) Muga, L. and Griffith, G : Phys. Rev., **B9**, 3639 (1974).
4) Muga, L. and Diksc, M.: Nucl. Instr. and Meth., **122**, 553 (1974).
5) Ajitanand, N. N.: Nucl. Instr. and Meth., **143**, 345 (1977).
6) Batra,R.K. and Shotter,A.L.: Nucl. Instr. and Meth., **124**, 101 (1975).
7) Ajitanand, N. N. and Iyengar, K. N.: Nucl. Instr. and Meth., **133**, 71 (1976).
8) Kanno, I. and Nakagome, Y : Nucl. Instr. and Meth., **A244**, 551 (1986)
9) Birks, J. B.: "The Theory and Practice of Scintillation Counting", Macmillan, New York (1964).
10) Smith, D. L., Polk, R. G. and Miller, T. G.: Nucl. Instr. and Meth., **64**, 157 (1968)
11) Craun, R. L. and Smith, D. L.: Nucl. Instr. and Meth., **80**, 239 (1970).
12) Muga, L and Griffith, G.: Phys. Rev., B8, 4069 (1973).
13) Barkas, W. H.: "Nuclear Research Emulsions", Academic Press, New York, Vol.I, p.371 (1963)
14) Weber, K. H.: Nucl. Instr. and Meth., **25**, 261 (1964).
15) Kobetich, E. J and Katz, R.: Phys. Rev., **170**, 391 (1968).
16) Muga, M. L.: private communication (1984)
17) Kanno, I. and Nakagome, Y.: Nucl. Instr. and Meth., **A251**, 108 (1986).
18) Muga, M. L., Burnsed, D. J. and Steeger, W E.: Nucl. Instr. and Meth., **104**, 605 (1972).
19) Schmitt, H. W., Kiker, R. W. and Williams, C. W.: Phys. Rev., **137**, B837 (1964)
20) Hyde, E. K.: "The Nuclear Properties of the Heavy Elements, Vol.3: Fission Phenomena", Prentice-Hall, Englewood Cliffs, New Jersey, p.144 (1964).

Table 3.1 Characteristics of the pulse height spectra of TFD for the fission fragments of the ^{252}Cf spontaneous fission. H_p and L_p are the channel numbers for the heavy and light fragment peaks, respectively, and H_p/L_p is their ratio. H_h/L_h and H_a/L_a are the ratio of the peak height and of the yield for the heavy and light fragment peaks.

Thickness		Position 1	2	3	4	5
	H_p	23.8	18.4	21.5	18.6	17.7
	L_p	38.0	33.5	33.6	29.2	27.3
50μg/cm²	H_p/L_p	0.63	0.55	0.64	0.64	0.65
	H_h/L_h	0.47	0.56	0.35	0.47	0.34
	H_a/L_a	0.35	0.22	0.38	0.34	0.28
	H_p	59.0	-	43.5	36.5	41.8
	L_p	127.0	-	71.1	74.6	59.0
100μg/cm²	H_p/L_p	0.47	-	0.61	0.49	0.71
	H_h/L_h	1.32	-	1.02	1.12	0.63
	H_a/L_a	0.70	-	0.68	0.51	0.32
	H_p	75.5	-	65.4	-	54.3
	L_p	188.8	-	166.0	-	137.8
200μg/cm²	H_p/L_p	0.40	-	0.39	-	0.39
	H_h/L_h	1.35	-	1.13	-	1.14
	H_a/L_a	0.90	-	0.91	-	0.91
	H_p	114.1	105.4	90.7	76.8	67.6
	L_p	303.5	266.1	238.8	214.6	191.4
300μg/cm²	H_p/L_p	0.38	0.40	0.38	0.36	0.35
	H_h/L_h	1.39	1.35	1.32	1.41	1.49
	H_a/L_a	0.97	0.96	0.97	0.95	0.96

Table 3.2 Dependence of TFD pulse height on beam position. The pulse heights are normalized to position 1 for each film thickness

Thickness	Position				
	1	2	3	4	5
50μg/cm^2	1	0.80	0.84	0.65	0.60
100μg/cm^2	1	-	0.58	-	0.45
200μg/cm^2	1	-	0.88	-	0.74
300μg/cm^2	1	0.90	0.81	0.72	0.64

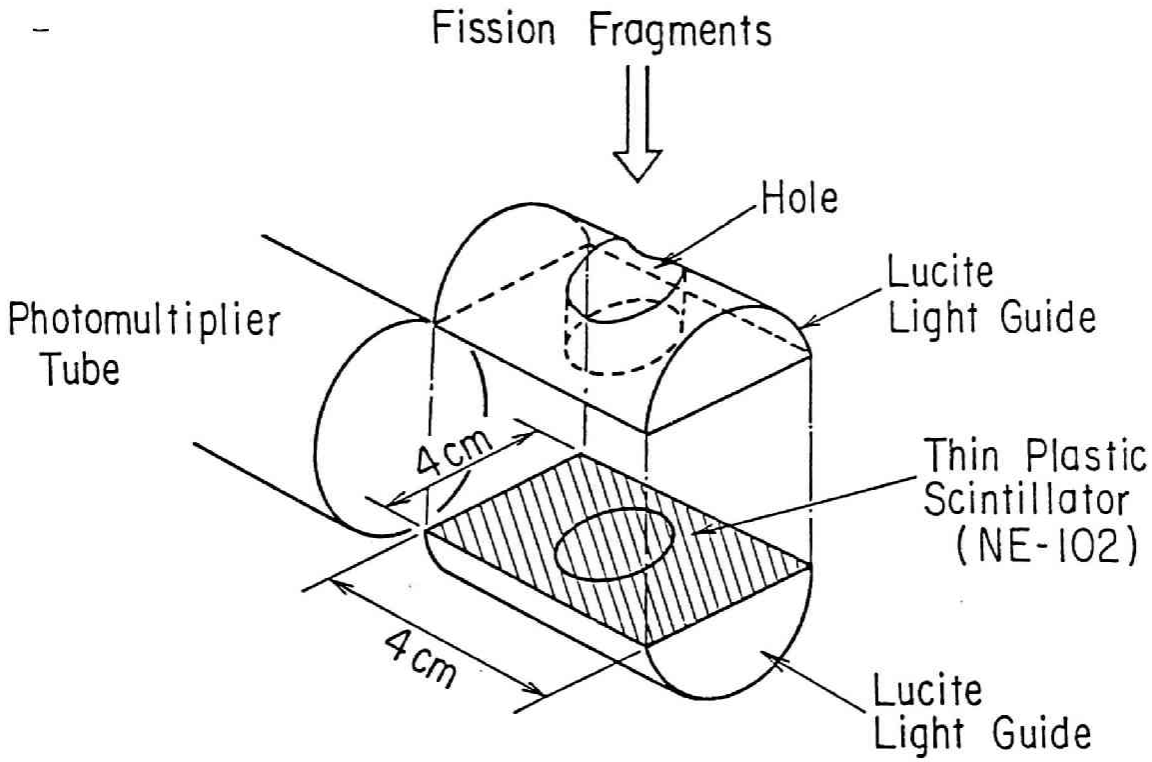

Fig.3.1 Illustration of a thin film detector (TFD) The thin plastic scintillator film is shown by the shaded region. The film was made of NE102 and was sandwiched between two hemi-cylindrical light guides made of lucite Charged particles pass through a hole bored at the center of the light guides

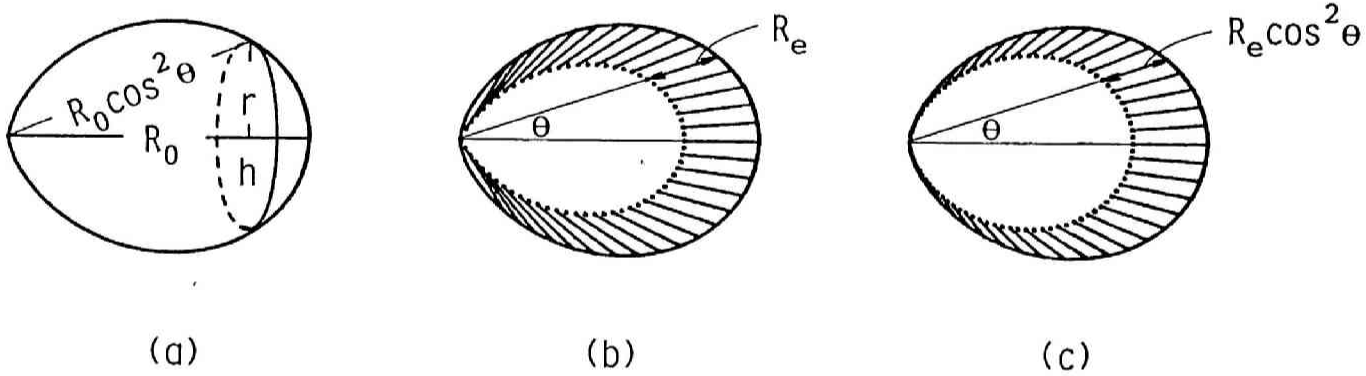

Fig.3.2 (a) The region in which primary electrons are able to move, $P(R_0,x)$. (b) π-electrons are excited within the hatched region. the primary electrons have ranges less than R_e in this region. (c) The substitution for the region described in (b), $P(R_0,x)-P(R_0-R_e,x)$, for simplicity of calculation. We call this region the effective region, $P_{eff}(R_0,x)$.

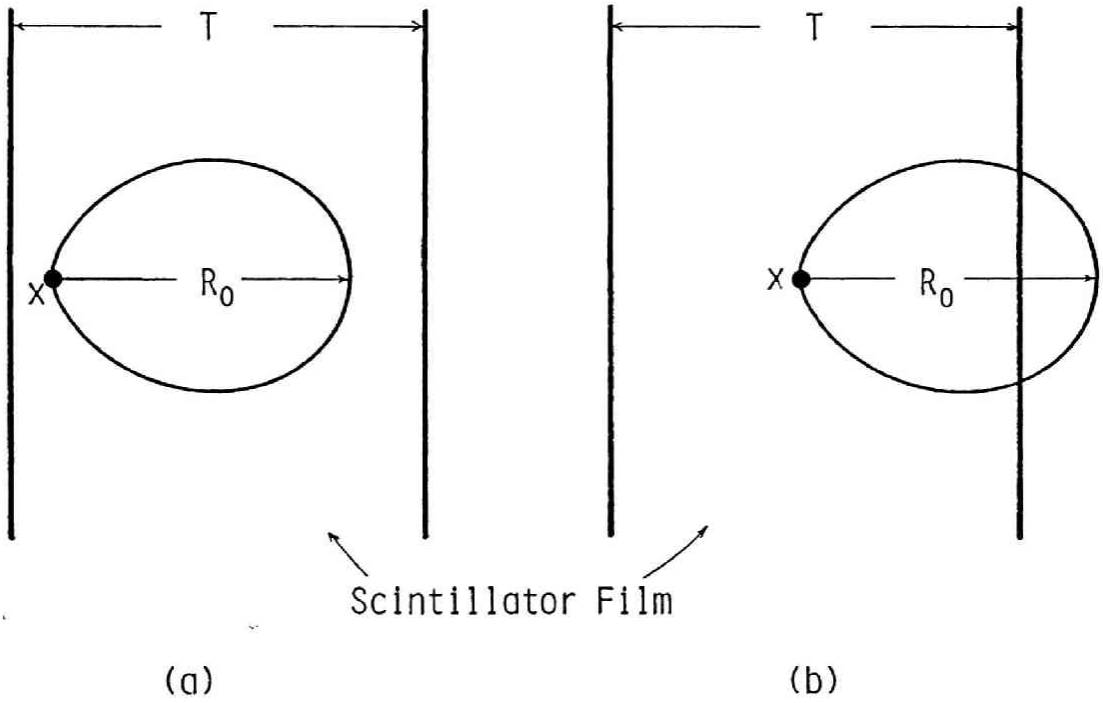

Fig.3.3 The thickness of the thin plastic scintillator film T and $P(R_0,x)$: (a) R_0 is less than T and $P(R_0,x)$ is contained inside the film. (b) R_0 is greater than T and part of $P(R_0,x)$ is outside of the film.

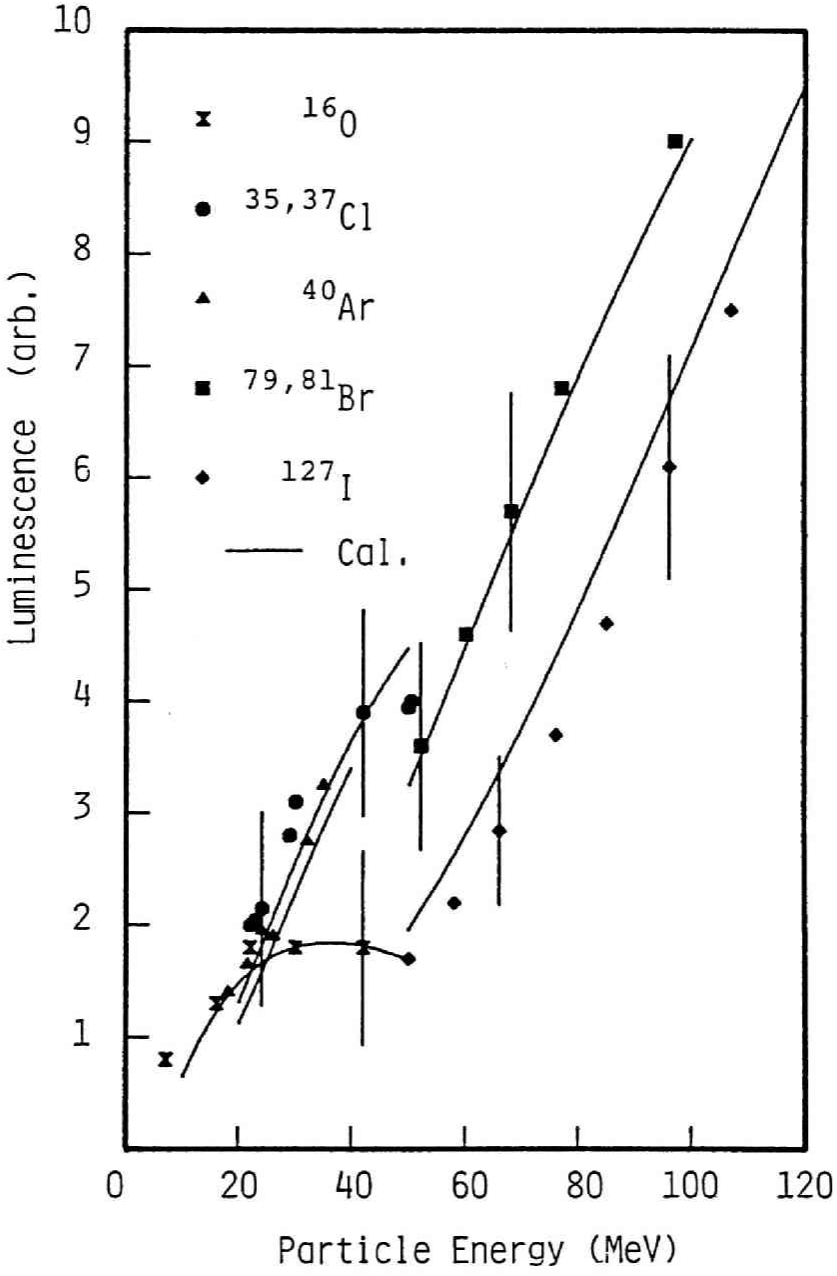

Fig.3.4 Calculated result of relative luminescence vs energy for heavy ions. Experimental data are taken from Ref.(5). The calculated results are normalized to the experimental data of ^{16}O at 28.8MeV energy.

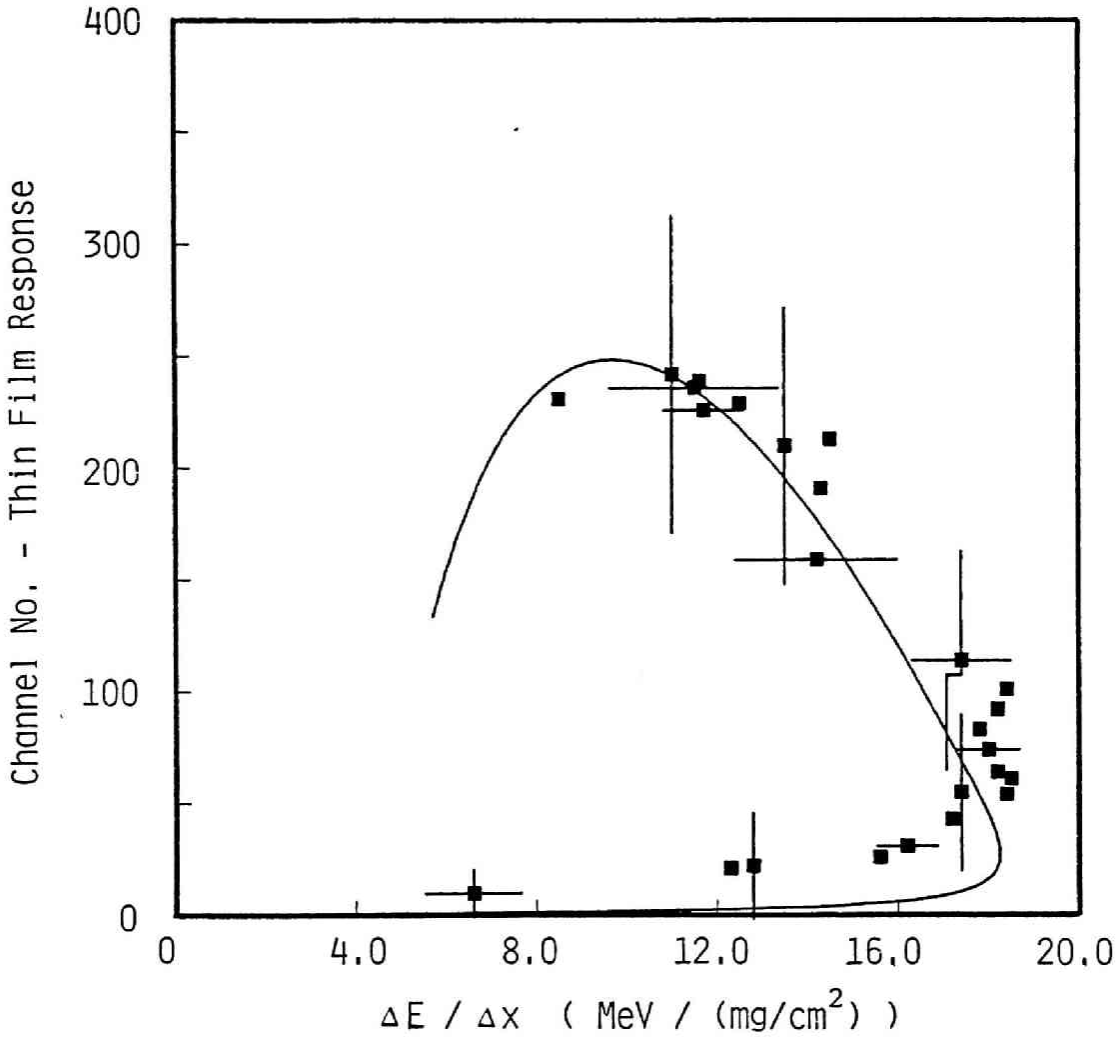

Fig.3.5 Luminescence production vs. energy loss for the ^{16}O ion. The experimental data have been taken from Ref.(13). The solid line is a calculated result from the model described in chapter 3.2.2.

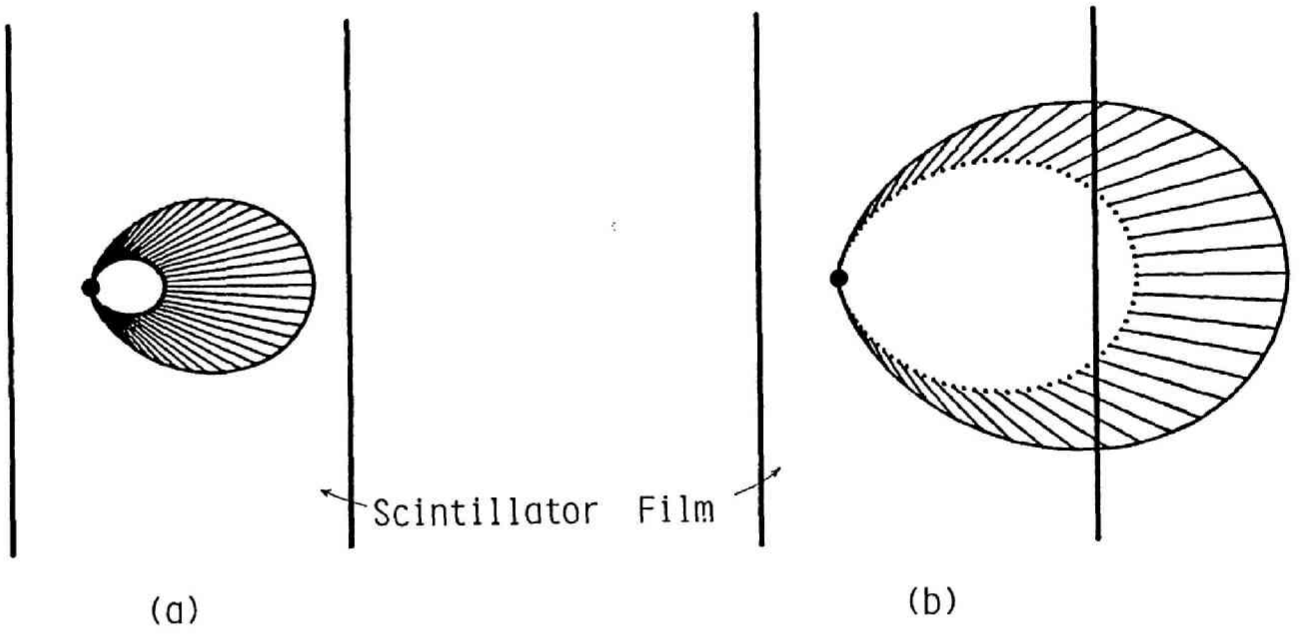

Fig.3.6 The relation between the scintillator film thickness and the ranges of primary electron for (a) low energy and (b) high energy.

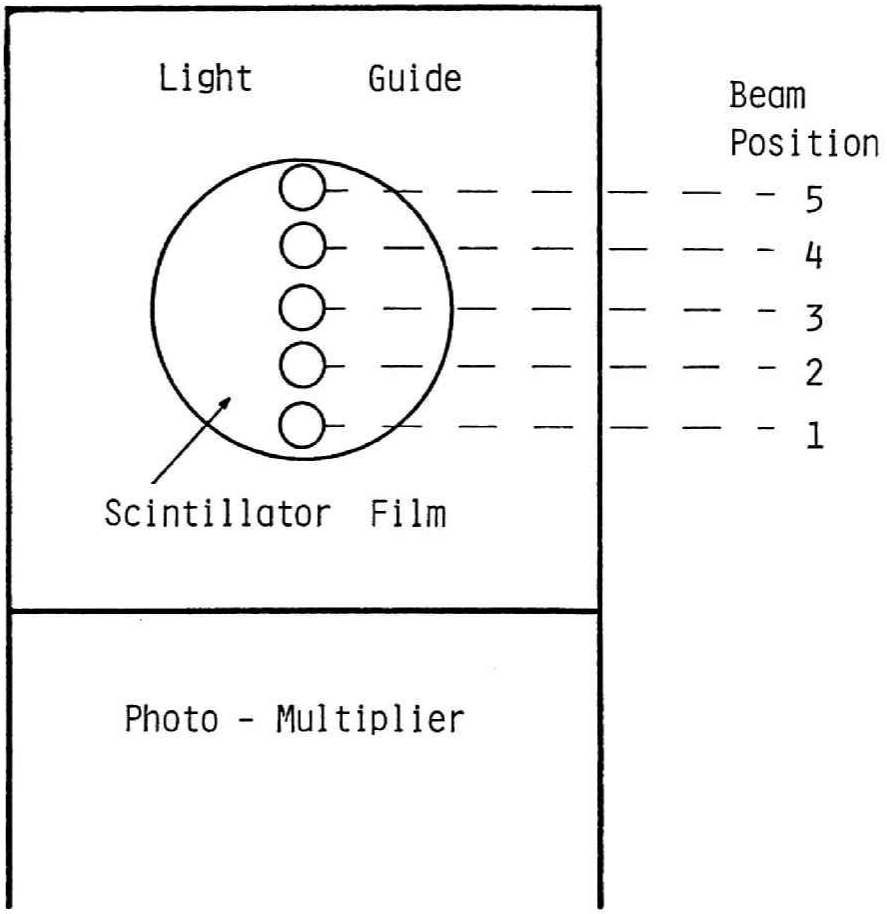

Fig.3.7 Incident beam position in the thin plastic scintillator film. The fission fragment beam is collimated to a diameter of 3mm. The distance between the neighboring beams is 4mm.

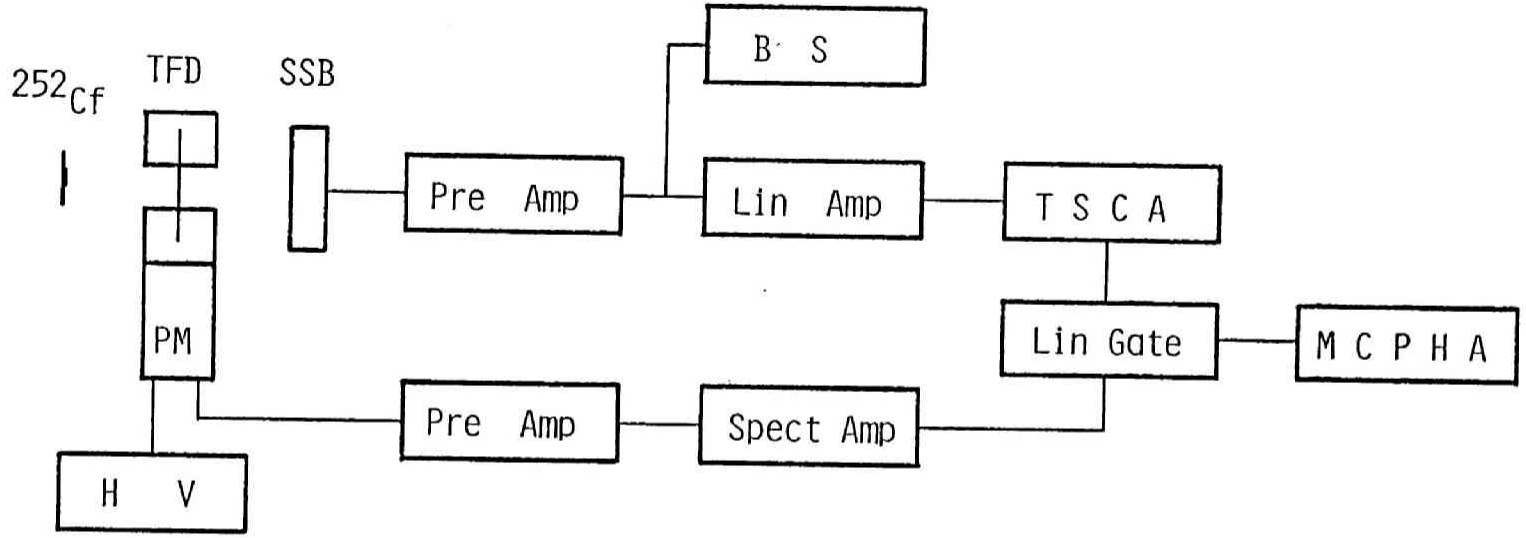

Fig.3.8 Experimental arrangement and electric circuits for the measurement of the TFD pulse height spectrum for ^{252}Cf spontaneous fission fragments, TFD: thin film detector; SSB: silicon surface barrier detector; PM: photomultiplier; Pre Amp: preamplifier; Lin Amp: linear amplifier; TSCA: timing single channel analyzer; Lin Gate: linear gate; Spect Amp: spectroscopy amplifier; MCPHA: multichannel pulse height analyzer; HV: high voltage supply for PM; BS: bias supply for SSB.

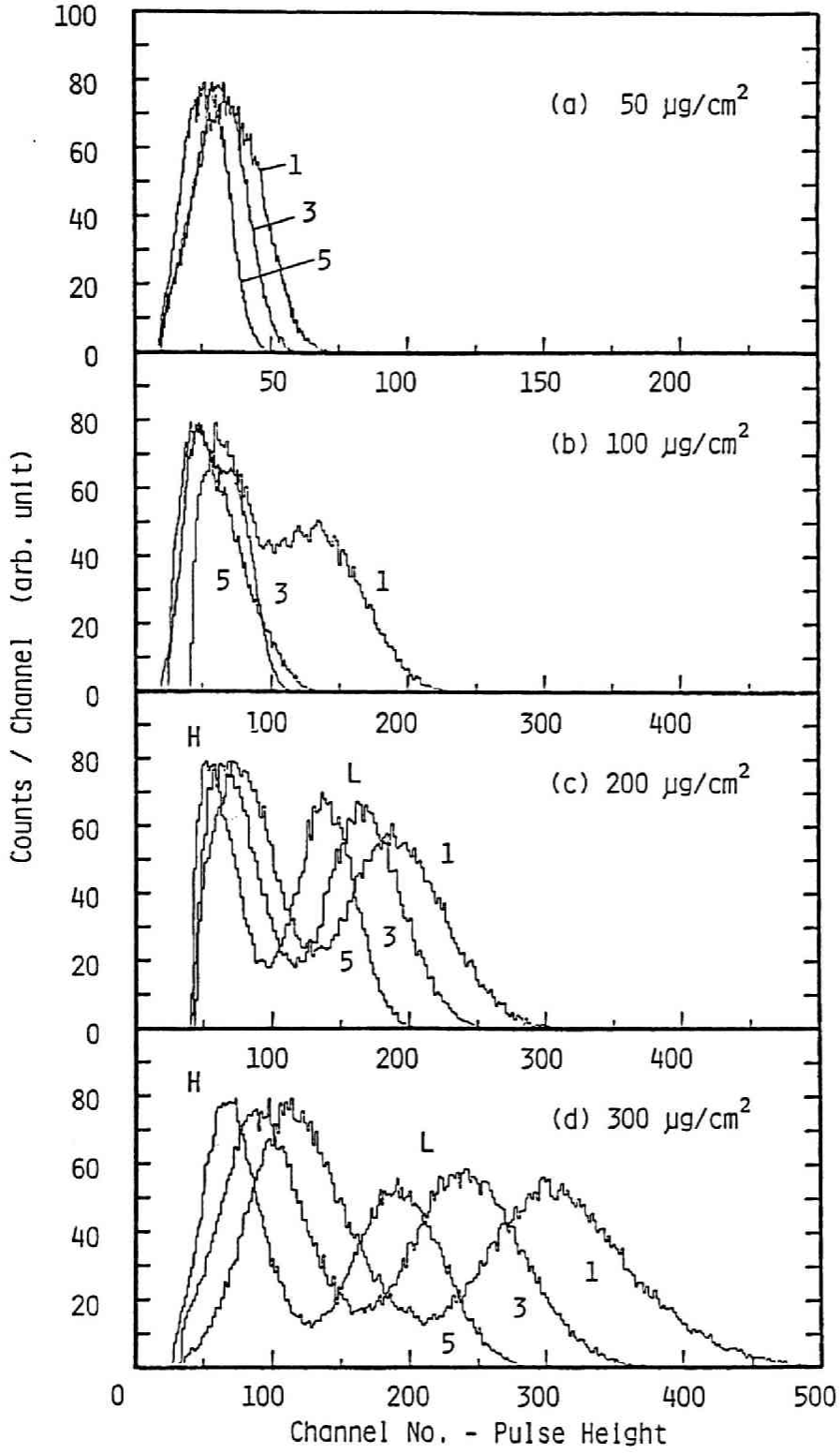

Fig.3.9 TFD pulse height spectra of ^{252}Cf spontaneous fission fragments. The scintillator films were (a) 50μg/cm², (b) 100μg/cm², (c) 200μg/cm² and (d) 300μg/cm² in thickness. The numbers 1, 3 and 5 in the figures indicate the incident beam positions (see Fig.3.7). H and L represent the heavy and light fragment peaks, respectively.

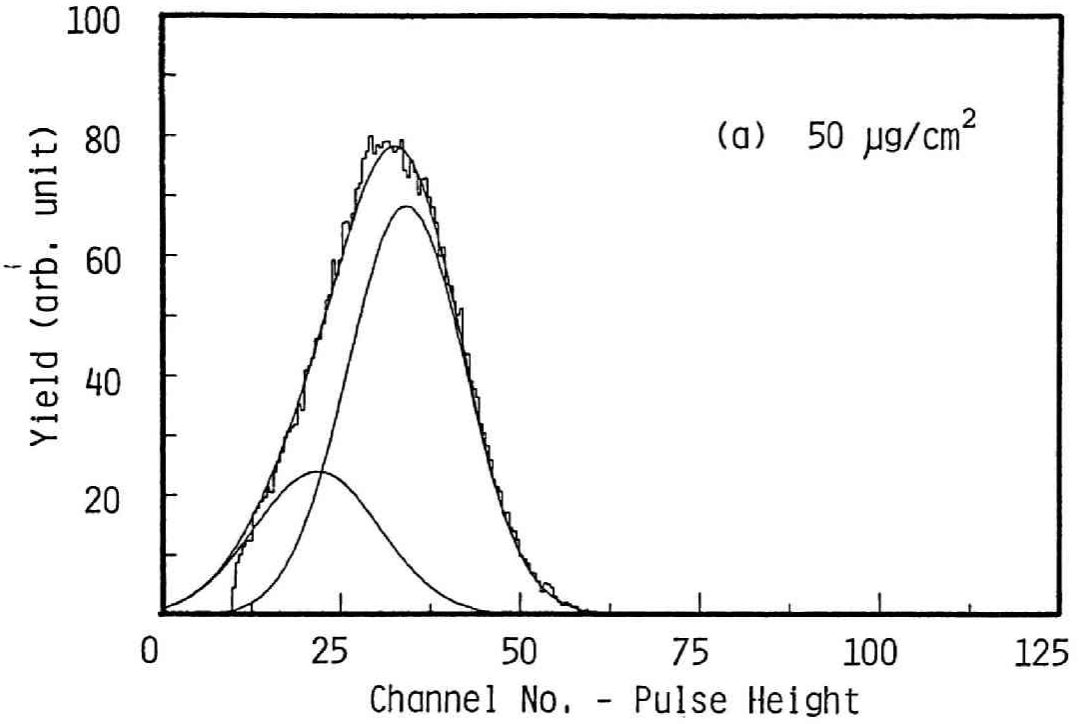

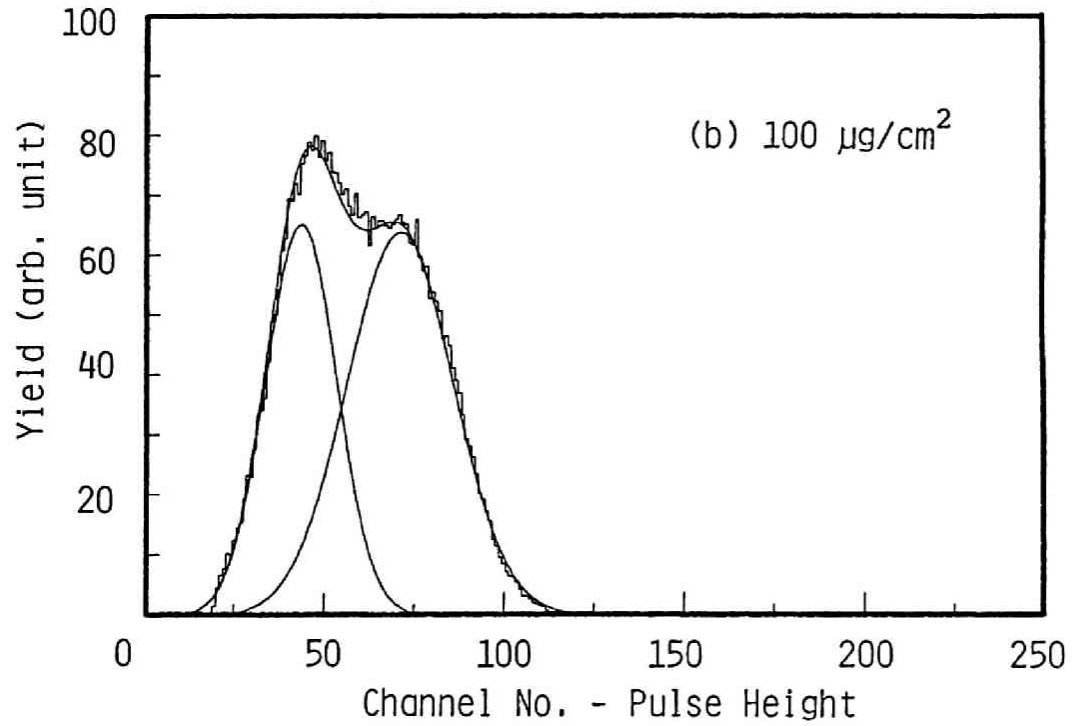

Fig.3.10 Examples of TFD pulse height spectra at beam position 3 decomposed into two Gaussians with the following scintillator thicknesses, (a) 50$\mu g/cm^2$, (b) 100$\mu g/cm^2$. The histogram represents the experimental data, and solid lines the fitted Gaussian distribution.

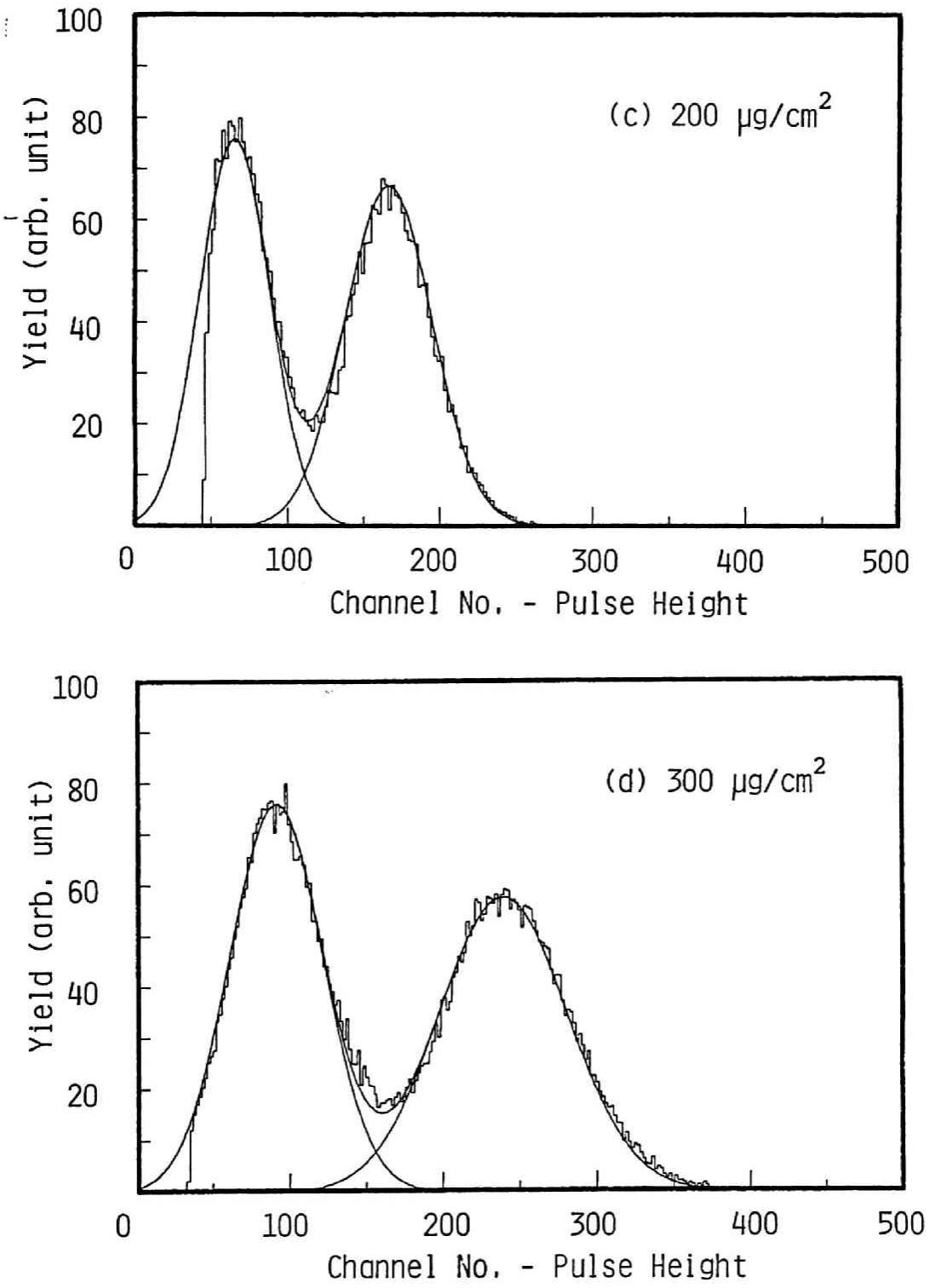

Fig.3.10 (continued) (c) 200μg/cm^2 and (d) 300μg/cm^2.

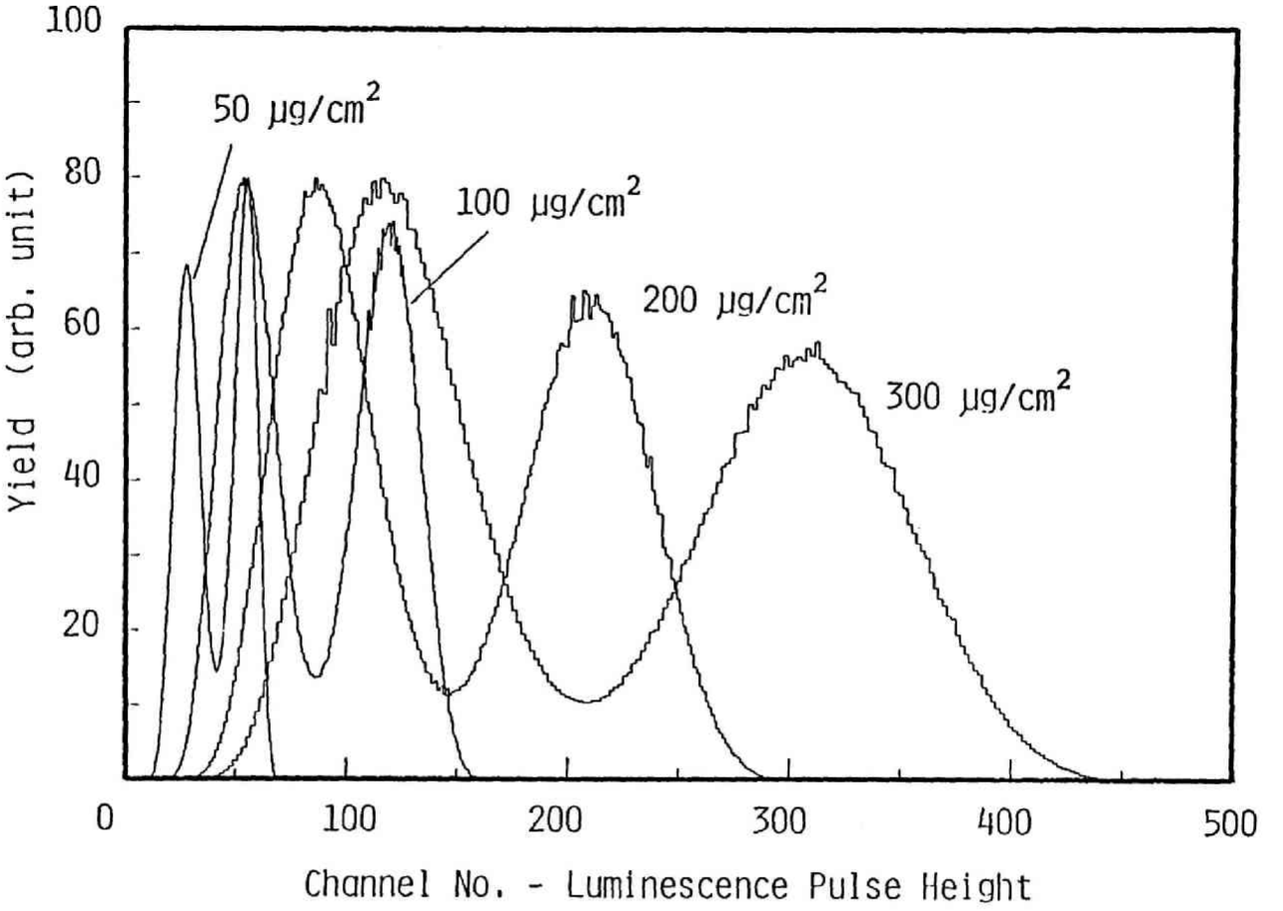

Fig.3.11 The calculated pulse height spectra of luminescence production from the ^{252}Cf spontaneous fission fragment. The thicknesses of the scintillator films are indicated in the figure. The peaks in the higher channel numbers correspond to the light fragments.

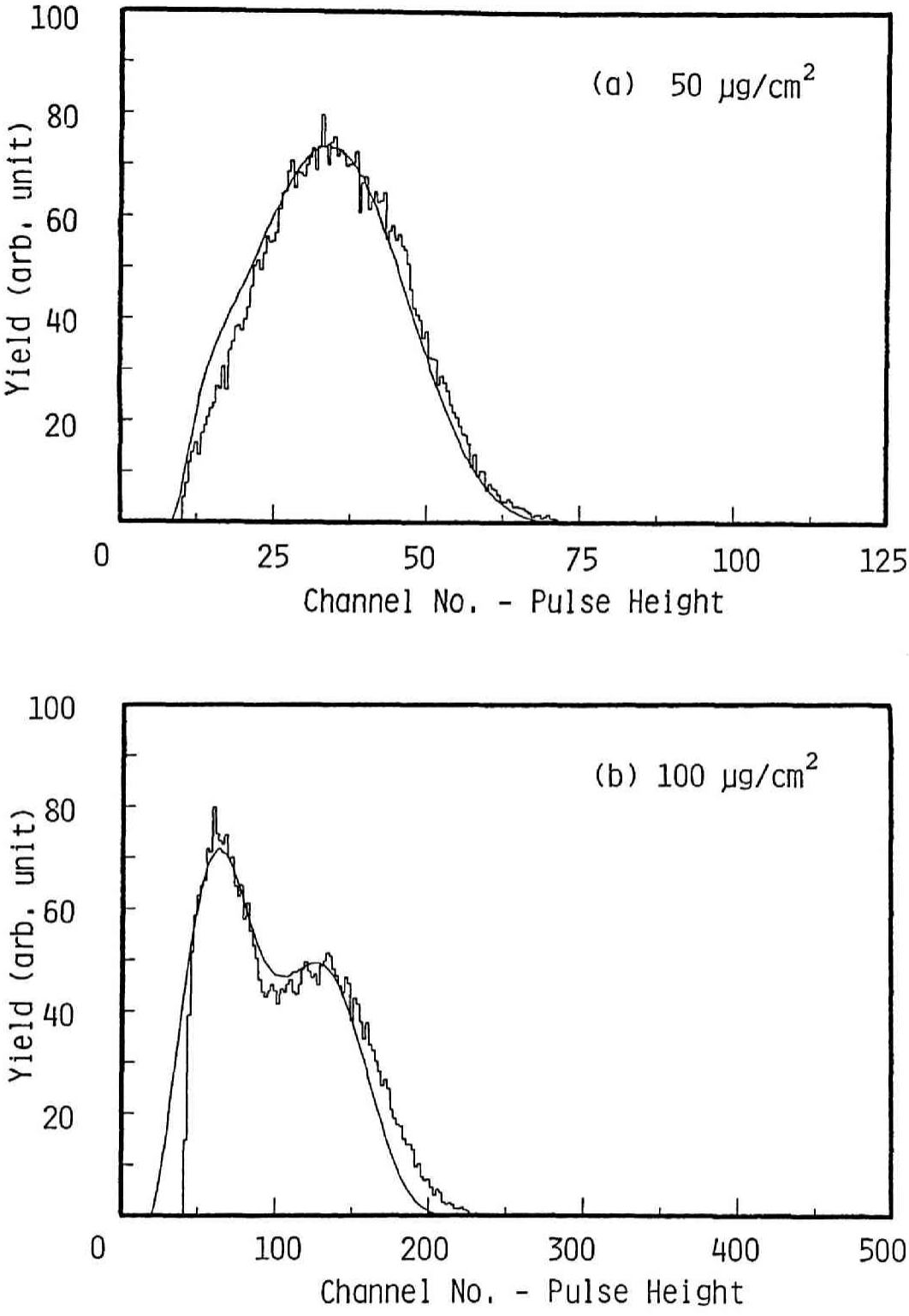

Fig.3.12 The calculated and experimental pulse height spectra of TFD for various film thickness. The spectra were obtained by fission fragments of the ^{252}Cf spontaneous fission at beam position 1. Fig.3.12(a) shows the case of a film thickness of 50$\mu g/cm^2$, (b) 100$\mu g/cm^2$. Solid lines represent the calculated results and histograms represent the experimental data.

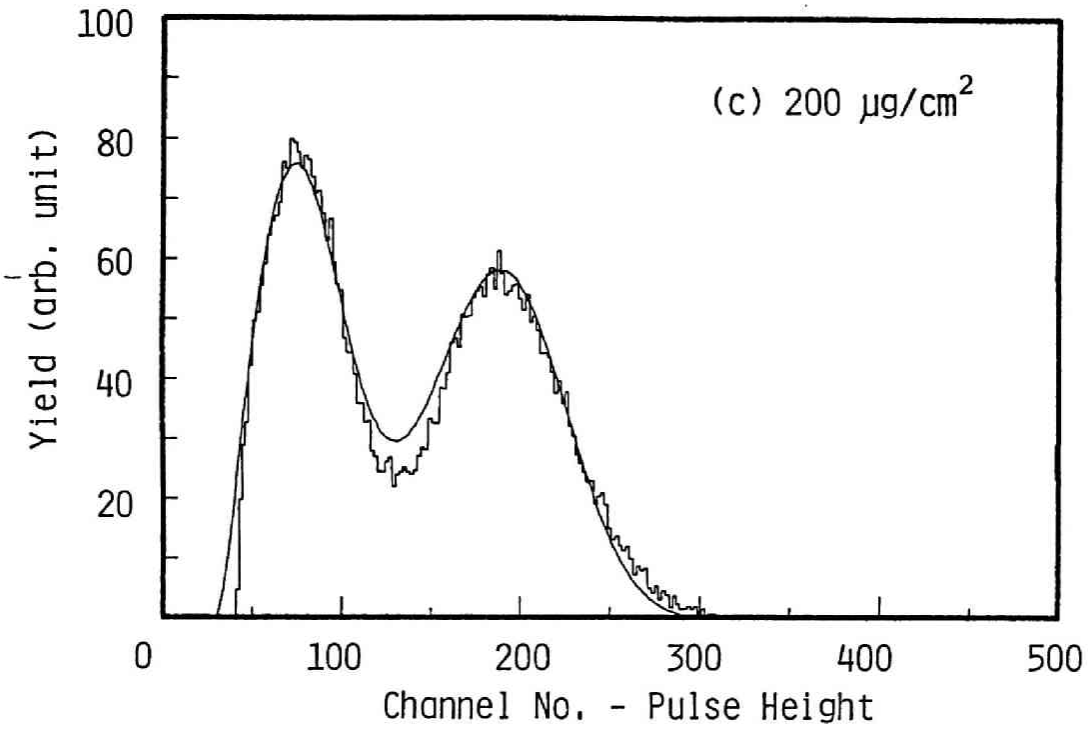

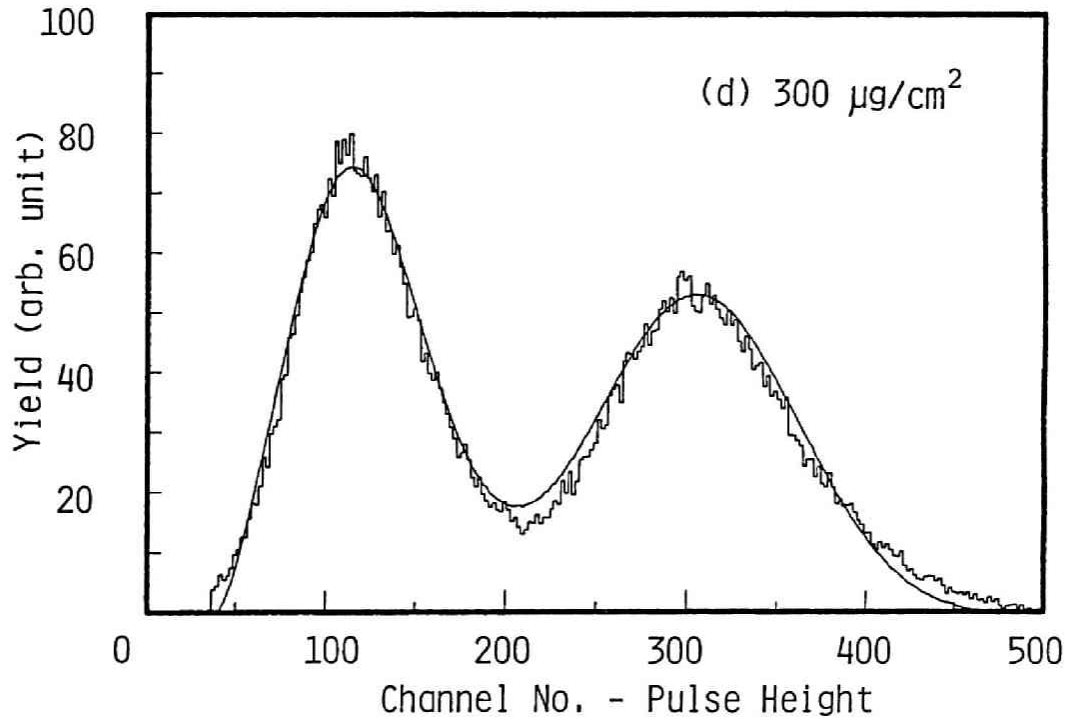

Fig.3 12 (continued) (c) 200$\mu g/cm^2$ and (d) 300$\mu g/cm^2$.

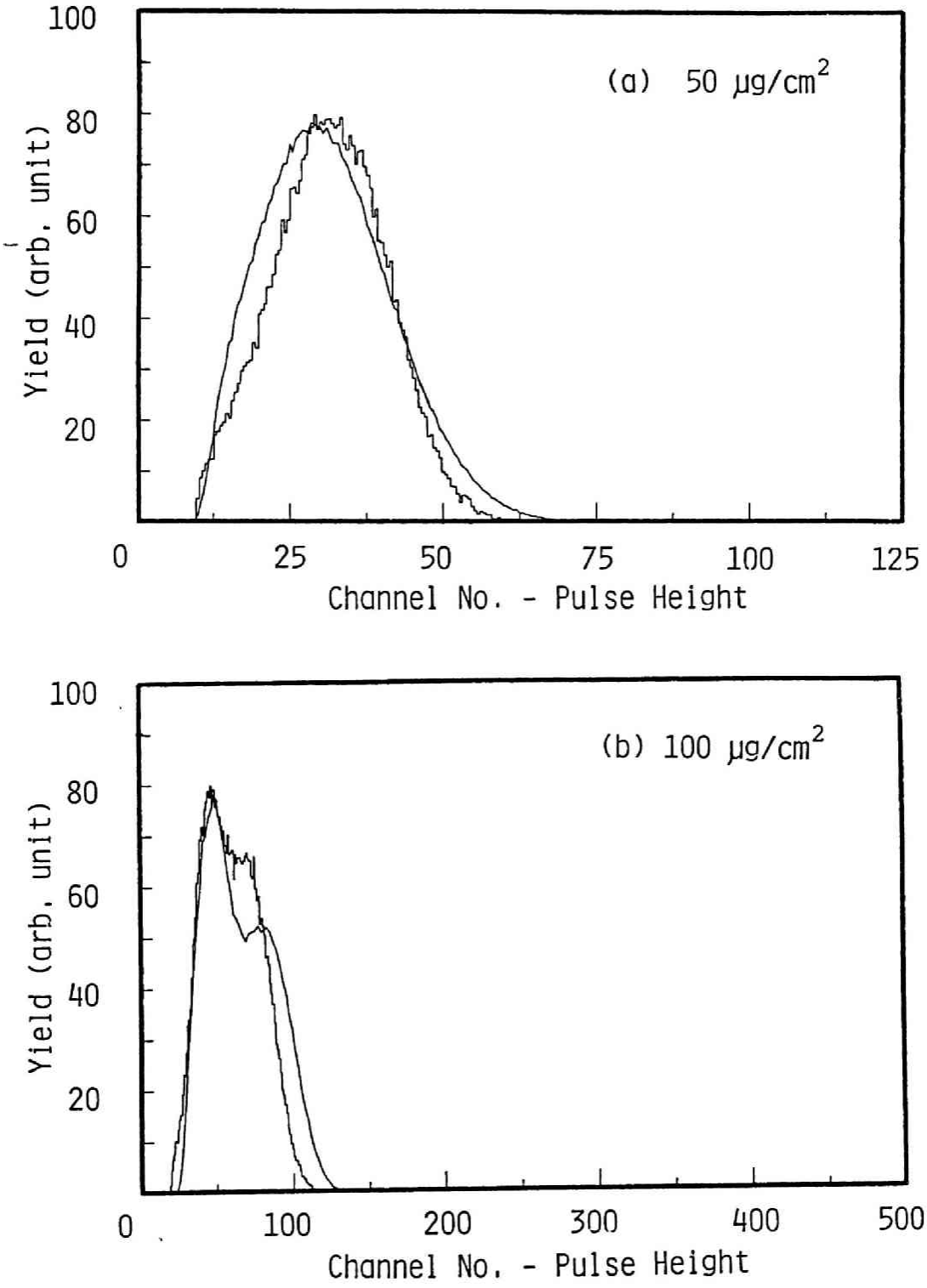

Fig.3.13 The same as in Fig.3.12 at beam position 3.

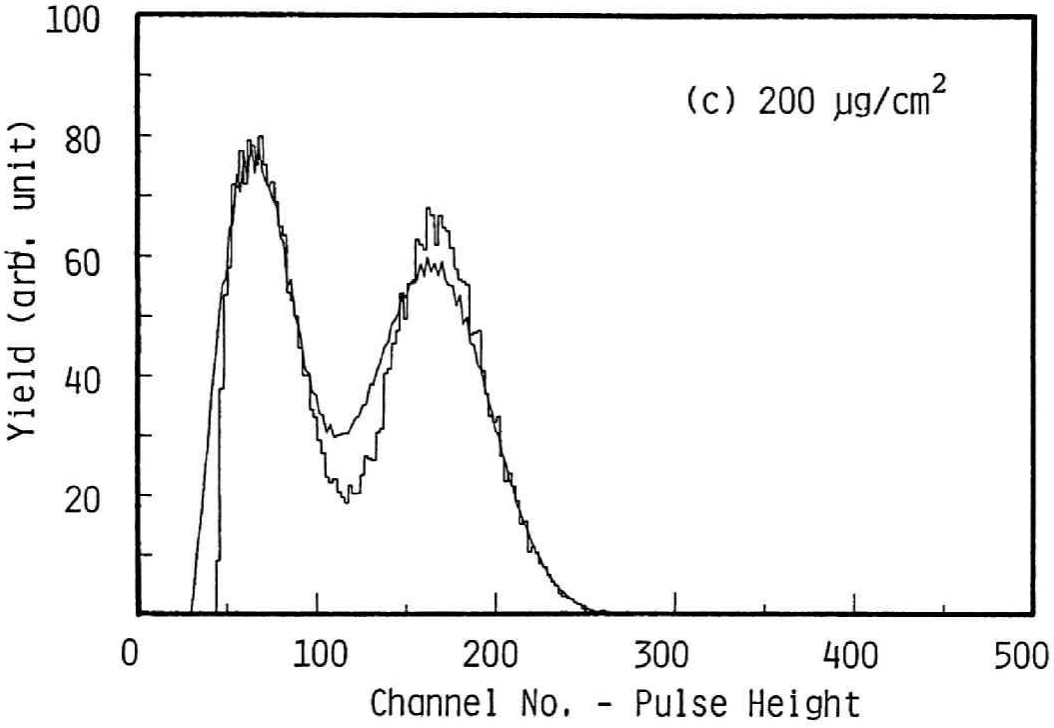

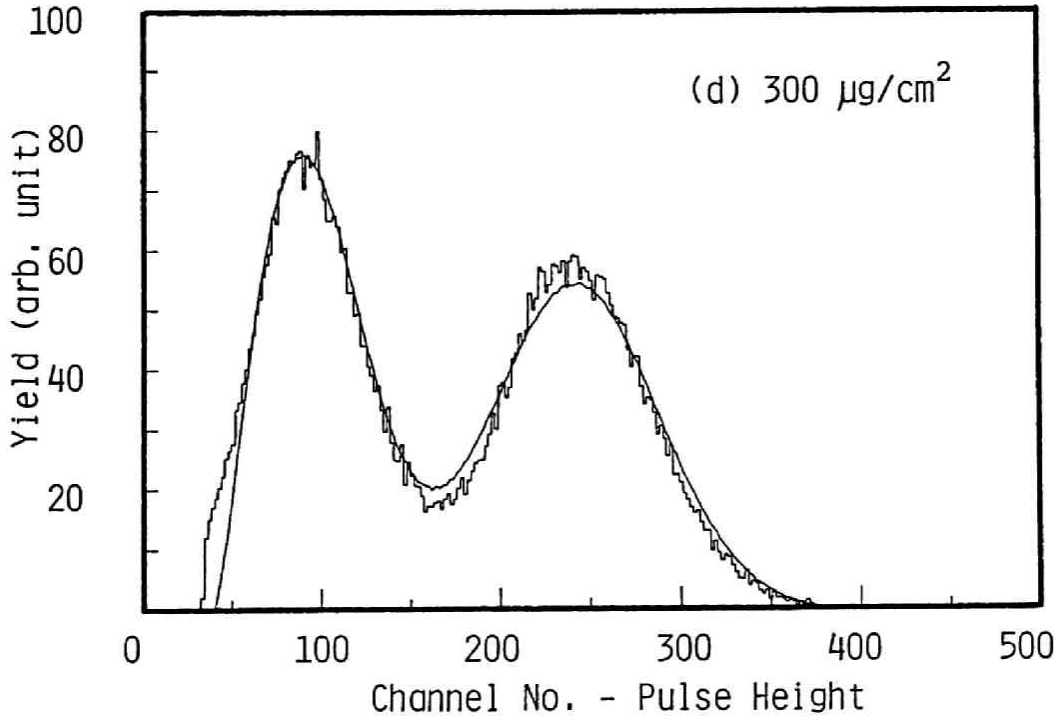

Fig.3.13 (continued)

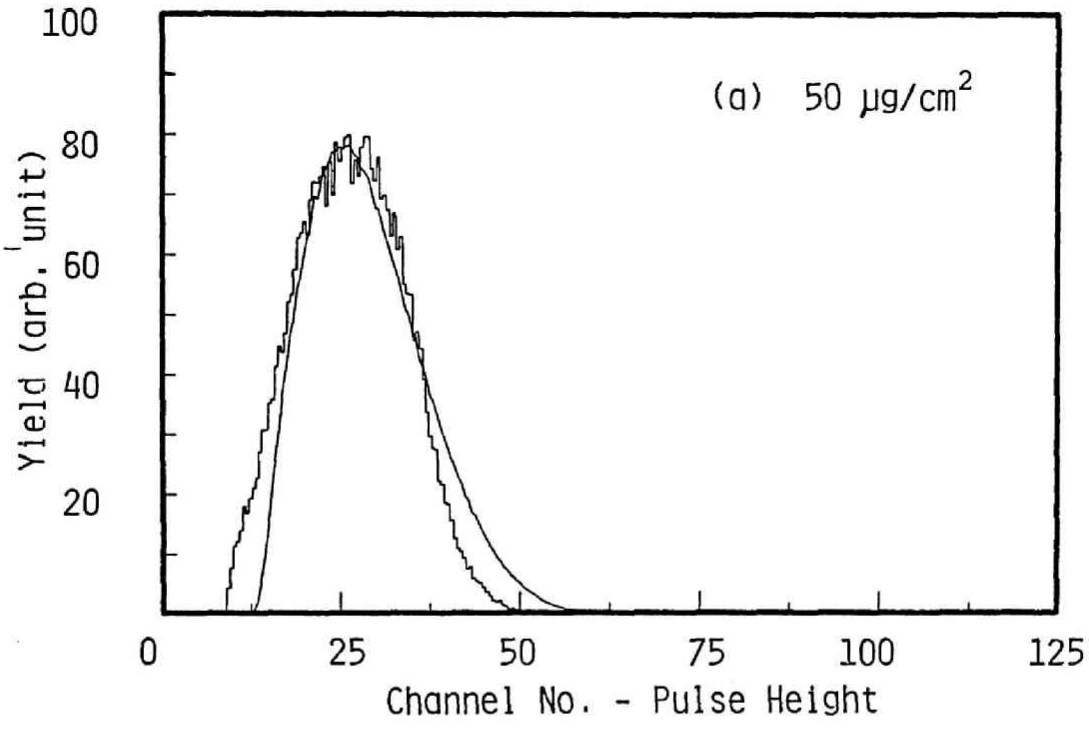

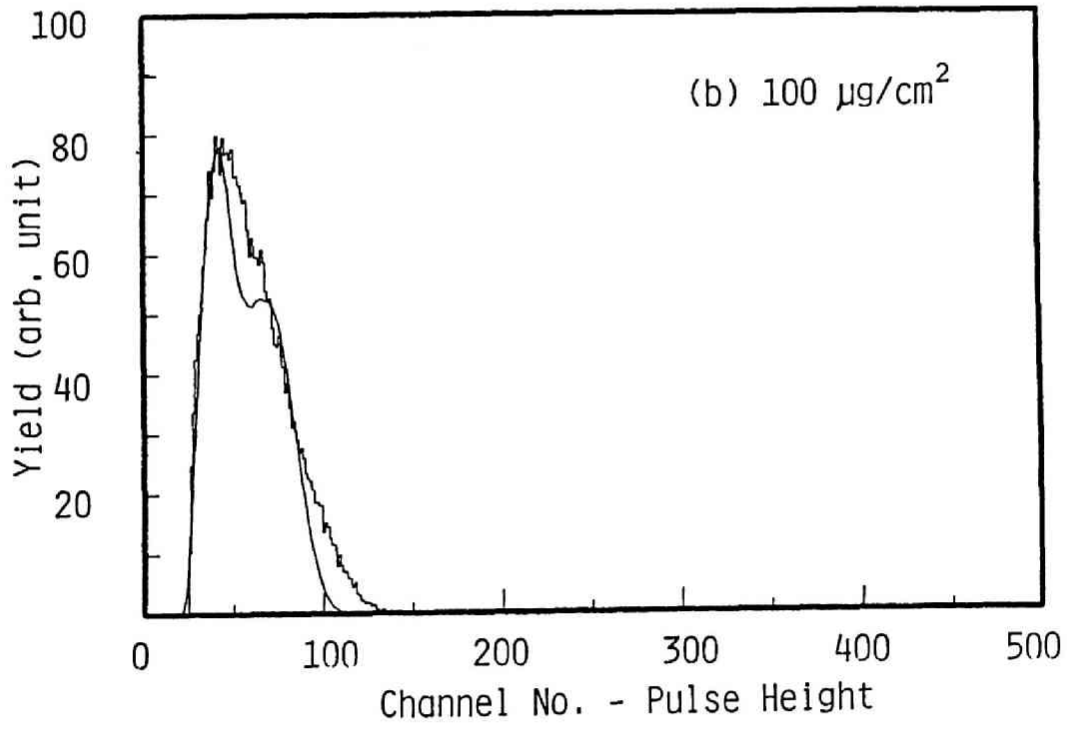

Fig.3.14 The same as in Fig.3.12 at beam position 5.

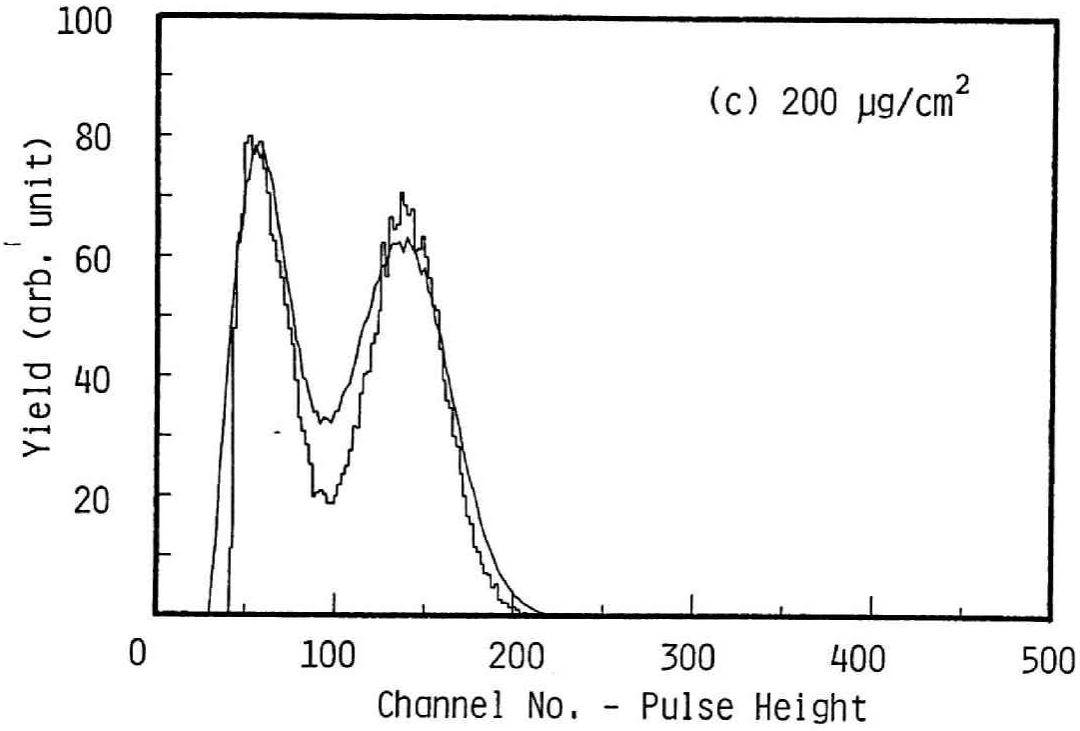

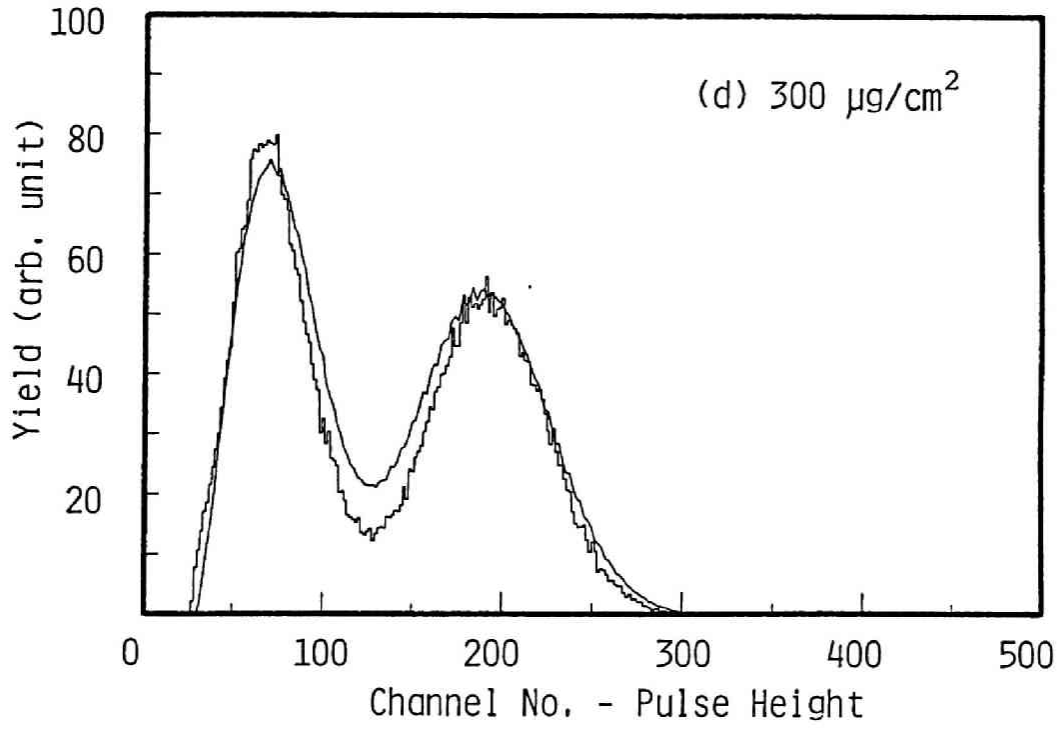

Fig.3.14 (continued)

4. Silicon surface barrier detector as a stop detector[1)]

4.1 Introduction

The silicon surface barrier detector (SSB) has been widely used for the measurement of charged particles in the last few decades because it is easy to handle and has excellent energy resolution. However, the SSB has two demerits for measurement of heavy ions; pulse height defect and plasma delay. The pulse height defect (PHD) results in the pulse height obtained from an SSB not being exactly proportional to the energy. The time delay of the signal from the ion incidence, called plasma delay, may range up to several nanoseconds. Both of these phenomena are ascribed to the formation of a plasma column in the silicon due to an incident heavy ion.

The PHD was observed in heavy ion measurements and a calibration method was proposed by Schmitt, *et al.*[2)]. Since then many researchers have investigated the PHD experimentally and theoretically. Wilkins, *et al.*[3),4)] studied the relationship between the energy response of the SSB for ions of He, C, O, Al, S, Ni, Ag, Au, I and U. Based on their experimental results, they proposed a new energy calibration method[5)]. Ndocko-Ndongue, *et al.*[6)] and Potter, *et al.*[7)] measured the PHD for ions of H, He, C, N, O, Ne, Mg, Al, Si, Ar, Fe and Kr at rather low energies. Kitahara, *et al* [8)] measured the PHD for much heavier ions like Kr, Xe, W, Bi and U. Finch, *et al.*[9)-11)] investigated the response of different types of SSBs to fission fragments. Very recently, they proposed an empirical calibration procedure for the PHD[12)]. Ogihara, *et al* [13)] measured the PHD for ^{12}C, ^{16}O, ^{28}S, ^{63}Cu, ^{79}Br and ^{127}I ions and proposed an empirical formula for the PHD.

All the authors separated causes of the PHD into three sources; (1) energy loss in the entry window, (2) energy loss by the nuclear stopping process and (3) energy dissipated by

the recombination of electron-hole pairs in the plasma column. Of the three sources of the defect, (1) and (2) can be reasonably understood by simple calculations. However, the recombination effect, which is understood qualitatively, has not been explained quantitatively. They have used the model of a qualitative plasma column proposed by Seibt, *et al.*[14] to calculate the recombination effect, but did not examine the plasma column formation.

The existence of the plasma delay was originally demonstrated by Alberigi Quaranta, *et al* [15] Since then, much work on the plasma delay has been carried out. Moszynski, *et al.*[16] measured the plasma delay for 5.7MeV alpha particles. Henschel, *et al* studied the plasma delay for the spontaneous fission fragments of ^{252}Cf[17] and observed the plasma delay directly[18),19]. Neidel, *et al.*[20] measured the plasma delay for protons, alpha particles and spontaneous fission fragments of ^{252}Cf and studied its dependence on the electric field strength. They also carried out an experiment on the plasma delay for ^{238}U ions with energies of 123MeV and 326MeV[21]. Butsch, *et al.*[22] observed the difference of the plasma delay between the isobars created in the reaction of ^{28}Si and ^{13}C. Recently, Bohne, *et al.*[23] carried out measurements of the dependence of the plasma delay on the kinetic energy and the electric field strength for alpha particles and ^{12}C, ^{20}Ne, ^{40}Ar and ^{129}Xe ions with various SSBs. This work showed that the plasma delay increases as the electric field strength increases, reaches a peak, and then decreases for higher fields. For all these particles except ^{129}Xe the plasma delay has a maximum value as a function of the electric field strength. They proposed an empirical formula for the plasma delay utilizing two linear functions for each charged particle

A theoretical model of the erosion of the plasma column was proposed by Seibt, *et al.*[14] and an improved model was reported by Finch[24], altering the formula for partially stripped ions and for totally stripped ions. However, they did not discuss the reason why the plasma column erodes. Both

models predicted an inverse electric field strength dependence of the plasma delay and could not explain the results of Bohne, *et al.*[23].

In order to estimate the recombination effect quantitatively and to explain the electric field strength dependence of the plasma delay, the author proposes here new models of the formation and erosion of the plasma column. With this model of the plasma column formation, the volume, the surface area of the plasma column and the density of the electron-hole pairs are calculated in Chapter 4.2. In the model of the erosion of the plasma column described in Chapter 4.3, it is postulated that the plasma delay is the time interval between the formation of the plasma column and the beginning of its erosion and that the erosion is caused by the change of the dielectric constant inside the plasma column, i.e., the change from a conductor-like plasma column to a dielectric-like one. With this model, the dependence on the electric field strength of the plasma delay is derived. In Chapter 4.4, the plasma delay is calculated and the result compared with the experiment of Bohne, *et al.*[23]. In Chapter 4.5, the recombination effect is described. The recombination effect can be calculated as the number of electron-hole pairs that recombine during the plasma delay time. However, the recombination calculation is difficult because of the lack of measurements of the plasma delay and recombination effects for the same charged particle with the same SSB. In this chapter, the recombination effect is calculated for the fission fragments of $^{235}U(n,f)$ and is compared with the experiment of Finch, *et al.*[11]. As an application of the study of Chapter 4.5, the energy calibration method for SSB which was proposed by Schmitt, *et al.*[2] is checked in Chapter 4.6. In Chapter 4.7, some conclusion are described.

4.2 A model of plasma column formation

The plasma column is composed of electron-hole pairs which are created by an incident ion. The plasma column formation is considered to occur in the following two steps; (1) electrons in the silicon are recoiled by the incident ions (recoiling primary electrons) and (2) the primary electron creates electron-hole pairs as it loses energy along its path.

(1) Primary electron recoil

The electrons in the silicon are recoiled by the heavy ion according to the Rutherford scattering cross section $d\sigma$,

$$d\sigma = \frac{1}{4}\left(\frac{e^2 Z_{eff}}{\mu V^2}\right)^2 \frac{d\theta}{sin^4(\theta/2)} = \sigma f(\theta) d\theta,$$

$$\sigma = \frac{1}{4}\left(\frac{e^2 Z_{eff}}{\mu V^2}\right)^2. \qquad (4-1)$$

In Eq.(4-1), V and Z_{eff} are the velocity and effective charge of the heavy ion, respectively, and μ is the reduced mass of the heavy ion with mass M and electron with mass m, which nearly equals m. The effective charge Z_{eff} is given as[25],

$$Z_{eff} = Z\{1-exp(-125\beta/Z^{2/3})\}, \qquad (4-2)$$

where β is the ratio of the velocity of the heavy ion to the velocity of light. Eq.(4-1) is rewritten using the relation

$$E = \frac{1}{2}kMV^2 \qquad (4-3)$$

as

$$\sigma = \frac{1}{4}\left(\frac{kMe^2 Z_{eff}}{2mE}\right)^2 \propto \left(\frac{MZ_{eff}}{E}\right)^2, \qquad (4-4)$$

where E is the energy of the heavy ion and k is the conversion constant from MKSA unit to cm, a.m.u., ns and MeV unit.

The electron energy E_e recoiled with an angle θ is given as[26]

$$E_e = 2m\left(\frac{M}{M+m}V cos\theta\right)^2 = \frac{4mE}{kM}cos^2\theta. \qquad (4-5)$$

The range of the primary electron R can be given by

$$R = gE_e = R_0 cos^2\theta, \qquad (4-6)$$

$$R_0 = R_0(E,M) = g\frac{4mE}{kM}. \qquad (4-7)$$

In Eq (4-7), g is 9.93×10^{-3}g/cm^{3}MeV[27] and R_0 is the primary electron range for the case of $\theta=0$. The region in which the primary electrons move is shown in Fig.4.1. We define this three dimensional region as $P(R_0,x)$, where x is the position of the incident ion in the SSB.

(2) Electron-hole pair creation

The primary electron is assumed to create an electron-hole pair along its path as it loses its 3.6eV of energy. The number of electron-hole pairs is given as a product of σ and the volume of the region $P(R_0,x)$. The volume of the region $P(R_0,x)$ is given as[28]

$$P(R_0,x) = \frac{2}{21}\pi R_0^3. \qquad (4-8)$$

The plasma column is obtained by superimposing the electron-hole pairs, the number of which is given as a function of the mass, charge and energy of the incident ion and its position in the SSB. The process of the formation of the plasma column is shown in Fig.4.2.

4.3 A model of plasma column erosion

In the plasma column formed by heavy charged particle like fission fragments, there exist high density electron-hole pairs and it is almost like a conductor. Electrons and holes inside the plasma column are not affected by the external electric field and the charge collection does not start until the electric field penetrates the plasma column. The plasma delay is the time interval from the plasma column formation to the beginning of its erosion.

The density of the electron-hole pairs is diluted by recombinations and by the enlargement of the plasma column radius, caused by diffusion of electrons and holes Because the number of the recombinations can be estimated to be only

a few percent of the total number of electron-hole pairs, as was seen in the work on the pulse height defect by Finch, *et al.*[11], enlargement of the radius must be the main source of the dilution.

The electric field strength F inside the cylindrical plasma column in an external field strength F_e is obtained, assuming that the plasma column is an infinite cylinder, as[29],

$$F = \frac{2\varepsilon}{\varepsilon' + \varepsilon} \cdot F_e \quad , \tag{4-9}$$

where ε is the dielectric constant of silicon, $\varepsilon = 12\varepsilon_0$ (ε_0 is the permittivity of free space), and ε' is the dielectric constant inside the plasma column. We assume the dielectric constant inside the plasma column is proportional to the electron-hole pair density,

$$\varepsilon' \fallingdotseq a\varepsilon_0 \cdot \frac{N}{\overline{r^2} l} \quad , \tag{4-10}$$

where a is a constant, $\overline{r^2}$ is the mean square radius of the plasma column, l is the length of the plasma column (range of the incident particle) and N is the number of electron-hole pairs at time t which is nearly equal to the initial number of electron-hole pairs, N_0. The mean square radius $\overline{r^2}$ is given as[30]

$$\overline{r^2} = 4D_a t + \overline{r_0^2} \quad , \tag{4-11}$$

where D_a is the ambipolar diffusion constant $16\mathrm{cm}^2/\mathrm{s}$[14] and $\overline{r_0^2}$ is the initial mean square radius of the plasma column. We assume here that the ambipolar diffusion constant D_a is given as a function of the electric field strength and the volume of the plasma column,

$$D_a = D_a(F_e, V) \quad . \tag{4-12}$$

The field strength inside the plasma column is written as

$$F = \frac{2\varepsilon}{a\varepsilon_0 \cdot N_0 / (4D_a(F_e, V)t + \overline{r_0^2}) l + \varepsilon} \cdot F_e \quad . \tag{4-13}$$

At $t = 0$, the electron-hole pair density is high, and the dielectric constant ε' is

$$\varepsilon'(t = 0) = a\varepsilon_0 \cdot \frac{N_0}{\bar{r}_0^2 l} \gg \varepsilon \ . \qquad (4-14)$$

By substituting Eq.(4-14) into Eq.(4-13), field strength F at the time $t = 0$ becomes

$$F \fallingdotseq 0 \ . \qquad (4-15)$$

The author assumes here that the electron and hole collection starts when the internal electric field strength reaches a certain value F_i,

$$\frac{2\varepsilon}{a\varepsilon_0 \cdot N_0 / (4D_a(F_e, V)t + \bar{r}_0^2) l + \varepsilon} \cdot F_e = F_i \ . \qquad (4-16)$$

Solving for t, the plasma delay is obtained as

$$t = \frac{1}{4D_a(F_e, V)} \cdot \left\{ \frac{aF_i\varepsilon_0 N_0}{(2F_e - F_i)\varepsilon l} - \bar{r}_0^2 \right\} \ . \qquad (4-17)$$

Next, let us consider the characteristics of the ambipolar diffusion constant, $D_a(F_e, V)$. The plasma column cannot enlarge itself freely because of the Maxwell's stress which depends on the electric field strength as F_e^2 Therefore, we assume an inverse F_e^2 dependence of D_a. The electrons and holes diffuse more when the volume of the plasma column is larger. Then we write the ambipolar diffusion constant as

$$D_a(F_e, V) = \frac{D_a V}{c F_e^2} \ , \qquad (4-18)$$

where c is a normalization factor. With Eqs.(4-17) and (4-18), we obtain the plasma delay,

$$t = c \cdot \frac{F_e^2}{4D_a V} \left\{ \frac{aF_i\varepsilon_0 N_0}{(2F_e - F_i)\varepsilon l} - \bar{r}_0^2 \right\} \ . \qquad (4-19)$$

The differential of the plasma delay against the electric field strength is

$$\frac{dt}{dF_e} = c \cdot \frac{F_e}{2D_a V (2F_e - F_i)^2 \varepsilon l} \left\{ a\varepsilon_0 N_0 F_i (F_e - F_i) - \bar{r}_0^2 \varepsilon l (2F_e - F_i)^2 \right\} \ . \qquad (4-20)$$

By the assumption of $F_e >> F_i$, we can obtain the following results,

$$\text{at} \quad F_e \leqq \frac{aF_i\varepsilon_0 N_0}{4\varepsilon l \bar{r}_0^2} \ , \qquad \frac{dt}{dF_e} \geqq 0 \ , \qquad (4-21)$$

and

$$\text{at} \quad F_e > \frac{aF_i\varepsilon_0 N_0}{4\varepsilon l \bar{r}_0^2} , \qquad \frac{dt}{dF_e} < 0 . \tag{4-22}$$

These relations show the experimental results of Bohne, *et al.*[23], *i.e.*, that the plasma delay increases as $1/F_e$ increases and it decreases when $1/F_e$ is greater than some value.

4.4 Plasma delay

In order to calculate the plasma delay expressed by Eq.(4-19), the number of electron-hole pairs, the radius and length of the plasma column should be known and the constants a and F_i must be determined.

For the comparison with the experiment carried out by Bohne, *et al.*[23], the radius, length of the plasma column and the number of electron-hole pairs were calculated for alpha particles with energy of 8.78MeV, ^{40}Ar with energies of 268MeV and 476MeV and ^{129}Xe with energy of 166MeV. The calculated results are shown in Table 4.1 and some examples of the plasma column are shown in Fig 4.3

The constant aF_i was determined from the relations (4-21) and (4-22) with the external field strength F_e which gives the maximum plasma delay in Fig.5 of Ref.(23). The values of aF_i obtained for each charged particle are given in the eighth row of Table 4.1. With these values, the plasma delay was calculated for the charged particles as a function of inverse electric field strength. The normalization constant c is determined by fitting the calculated results to the 0.265cm/kV point for alpha particles, 0.23cm/kV for 268MeV ^{40}Ar, 0.193cm/kV for 476MeV ^{40}Ar and 0.15cm/kV for ^{129}Xe. The values of c are shown in the bottom row of Table 4.1.

The calculated plasma delays against inverse field strength for alpha particles, ^{40}Ar and ^{129}Xe are plotted in Fig.4.4 with the experimental values of Bohne, *et al.*[23].

The calculated and experimental results for alpha particle

and ^{40}Ar agree well. The reason that the maximum plasma delay exists is explained intuitively as follows. In the case of low electric field strength, the plasma column enlarges itself rapidly because of weak Maxwell's stress and the density of electron-hole pairs becomes low enough to be collected. If the electric field strength is very strong, the electrons and holes are attracted to the electrodes before the volume of the plasma column becomes large

In the case of ^{129}Xe, the experimental data does not show the behavior described above. This phenomenon is understood as follows. For a plasma column with a high density of electron-hole pairs, the Maxwell's stress cannot affect its strength enough to be written as F_e^2, but rather is in a weaker form, F_e. Assuming that the effective Maxwell's stress shows F_e dependence, the ambipolar diffusion constant will be expressed as

$$D_a(F_e, V) = \frac{D_a V}{c' F_e} \quad , \tag{4-23}$$

where c' is a normalization factor With this assumption, the plasma delay is given by

$$t = c' \cdot \frac{F_e}{4 D_a V} \left\{ \frac{a F_i \varepsilon_0 N_0}{(2F_e - F_i) \varepsilon l} - \bar{r}_0^2 \right\} \quad , \tag{4-24}$$

and the differential against the electric field strength is

$$\frac{dt}{dF_e} = - c' \cdot \frac{a F_i^2 \varepsilon_0 N_0 + \bar{r}_0^2 \varepsilon l (2F_e - F_i)^2}{4 D_a V (2F_e - F_i)^2 \varepsilon l} < 0 \quad . \tag{4-25}$$

The plasma delay decreases monotonously as the electric field strength increases The calculated plasma delay assuming $1/F_e$ dependence of the ambipolar diffusion constant is also plotted in Fig.4.4 as the dashed line. This dashed line shows good agreement with the experimental data. The calculated results are normalized to the 0.15cm/kV point.

The constant aF_i must be common to all the charged particles. However, aF_i is greater when the plasma column has low electron-hole pair density This means that the dielectric constant depends slightly on the electron-hole pair density. In other words, in the case of high density, sat-

uration of the dielectric constant occurs. On the other hand, the values of c are almost equal to 1×10^{-10}. This shows the validity of the derived formula.

4.5 Recombination effect

The recombination effect can be calculated as the number of electrons and holes which recombine during the time interval of the plasma delay. However, no data has been reported which measured both the plasma delay and the recombination effect simultaneously. Because of this lack of appropriate data, the author performs the calculation of the recombination effect using parameters derived in the following chapter.

In order to compare the calculation to the experimental result by Finch, *et al.*[11], we calculated the number of electron-hole pairs, volume and surface area of the plasma column for the fission fragments of ^{235}U with mass numbers of 90, 101 and 135 The proton numbers of the fragments are assumed to be proportional to the ratio of the proton number to the mass number of the fissioning nucleus ^{236}U. We compare the calculation to the measurement with a bias voltage of 84V in the work of Finch, *et al.*[11].

The plasma columns formed by the fragments of mass number 90 with energy 94MeV, mass number 101 with 94MeV and mass number 135 with 65.7MeV are shown in Figs.4.5 (a), (b) and (c), respectively. Contours on the figures show equi-density regions of electron-hole pairs. The calculated results are shown in Table 4.2. According to Ref (11), the fragment with mass number 90 and incident energy 94MeV, for example, loses 0.52MeV energy in the gold entry window of the SSB and 1.56MeV in nuclear stopping process and consumes the rest of the incident energy 91.92MeV to create electron-hole pairs. The number of the electron-hole pairs are calculated so that the fragment with residual energy of

91.92MeV produces an electron-hole pair every 3.6eV. The averaged density of the electron-hole pairs is also calculated.

Here, the author introduces the product of the surface area and the average density as a parameter $N(M,E)$ to express the recombination effect, where M and E are the mass number and the energy of the fragment. With this parameter $N(M,E)$, the recombination effect $\Delta_r(M,E)$ is calculated for each fragment as a ratio to the $N(M,E)$ with the smallest energy E_{min} as

$$\Delta_r(M,E) = \frac{N(M,E)}{N(M,E_{min})} \Delta_{r,exp}(M,E_{min}), \qquad (4-26)$$

where $\Delta_{r,exp}$ means the recombination effect obtained experimentally in Ref.(11). The calculated recombination effect is shown in the bottom row in the Table 4.2 and Fig.4.6 The calculated values show very good agreement to the experimental ones as seen by comparing the second to the bottom row in Table 4.2.

The relative recombination effect for the two fragments is derived using the ratio of the density of the electron-hole pairs to the range of the fragment, $\rho(M,E)$. For example, the recombination effect of the fragment of mass 101 and energy 72.8MeV is calculated using that of the fragment of mass 90 and energy 72.8MeV as

$$\Delta_r(101,72.8) = \frac{N(101,72.8)}{N(90,72.8)} \cdot \frac{\rho(101,72.8)}{\rho(90,72.8)} \Delta_{r,exp}(90,72.8), \qquad (4-27)$$

The recombination effect of the fragment of mass 101 is explained fairly well with the method described above, however this method overestimates in the case of the fragment of mass 135.

As is shown in Fig.4.5, the density of electron-hole pairs in a region of the plasma column depends on the position of the region. This change of the density will have some effect on the recombination, however the simply averaged density and the surface area explain the recombination effect very well.

The physical meaning of the parameter $N(M,E)$ is the

linear number density of the electron-hole pairs in the radial direction at the surface of the plasma column. This suggests that the plasma erosion starts from the surface of the plasma column by a small amount of diffusion. The plasma column erodes rapidly after the density of the electron-hole pairs decreases to some extent with the recombination and enlargement of the volume of the plasma column.

The overestimation of the recombination effect of the fragment of mass 135 predicted by other fragments' recombination effect suggests a saturation of the recombination with the high density of electron-hole pairs. This saturation effect prolongs the time which is needed to decrease the electron-hole pair density significantly.

4.6 Check of the calibration formula of Schmitt, *et al.*

4.6.1 Method

As described in the introduction of this chapter, the calibration formula of Schmitt, *et al.*[2] has been widely used for the correction of the pulse height defect. In order to use the calibration formula for the analysis of the double-energy double-velocity measurement, the author checked the validity of the formula.

The calibration formula of Schmitt, *et al.* is given as follows:

$$E = (a + a'm)\cdot x + b + b'm, \tag{4-28}$$

$$a = \frac{c_1}{(P_L - P_H)}, \tag{4-29}$$

$$a' = \frac{c_2}{(P_L - P_H)}, \tag{4-30}$$

$$b = d_1 - a\cdot P_L, \tag{4-31}$$

$$b' = d_2 - a'\cdot P_L, \tag{4-32}$$

where E is the energy of the heavy ion measured by an SSB, m is the mass number, x is the pulse height, a, a', b and b'

are constants which depend on the pulse heights of light fragment peak P_L and heavy fragment peak P_H. Also, c_1, c_2, d_1 and d_2 are the constants measured for fissiles. Schmitt, *et al*. determined c_1, c_2, d_1 and d_2 by means of ^{79,81}Br and ^{127}I ions, which had the same pulse heights for the heavy and light fragment peaks. For example, the values of the constants c_1, c_2, d_1 and d_2 for the fission fragments of the spontaneous fission of ^{252}Cf are 24.0203, 0.03574, 89.6083 and 0.1370. As the first step of checking the calibration formula, the author calculates the energies of ^{79,81}Br and ^{127}I ions which give the same energy pulse height as the heavy and light fragment peaks of the spontaneous fission fragment of ^{252}Cf. Next, the plasma columns are calculated for the ions described above and for the fission fragments correspond to the light and heavy fragment peaks. Finally, the residual energies are calculated by subtracting the recombination effect, the energy loss in the entrance window and the energy loss by nuclear collision from the initial energies for each charged particles and are compared with one another.

4.6.2 Derivation of the energy of the charged particles

The energy spectrum of the spontaneous fission fragment of ^{252}Cf was taken from the work of Schmitt, *et al*.[31]. The channel numbers of the heavy and light fragment peaks were 99 and 147, respectively. The mass numbers and kinetic energies of the representatives of the heavy and light fragment peaks were obtained from the same work as 142.3amu and 79.1MeV for heavy fragments and 106.1amu and 105.1MeV for light fragments, respectively. The energies of ^{79,81}Br and ^{127}I ions which corresponded to the peaks of heavy and light fragments were calculated by Eqs.(4-28)-(4-32) as 73.7MeV and 100.6MeV for ^{79,81}Br and 78.5MeV and 107.0MeV for ^{127}I

4.6.3 Calculations

With the model of the plasma column formation, the number of electron-hole pairs, volume, surface area and length of the plasma column were calculated for heavy ions as described in Chapter 4.6.1. The results of the calculations are shown in Table 4.3. The energy losses of the heavy ions in the gold entrance window ($40\mu g/cm^2$), Δ_w, were calculated by Bethe's formula. The energy losses by nuclear collision, Δ_n, were obtained by inter- and extra-polations of the results of Finch, *et al.*[11]. The numbers of electron-hole pairs were calculated by assuming the residual energies after subtracting the calculated energy losses described above from the initial energies produced electron-hole pairs every 3.6eV. Because of the lack of the experimental data on the recombination effect on $^{79,81}Br$ and ^{127}I ions, the author used Eq.(4-27) assuming that the residual energies of both ions were equal For heavy ions which formed plasma columns with densities of electron-hole pairs greater than $10^{22}n/cm^3$, a reducing factor 0.84 was used for the calculations of the recombination effect as described in Chapter 4.5. The residual energies of each heavy ions are listed in the bottom row of Table 4.3. For the light fragment peak, the calculated residual energy (pulse height) is 1.0MeV greater than those of $^{79,81}Br$ and ^{127}I ions, while for heavy fragment peak, the results agree quite well. The poor agreement of the recombination effect of light fragments might be caused by the reducing factor However, the author concludes that the consistency between the calibration formula of Schmitt, *et al.*[2] and the recombination model is fairly satisfactory.

4.7 Conclusion

(1) Quantitative models for the formation and erosion of the plasma column were proposed for the first time. With

this model for the plasma column formation, the volume and surface area of the plasma column and the number and density of the electron-hole pairs were calculated. From this calculation, the density of the electron-hole pairs was found to be greater than that in the work of Seibt, *et al*.[14] which was derived from a qualitative estimate of the plasma column diameter

(2) The cause of the erosion of the plasma column has not been discussed in earlier papers In this chapter, the author proposes that the change of the dielectric quality of the plasma column caused by the diffusion of the electrons and holes with time is the trigger of the erosion process.

(3) The plasma delay, which is calculated as the time interval between the formation and start of erosion of the plasma column, is affected by the ambipolar diffusion constant. The author has examined the electric field dependence of the ambipolar diffusion constant as a function of the density of electron-hole pairs of the plasma column; however, further study must be carried out on the ambipolar diffusion constant as a function of the density of charge carriers.

(4) The recombination effect was estimated quantitatively using two derived parameters, because of the lack of appropriate measurements relating the plasma delay to the recombination effect. In future studies, recombination effects should be calculated directly using data for the plasma delay and the rate of electron/hole recombination.

(5) The calibration formula of the pulse height defect proposed by Schmitt, *et al* was checked using the model of the recombination effect. This model explained the calibration formula fairly well.

(6) The author requests that experimental researchers perform experiments both on plasma delay and on recombination effect with the same charged particle and energies.

References

1) Kanno, I.: Rev. Sci. Instrm., in press.
2) Schmitt, H. W., Gibson, W. M., Neiler, J. H., Walter, F. J. and Thomas, T. D.: "Proceedings of the Symposium on Physics and Chemistry of Fission", Salzburg, IAEA, Vienna, Vol.I, p 531 (1965).
3) Wilkins, B. D., Fluss, M. J., Kaufman, S. B., Gross, C. E. and Steinberg, E. P.: Nucl. Instr. and Meth., **92**, 381 (1971).
4) Steinberg, E. P., Kaufman, S. B., Wilkins, B. D. and Gross, C. E.: Nucl. Instr. and Meth., **99**, 309 (1977).
5) Kaufman, S. B., Steinberg, E. P., Wilkins, B. D., Unik, J , Gorski, A. J and Fluss, M. J : Nucl. Instr. and Meth., **115**, 47 (1974).
6) Ndocko-Ndongue, V. B., Pape, A. J. and Armbruster, R.: J. Phys. C: Solid State Phys., **11**, 1733 (1978).
7) Potter, D. W. and Campbell, R. D.: Nucl. Instr. and Meth., **153**, 525 (1978).
8) Kitahara, T , Geissel, H., Laichter, Y. and Armbruster, P.: Nucl. Instr. and Meth., **113**, 317 (1973).
9) Finch, E. C.: Nucl. Instr. and Meth., **113**, 41 (1973).
10) Finch, E. C., Asghar, M., Forte, M., Siegert, G., Greif, Decker, R. and 'Lohengrin Collaboration': Nucl Instr and Meth., **142**, 539 (1977).
11) Finch, E. C., Asghar, M. and Forte, M.: Nucl. Instr. and Meth., **163**, 467 (1979).
12) Finch, E. C., Goennenwein, F., Geltenbort, P., Oed, A. and Weissenberger, E.: Nucl. Instr. and Meth., **228**, 402 (1985).
13) Ogihara, M., Nagashima, Y., Galster, W. and Mikumo, T.: Nucl Instr. and Meth., **A251**, 313 (1986).
14) Seibt, W., Sundstroem, K. E. and Tove, P. A.: Nucl. Instr. and Meth., **113**, 317 (1973).
15) Quaranta, A. A., Taroni, A. and Zanarini, G.: Nucl. Instr. and Meth., **72**, 72 (1969).
16) Moszynski, M. and Bengston, B.: Nucl Instr. and Meth.,

91, 73 (1971).
17) Henschel, H., Hipp, H., Kohnle, A. and Goennenwein, F.: Nucl. Instr. and Meth., **125**, 365 (1975).
18) Henschel, H. and Schmidt, R.: Nucl. Instr. and Meth., **151**, 529 (1978).
19) Hannappel, L., Henschel, H. and Schmidt, R.: Nucl. Instr. and Meth., **151**, 537 (1978).
20) Neidel, H. -O. and Henschel, H.: Nucl. Instr. and Meth., **178**, 137 (1980).
21) Neidel, H. -O., Henschel, H., Geissel, H. and Laichter, Y.: Nucl. Instr. and Meth., **212**, 299 (1983).
22) Butsch, R., Pochodzalla, J. and Heck, B.: Nucl. Instr. and Meth., **228**, 586 (1985).
23) Bohne, W., Galster, W., Grabisch, K. and Morgenstern, H.: Nucl. Instr. and Meth., **A240**, 145 (1985).
24) Finch, E. C.: Nucl. Instr. and Meth., **121**, 431 (1974).
25) Barkas, W. H.: "Nuclear Research Emulsions", Academic Press, New York, Vol.I, p.371 (1963).
26) Weber, K. H.: Nucl. Instr. and Meth., **25**, 261 (1964).
27) Kobetich, E. J. and Katz, R.: Phys Rev , **170**, 391 (1968).
28) Kanno, I and Nakagome, Y.: Nucl. Instr. and Meth., **A244**, 551 (1986).
29) Landau, L. D. and Lifshitz, E. M.: "Electrodynamics of Continuous Media", Pergamon Press, London, p.43 (1960).
30) Tove, P. A. and Seibt, W.: Nucl. Instr. and Meth., **51**, 261 (1967).
31) Schmitt, H. W., Neiler, J. H. and Walter, F. J.: Phys. Rev., **141**, 1146 (1966).

Table 4.1 The number of electron-hole pairs, volume and surface area of the plasma column formed by 8.78MeV alpha particles, 268MeV and 476MeV ^{40}Ar ions and 166MeV ^{129}Xe ions. The meanings of αF_i and c are explained in the text.

Particles	α	^{40}Ar		^{129}Xe
Energy (MeV)	8.78	268	476	166
Range (cm)	5.76E-03	7.28E-03	1.57E-02	1.97E-03
Pairs	2.44E+06	7.39E+07	1.32E+08	4.56E+07
Volume (cm^3)	1.45E-13	1.69E-12	1.23E-11	9.26E-15
Density (n/cm^3)	1.71E+19	4.34E+19	1.07E+19	4.92E+21
Surface (cm^2)	8.99E-08	3.37E-07	1.36E-06	1.16E-08
αF_i	2.28E-18	1.51E-18	6.45E-18	1.23E-20
c	1.15E-10	1.12E-10	7.05E-11	-

Table 4.2 Calculated results of the plasma column and recombination effect for fission fragments. The experimental results in the second row are taken from the work of Finch, *et al.*[11]. $N(M,E)$ is the product of surface area and electron-hole density. The calculation method to derive the value in the bottom row is described in the text.

Fragments	M=90				M=101			M=135			
Energy (MeV)	50.6	72.8	78.9	94.0	72.8	78.9	94.0	50.6	55.6	60.7	65.7
Exp.[11] (MeV)	1.01	1.29	1.32	1.42	2.09	2.16	2.38	3.00	3.18	3.41	3.67
Range ($*10^{-4}$ cm)	12.1	14.4	15.5	16.6	13.9	14.7	16.1	11.8	11.8	12.1	12.1
Pairs ($*10^{7}$)	1.07	1.78	1.99	2.55	1.86	2.09	2.68	1.27	1.44	1.64	1.85
Volume ($*10^{-16}$ cm^3)	15.1	32.3	37.7	57.4	25.2	30.5	43.5	7.98	9.20	10.9	12.6
Density ($*10^{21}$ n/cm^3)	7.09	5.51	5.28	4.44	7.38	6.85	6.16	15.9	15.7	15.0	14.7
Surface ($*10^{-9}$ cm^2)	3.80	5.97	6.64	8.48	5.22	5.85	7.29	2.61	2.81	3.09	3.44
N(M,E) ($*10^{13}$ n/cm)	2.69	3.29	3.51	3.77	3.85	4.01	4.49	4.15	4.41	4.64	5.06
Calculation (MeV)	1.01	1.24	1.32	1.42	2.09	2.18	2.44	3.00	3.19	3.35	3.66

Table 4.3 Calculated results of the plasma column and the recombination effect for ^{79,81}Br ions, ^{127}I ions and the representatives of heavy and light fragment of the spontaneous fission of ^{252}Cf. Δ_w and Δ_n are the energies of the charged particles lost in the gold window of SSB and by the nuclear collision. $N(M,E)$ and $\rho(M,E)$ are the products of surface area and the density of electron-hole pair and the density divided by the range. Δ_r is the calculated recombination effect. The residual energy listed in the bottom row means the energy of charged particle after subtracting Δ_w, Δ_n and Δ_r.

Particles	^{79,81}Br		^{127}I		Heavy	Light
Energy (MeV)	73.7	100.6	78.5	107.1	79.1	105.1
Δ_w (MeV)	0.53	0.64	0.52	0.73	0.47	0.67
Δ_n (MeV)	1.54	1.57	2.36	2.39	2.89	1.92
Range ($*10^{-4}$ cm)	14.1	17.1	12.7	15.2	13.8	16.7
Pairs ($*10^{7}$)	2.00	2.74	2.09	2.89	2.10	2.84
Volume ($*10^{-16}$ cm^3)	39.7	82.7	19.0	36.0	17.1	51.3
Density ($*10^{21}$ n/cm^3)	5.04	3.31	11.0	8.03	12.3	5.54
Surface ($*10^{-9}$ cm^2)	6.44	10.2	4.31	6.33	4.16	8.05
N(M,E) ($*10^{13}$ n/cm)	3.24	3.38	4.74	5.08	5.11	4.46
ρ(M,E) ($*10^{24}$ n/cm^4)	3.57	1.94	8.66	5.28	8.91	3.32
Δ_r (MeV)	1.62	2.11	4.82	7.21	5.36	4.76
Residual Energy (MeV)	70.0	96.3	70.8	96.8	70.4	97.8

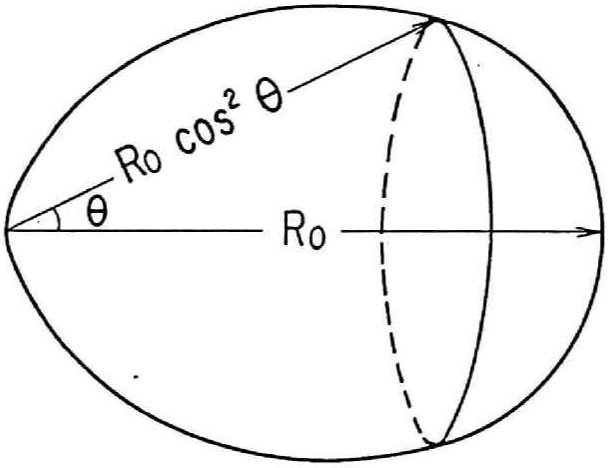

Fig.4.1 Three dimensional region in which primary electron recoiled at position x by a heavy ion can move. R_0 is the maximum range of the primary electron and is a function of mass and energy of the heavy ion.

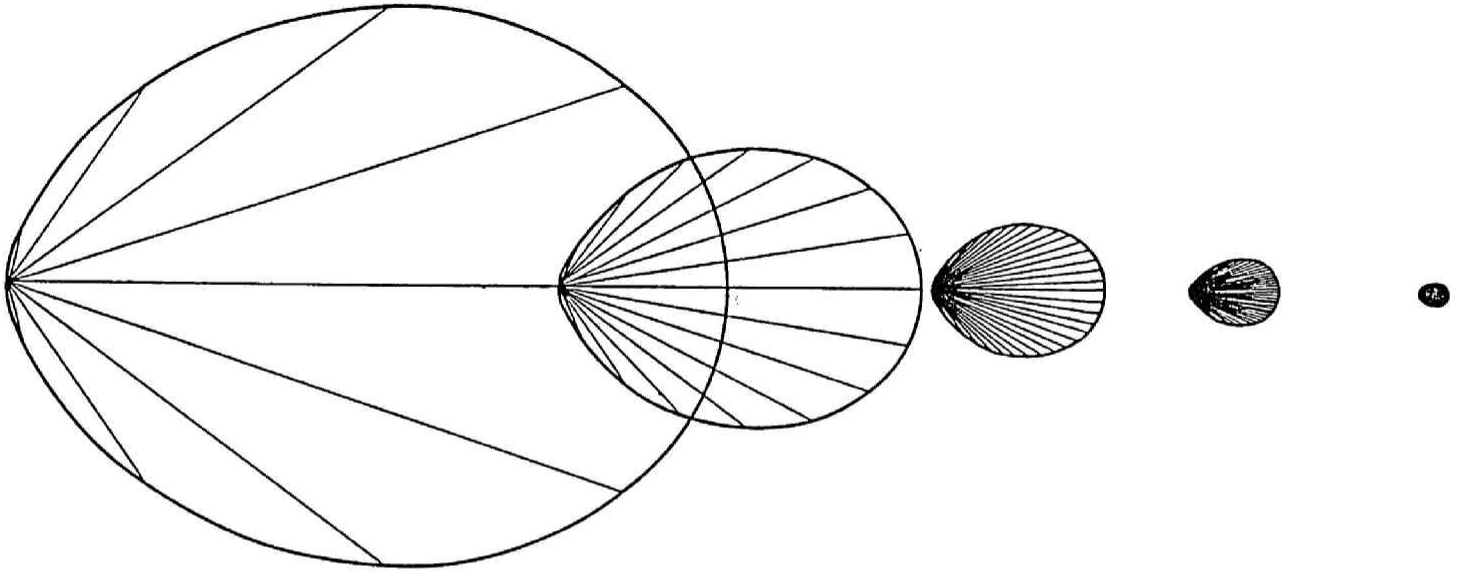

Fig.4.2 The process of the plasma column construction. A heavy ion proceeds in silicon losing its energy. The region explained in Fig.4.1 becomes smaller as the energy of the heavy ion gets smaller. The number of the lines in each region is approximately proportional to the cross section of recoiling primary electrons. The plasma column is obtained by continuously superimposing the regions.

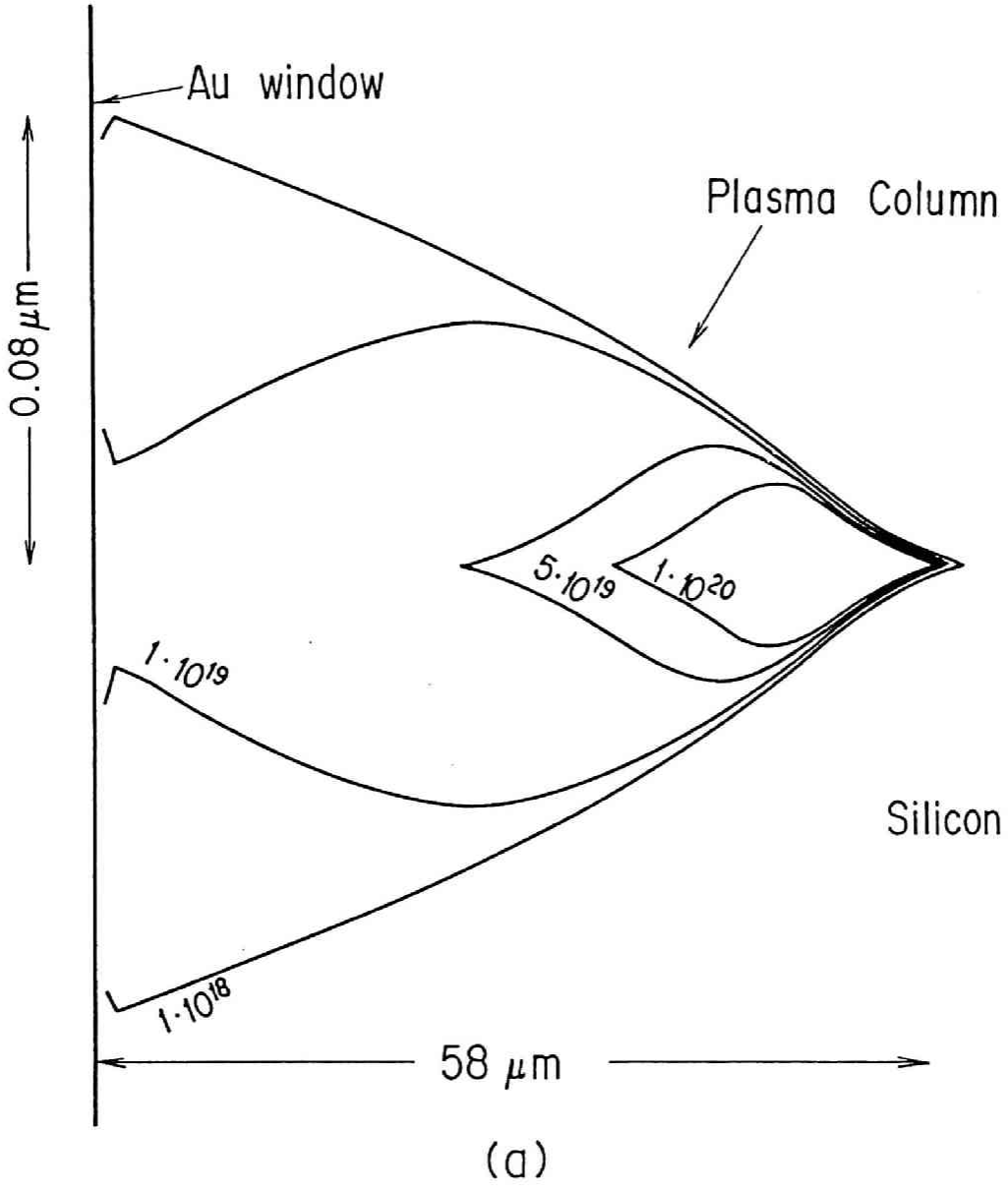

Fig.4.3 Examples of the plasma column formed by (a) alpha particles with 8.78MeV The numbers on the contour lines show the density of electron-hole pairs (n/cm^3).

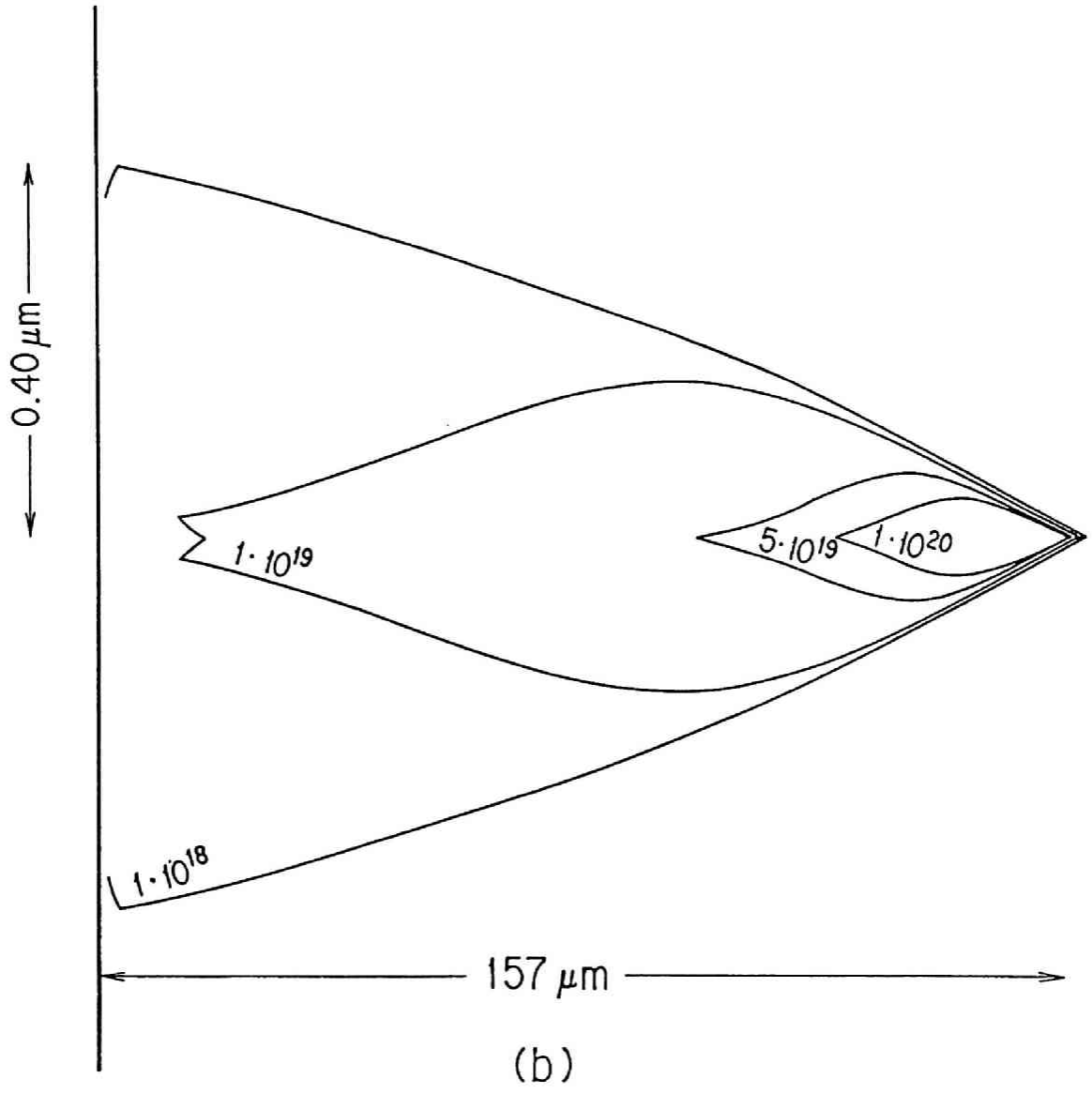

Fig.4.3 (continued) (b) ^{40}Ar with 476MeV

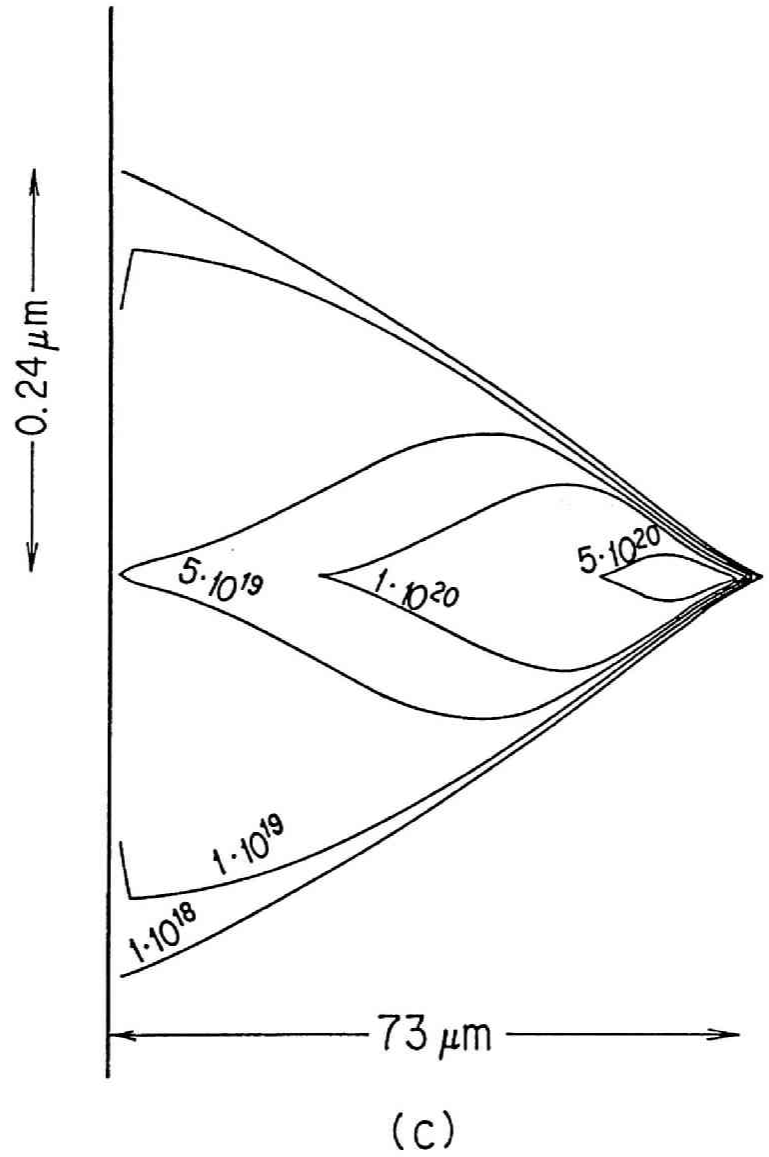

Fig.4.3 (continued) (c) ^{40}Ar with 268MeV.

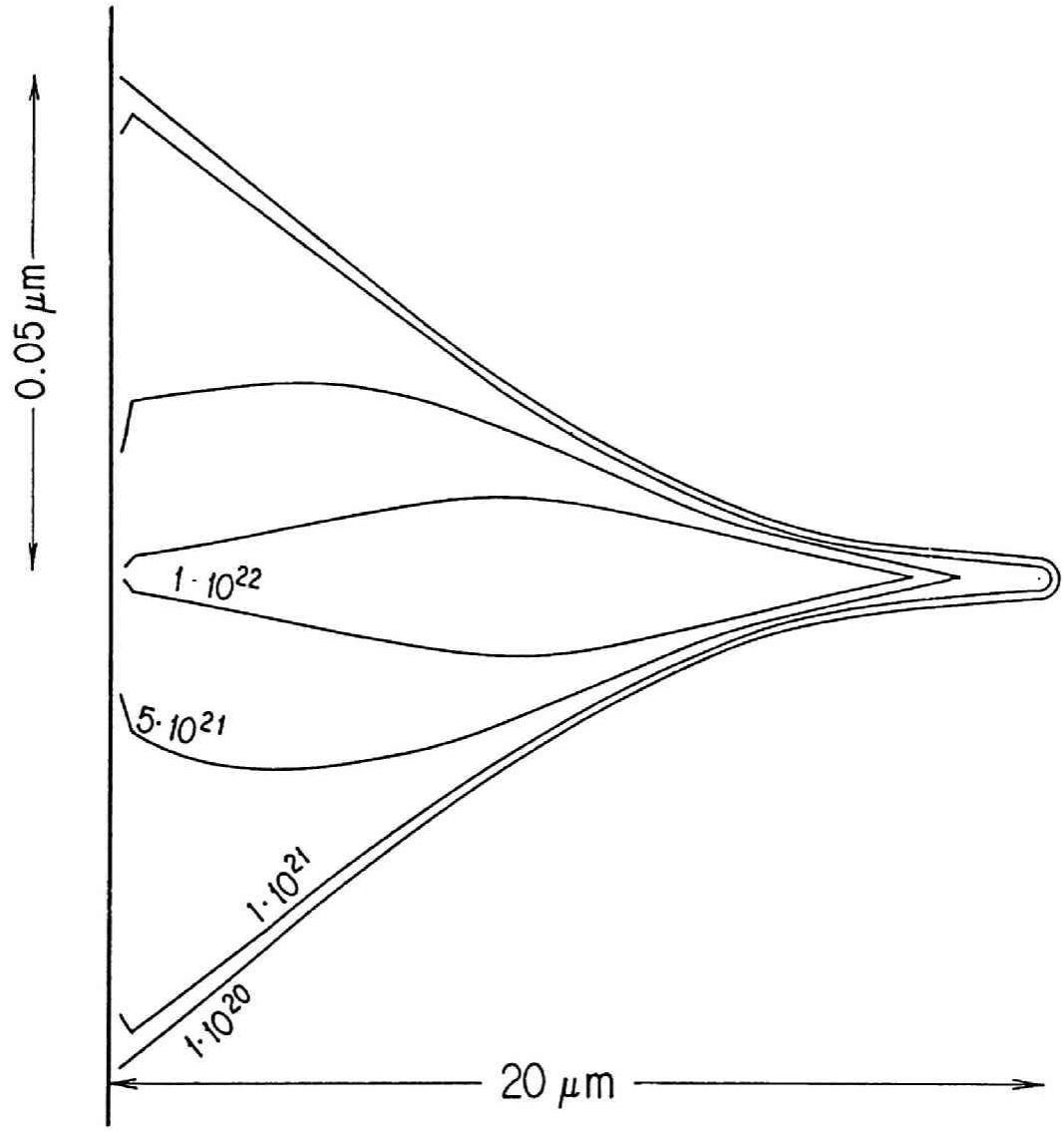

Fig.4.3 (continued) (d) ^{129}Xe with 166MeV.

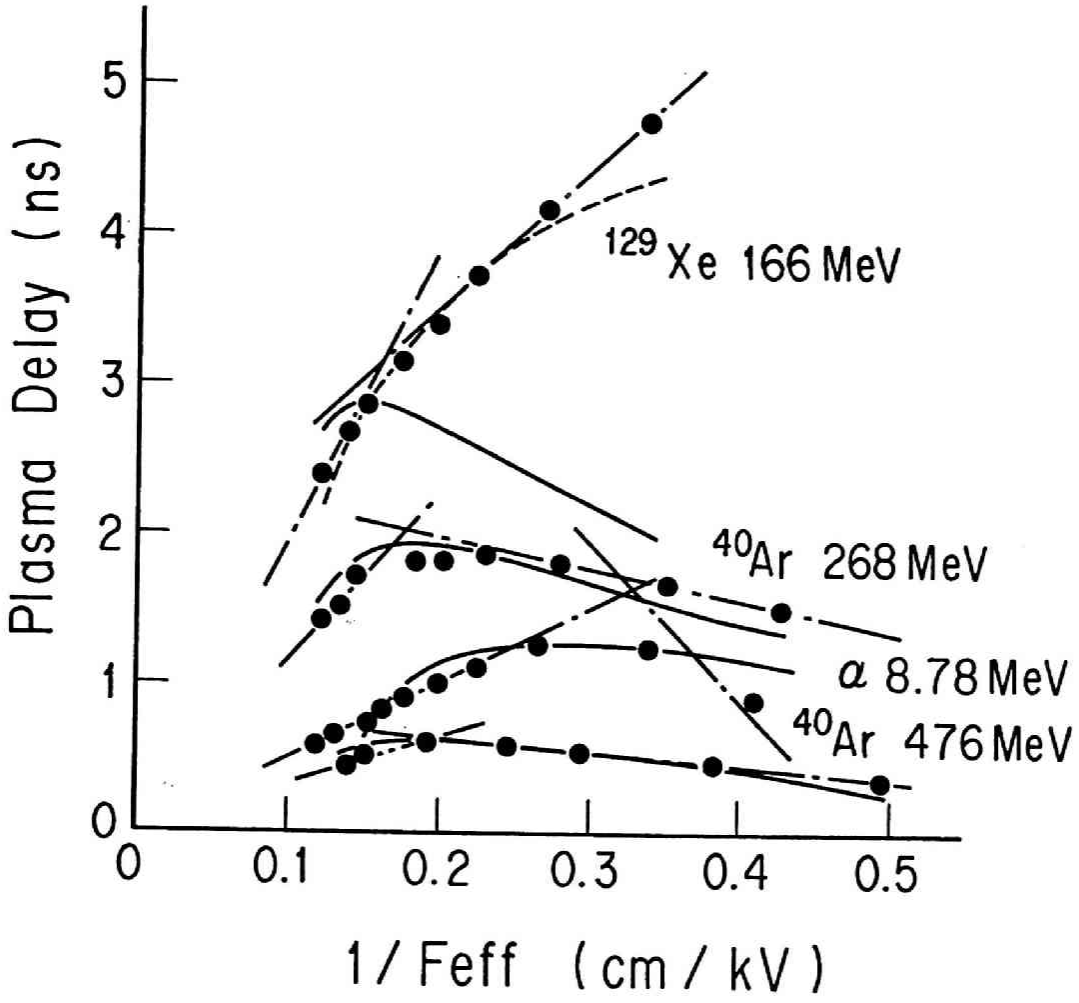

Fig.4.4 The plasma delay of 8.78MeV alpha particles, 268MeV and 476MeV ^{40}Ar and 166MeV ^{129}Xe ions. The black dots are the experimental data of Bohne, *et al.*[23] and the dot-dash lines are the calculations by their empirical formula. Solid lines are the results obtained by the present work with $1/F_e^2$ dependence of the ambipolar diffusion constant. The dashed line is the result for ^{129}Xe with $1/F_e$ dependence of the ambipolar diffusion constant.

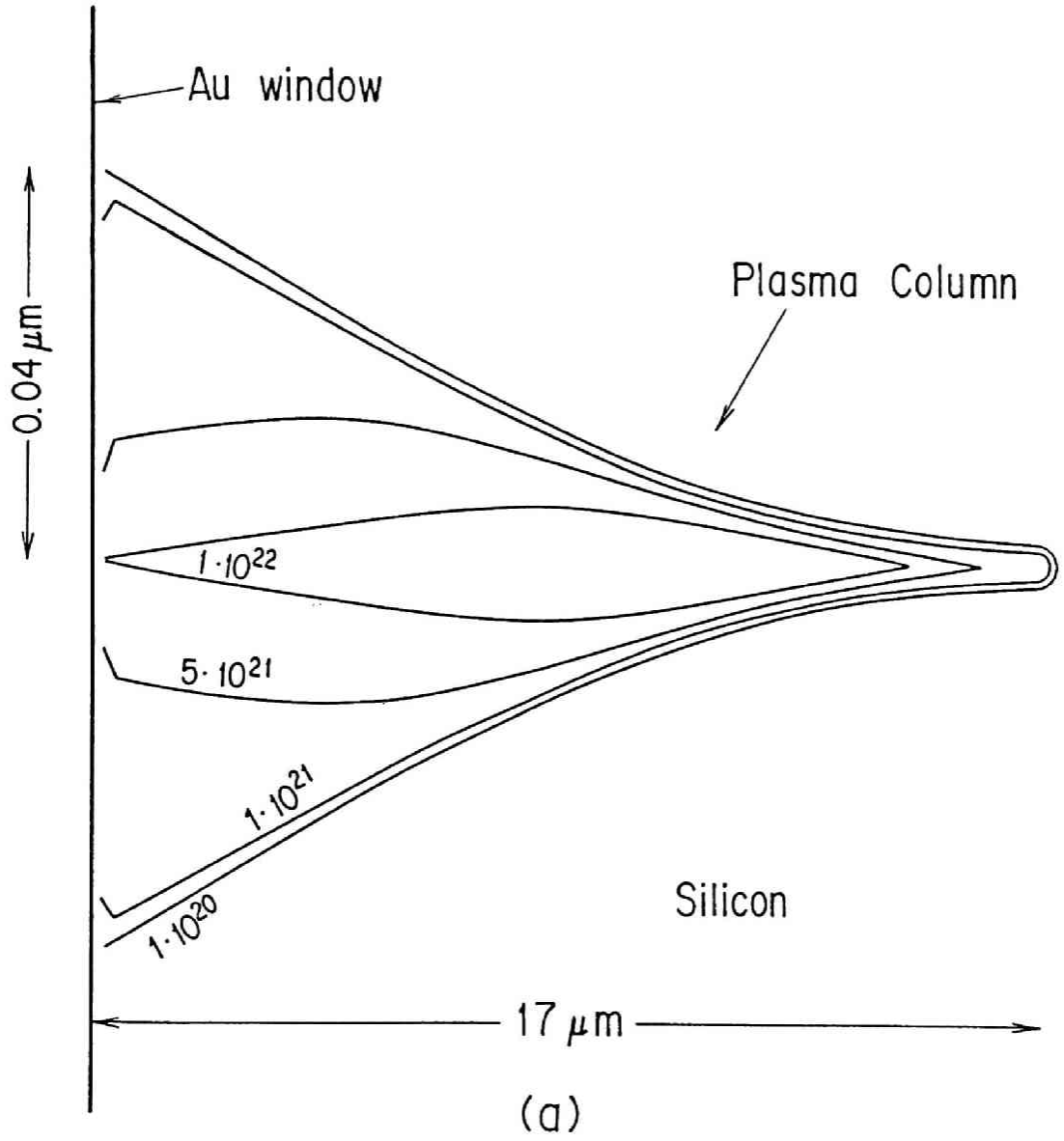

Fig.4.5 Examples of the plasma column formed by the fragments of ^{235}U (n,f) with (a) mass 90, energy 94MeV. The numbers on the contour lines show the density of the electron-hole pairs.

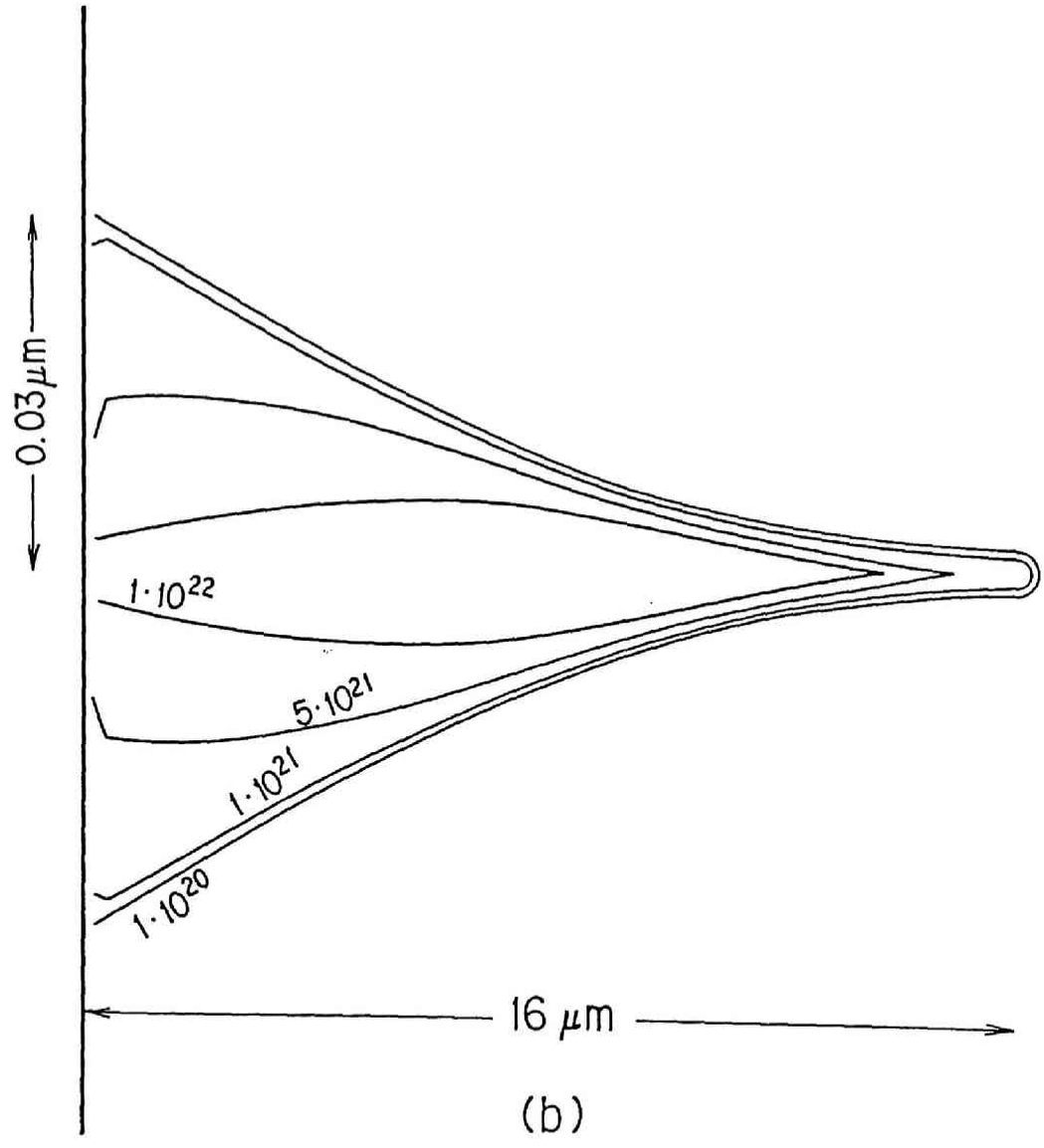

Fig.4.5 (continued) (b) the same as (a), but with mass 101, energy 94MeV.

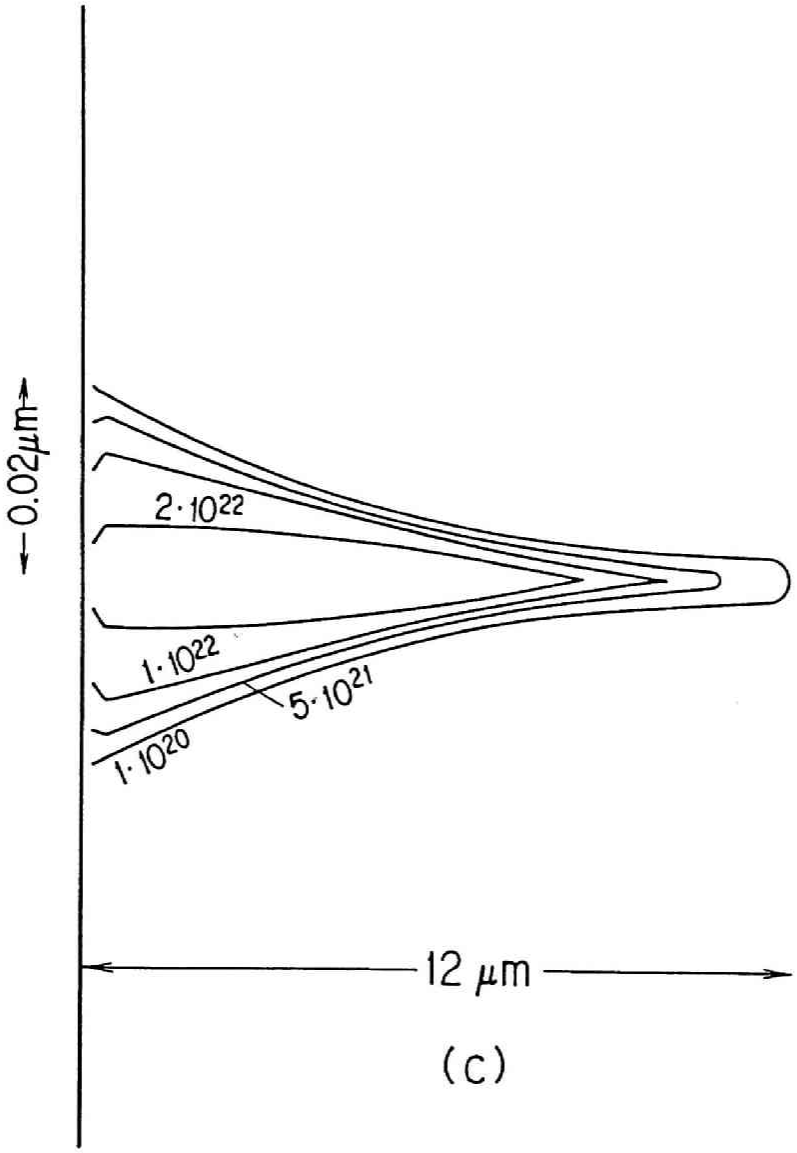

Fig.4.5 (continued) (c) the same as (a), but with mass 135, energy 65 7MeV.

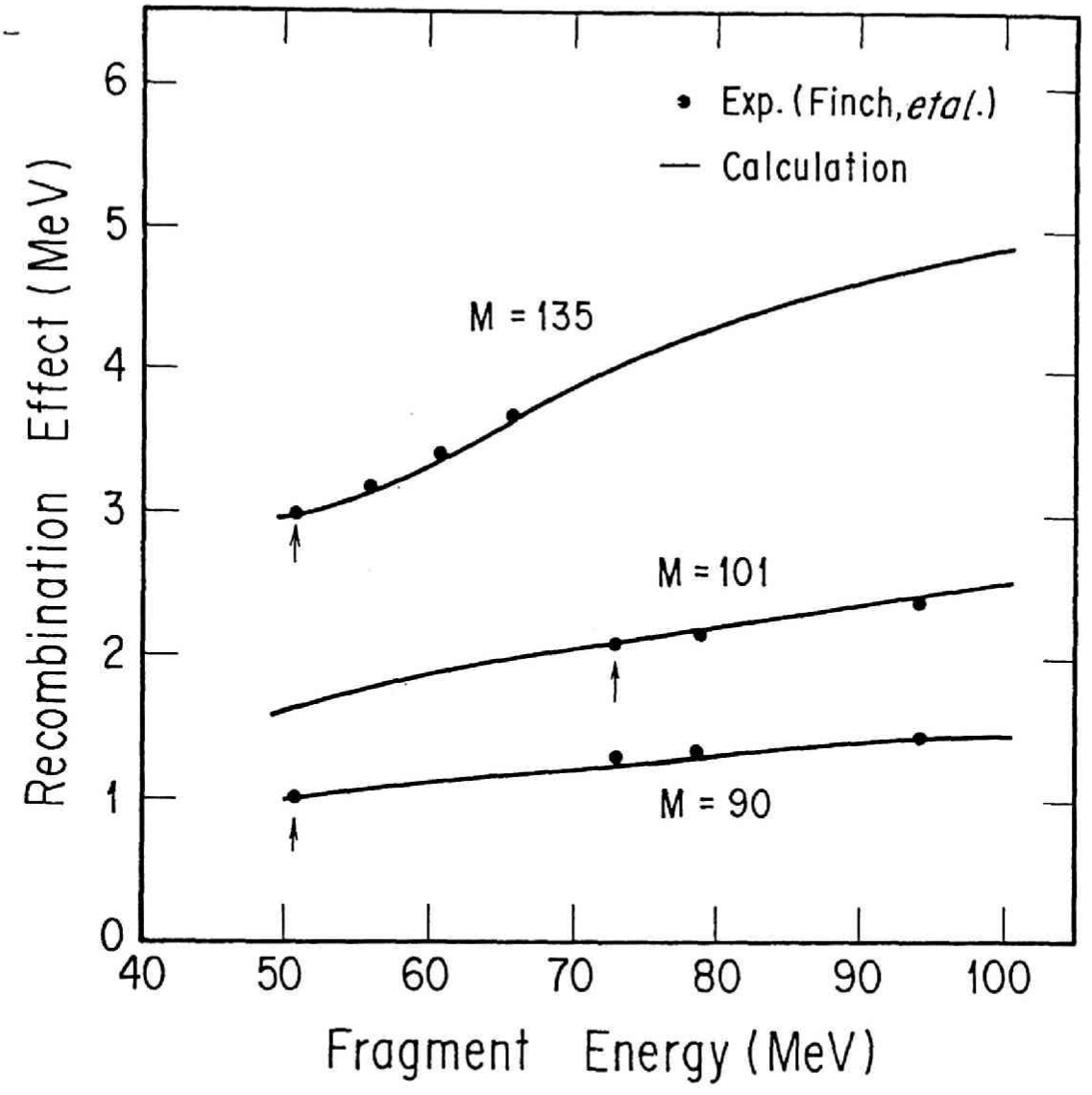

Fig.4.6 Calculated and experimental results of the recombination effect for $^{235}U(n,f)$ fission fragments of mass numbers 90, 101 and 135. The calculated results are normalized to the experimental values of Finch, *et al.*[11] at the points indicated by arrows.

5 Double-energy double-velocity measurement of ^{233}U thermal neutron induced fission fragments[1)]

5.1 Introduction

For the study of the mechanism of nuclear fission and the calculation of the kinetic energy released in the fission phenomena, the shape of the fission barrier, especially the barrier shape close to the scission point, must be known. Another problem exists concerning the scission point; whether thermal equilibrium is achieved. For the study of these themes the velocities, energies and the number of emitted neutrons of two complementary fragments are required.

Using the DEDV measurement system described in Chapter 2, the energies and velocities of the fragments of thermal neutron induced fission of ^{233}U were measured and the number of prompt neutrons emitted from the fission fragment, $\nu_p(m^*)$, was derived and compared with other experimental data. Some discussion will be presented concerned with the thermal equilibrium at the scission point

5.2 Principle of the $\nu_p(m^*)$ derivation

Prompt neutrons are considered to be emitted within 10^{-14}s after fission and the velocities and energies we can measure are those of post-neutron emission fragments With the four parameters (two energies and two velocities), we derive the pre-neutron emission and post-neutron emission fragment masses.

In the fission phenomena, the mass and linear momentum are conserved:

$$m_1^* + m_2^* = m_0 \ , \qquad (5-1)$$

$$m_1^* v_1^* = m_2^* v_2^* \ . \qquad (5-2)$$

Here, the asterisk means the quantities of pre-neutron emission, m_0 is the mass number of the fissioning nucleus,

m_i^* and v_i^* are the mass and velocity of the fragments (i=1,2). From Eqs.(5-1) and (5-2), the pre-neutron emission mass is obtained as,

$$m_i^* = \frac{v_j^*}{v_i^* + v_j^*} \cdot m_0 \quad (i = 1, 2. \ j = 3 - i) . \tag{5-3}$$

The velocities measured by the experiment are the post-neutron emission velocities. However, the neutrons are emitted as if they evaporate from the fragments and do not disturb the fragment velocities[2],

$$v_i^* = v_i . \tag{5-4}$$

The relation between the velocity and kinetic energy is given

$$E = \frac{k}{2} m v^2 , \tag{5-5}$$

where k is the conversion constant 1.0365 from MKS unit to cm, amu, ns and MeV in energy. The kinetic energy measured by SSBs is given by Eq.(2-1). With Eqs.(2-1) and (5-5), the post-neutron emission mass is obtained:

$$m = \frac{ax + b}{k/2 \cdot v^2 - a'x - b'} . \tag{5-6}$$

The number of emitted neutrons are obtained from Eqs.(5-3) and (5-6);

$$\nu_p(m^*) = m^* - m . \tag{5-7}$$

5.3 Experimental procedure

5.3.1 Arrangement

The picture of the experimental chamber and the experimental arrangement is shown in Figs.5.1 and 5.2 The experiment was performed at the super mirror neutron guide tube facility of Kyoto University Reactor (KUR) The neutrons were guided by the super mirrors developed by Akiyoshi, *et al* [3]. The super mirrors were multi-layer films of Ni and Ti deposited onto float glass plates. The guide tube was composed of 13 elements and its total length was 11.7m. A remote

controlled beam shutter was set at the neutron exit so that the experimentalist could check and adjust the experimental conditions while the reactor was on. The neutron beam was collimated to 2cm×7cm by a beam slit made of ^{6}LiF. The neutron flux was about $5\times10^{7}n/cm^{2}s$ and there was little gamma ray background from the reactor core (0.4mR/hr). The neutrons entered an evacuated chamber through a thin aluminum window (1mm thick) and went out through a similar window on the opposite side Less than 1% of the neutrons were lost by this experimental set up and the rest of the neutrons were utilized for other experiments whose devices were set behind this experimental set up. The room temperature was kept at 23°C through the experiment to avoid a gain shift of the detectors.

5.3.2 Uranium target

The uranium-233 target used in this experiment was prepared by the lacquer method[4] at KURRI. Dibenzoilmethane (DBM:$C_6H_5COCH_2COC_6H_5$) was dissolved in acetone. The solution was mixed with a nitrouranil solution while stirring. The precipitation of uranildibenzoilmethane was separated from the solution and dissolved to ethylacetate. Upon adding a little nitrocellulose, this solution had low viscosity. Dropping this solution on the surface of distilled water, a thin film was developed. By picking up the thin uranium film with holder, the ^{233}U target was made. A drawing of the uranium target is shown in Fig.5.3.

The thickness of the ^{233}U target was determined to be $7\mu gU/cm^{2}$ by measuring the energy loss of alpha particles emitted by ^{252}Cf. The purity of the ^{233}U was 99.47%. The contents of the target is shown in Table 5.1.

5.3.3 Corrections

In the actual measurement, the fragments lose energy both in the uranium target and in the thin plastic scintillator

film. With respect to flight time, plasma delay prolongs the flight time for some nanoseconds.

In this chapter, the correction methods for the energy loss in the films and the plasma delay are described.

(1) Energy loss in films

When the fission fragments pass through materials, the fragments interact electrically with the electrons in the materials and lose energy. The energy loss of a charged particle is well known and the energy loss of the fragment was calculated by Bethe's formula for each fragment in the analysis. The thickness of the uranium target through which the fission fragment passes was assumed to be half of the whole thickness.

(2) Plasma delay

The plasma column formed in the SSB retards the pulse output, as was described in Chapter 4.5. This plasma delay should be calculated by Eq (4-24). However, its absolute value cannot be determined at this stage because of the lack of experimental data. Former researchers fit the time delay using a polynomial function of mass and energy[5),6)];

$$t_d = t_d(m, E) \quad . \tag{5-8}$$

The author followed the method proposed by Mueller, *et al.*[6)]. They fit the time delay by a second order polynomial, so that the calculated velocity satisfies the following equations,

$$E_i^* = E_i \cdot \frac{m_i^*}{m_i} \quad , \tag{5-9}$$

$$m_i = m_i^* - \bar{\nu}(m_i^*) \quad . \tag{5-10}$$

In this calculation, the averaged neutron emission number $\bar{\nu}(m_i^*)$ was taken from the work of Apalin, *et al.*[7)].

5.4 Result and discussion

An energy pulse height spectrum of the single fission fragment of the thermal neutron induced fission of ^{233}U is shown in Fig.5.4. The peaks in the higher channels correspond

to light fragments and the lower channels correspond to heavy fragments. The sharp peak in about the 30th channel is the alpha particle peak. In Fig.5.5, the TOF spectrum is shown. The peak in the lower channels corresponds to the light fragment and the higher channel's broad peak to the heavy fragment. The peaks of heavy and light fragments are clearly separated. Alpha particles were not counted because they produced very little luminescence in the TFD as a start pulse for the TOF.

The pre-neutron emission fission fragment mass distribution is shown in Fig.5.6. The mass distribution is compared to that of Milton and Fraser[8]. The kinetic energy distribution is shown in Fig.5.7. The error bars in the mass distribution indicate the statistical errors. The error bars in other figures indicate one standard deviation. As experimental error sources, we considered the flight path (error 0.1%), the thickness of ^{233}U target and scintillator film (about 10%), the resolution of TOF measurement system (133ps) and the energy resolution of the SSB (about 78keV). The mean values of fragment masses, kinetic energies and velocities of the light and heavy fragments are shown in Table 5.2. For comparison, the mean values reported by other authors are also listed[5),9)-11)]. The data of Ref.(9)-(11) are for thermal neutron induced fission of ^{233}U. The results of Patin, *et al* [5] are listed, since the data was taken by the double-energy double-velocity method. The present results agree well with other works. The prompt neutron distribution, $\nu_p(m^*)$, is shown in Fig.5.8. The data of Apalin, *et al*.[7] and of Milton and Fraser[8] are plotted for comparison. The present results are close to those of Milton and Fraser in the heavy fragment region, while in the mass region of 100 to 110, the results are close to those of Apalin, *et al*. In the light fragment region, $\nu_p(m^*)$ is greater than the other works. This behavior is also seen in the preliminary result of the analysis for DEDV measurements of thermal neutron induced fission of ^{235}U The averaged total neutron emission number, ν_T, of this mea-

surement was 2.53 and agreed well with the JENDL-2[12] value of 2.49, within the error. The mean values of the number of prompt neutrons of light and heavy fragments are also shown in Table 5.2.

– The number of emitted neutrons are greater than found in other authors' works in the mass range of 80–100. The energy balance is considered in the following for the representative mass separation of 85 and 149. The most probable candidates for fragments of masses 85 and 149 are ^{85}Nb and ^{149}Pr, respectively. From the mass excesses of ^{85}Nb, ^{149}Pr, ^{233}U and neutrons, the released energy is calculated to be 179.9MeV[13]. With the total kinetic energy equal to 164.2MeV, the excitation energy of the two fragments is deduced to be 15.7MeV. If thermal equilibrium is achieved between the two fragments, energies of 5.7MeV and 10.0MeV are distributed to ^{85}Nb and ^{149}Pr, respectively. On the other hand, with respect to the mass excess calculation, energies of 5.43MeV and 10.5MeV are needed for ^{85}Nb and ^{149}Pr to emit 2 and 1.7 neutrons With the consideration described above, thermal equilibrium is achieved between fragments, at least macroscopically. In the future, this sort of study will be carried out for each fission event.

5.5 Conclusion

The double-energy double-velocity measurement system using thin film detectors as start detectors was performed for the thermal neutron induced fission of ^{233}U. The obtained data agreed well with other works. The averaged quantities of pre-neutron emission fragment are shown in Table 5.2. The average number of total neutrons emitted was 2.53 and agreed well with the value of JENDL-2, within the error. The data on the pre-neutron emission mass, kinetic energy and number of prompt neutrons of the fission fragments was stored on a magnetic disk event by event in a list mode. Utilizing this data set, the fission phenomena, especially the inertial

excitation energy of the fission fragment at scission point and the shape of the scission configuration will be studied. One shortcoming in this measurement system is that the fragment passes through the thin plastic scintillator film of 20$\mu g/cm^2$ thickness and lose from 1 to 2MeV of kinetic energy. With some improvement, e.g., the development of a light guide with less photon attenuation and the usage of more efficient photomultipliers, the thickness of the scintillator film will be able to be reduced.

References

1) Kanno, I., Nakagome, Y. and Kimura, I.: J. Nucl. Sci. Technol., to be published.
2) Schmitt, H. W., Lide, R. W. and Pleasonton, F.: Nucl. Instr. and Meth., **63**, 237 (1968).
3) Akiyoshi, T., Ebisawa, T., Kawai, T., Yoshida, F., Ono, M., Mitani, S., Kobayashi, T. and Okamoto, S.: "Proceedings of the 1985 Seminar on Nuclear Data", JAERI-M 86-080, p.380 (1986).
4) Parker, W., de Croes, M. and Sevier, Jr., F.: Nucl. Instr. and Meth., **7**, 22 (1960).
5) Patin, Y., Cierjacks, S., Lackar, J., Sigaud, J , Haouat, G. and Cocu, F.: Nucl. Instr. and Meth., **160**, 471 (1979).
6) Muller, R., Naqvi, A. A., Kaeppeler, F. and Dickmann, F.: Phys Rev., **C29**, 885 (1984).
7) Apalin, V. F., Gritsyuk, Yu. N., Kutikov, I. E., Levedev, V I. and Mikaelian, L. A.: Nucl. Phys., **71**, 553 (1965).
8) Milton, J. C. D. and Fraser, J. S.: "Proceedings of the Symposium on Physics and Chemistry of Fission", Salzburg, IAEA, Vienna, Vol.I, p.39 (1965).
9) Milton, J. C. D. and Fraser, J. S.: Can. J. Phys., **40**, 1626 (1960).
10) Pleasonton, F.: Phys. Rev., **174**, 1500 (1968).
11) Bennett, M. J. and Stein, W.: Phys. Rev., **156**, 1277 (1967).
12) Nakagawa, T.: "Summary of JENDL-2 General Purpose File", JAERI-M 84-103 (1984).
13) Lederer, C. M. and Shirley, V. S.: "Table of Isotopes", John Wiley & Sons, Inc., New York, (1978).

Table 5.1 Content of the target.

^{233}U	Content (%)
U-232	0.8 ppm
U-233	99.47
U-234	0.166
U-235	0.064
U-236	0.015
U-238	0.282

Table 5.2 Mean values and standard deviations of pre-neutron emission distributions. The results of Ref.(9)--(11) are the data on thermal neutron induced fission of ^{233}U. The result of Ref.(5) is listed in the interest of measuring the data by double-energy double-velocity method, though the data was taken using the (d,pf) reaction of ^{233}U.

Quantities	Present	Milton[9]	Pleasonton[10]	Bennett[11]	Patin[5]
$<m_L^*>$ (amu)	94.36 ± 0.23	94.57 ± 0.1	95.2 ± 1.0	94.8	95.3 ± 0.5
$\sigma(m_L^*)$ (amu)	6.21	5.85	4.98	5.69	5.70
$<E_L^*>$ (MeV)	101.38 ± 0.72	99.9 ± 1.0	101.9 ± 1	101.7 ± 1.5	101.3 ± 1
$\sigma(E_L^*)$ (MeV)	5.95	6.2		5.54	5.59
$<v_L^*>$ (cm/ns)	1.44 ± 0.005				
$\sigma(v_L^*)$ (cm/ns)	0.072				
$<\nu_L^*>$	1.68 ± 0.69				
$<m_H^*>$ (amu)	139.64 ± 0.23	139.43 ± 0.1	138.8 ± 1.0	139.3	138.7 ± 0.5
$\sigma(m_H^*)$ (amu)	6.21	5.85	4.98	5.69	5.70
$<E_H^*>$ (MeV)	68.78 ± 0.34	67.9 ± 0.7	70.1 ± 0.8	69.5 ± 1.5	69.9 ± 1
$\sigma(E_H^*)$ (MeV)	7.48	7.3			7.68
$<v_H^*>$ (cm/ns)	0.975 ± 0.002				
$\sigma(v_H)$ (cm/ns)	0.073				
$<\nu_H>$	0.85 ± 0.72				
$<E_K^*>$(MeV)	170.16 ± 0.80	167.6 ± 1.7	172 ± 1.8	171.2 ± 2	171.52 ± 1
$\sigma(E_K^*)$ (MeV)	10.65	11.2		10.84	11.0
ν_p	2.53 ± 1.00				

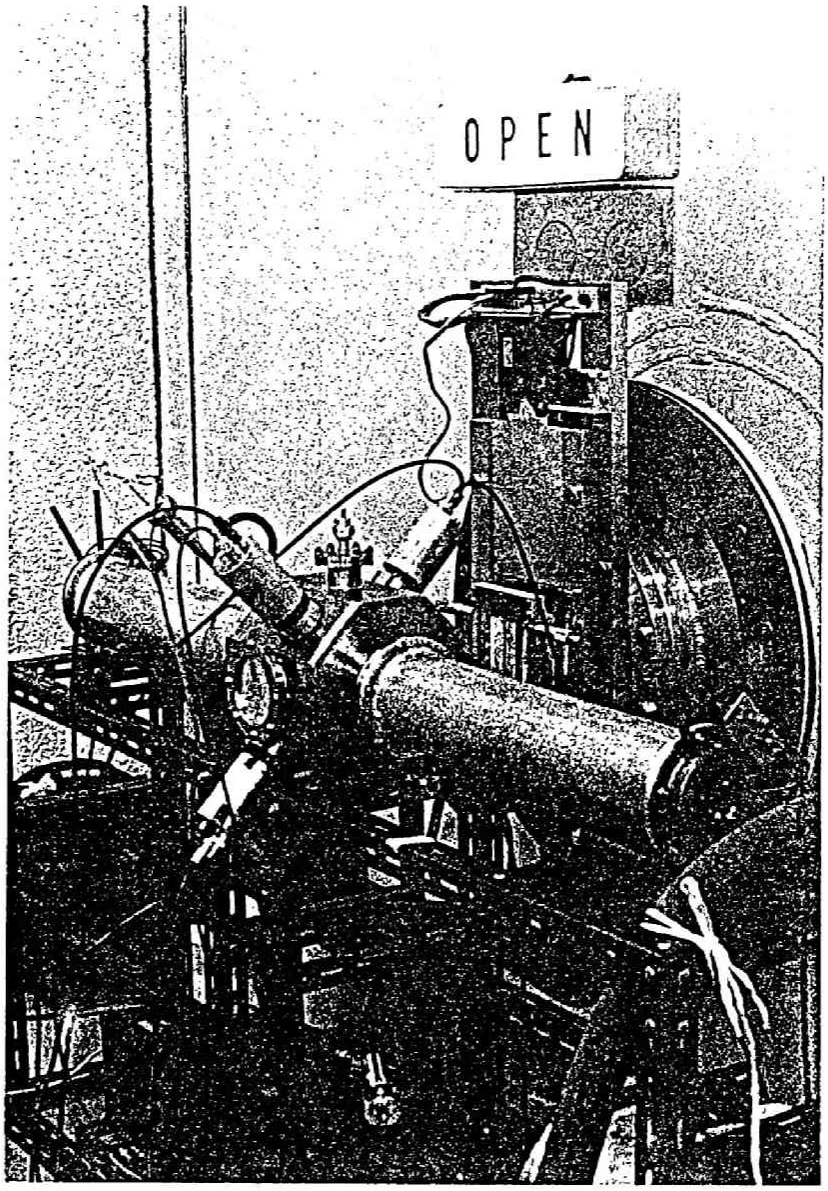

Fig.5.1 The picture of the experimental chamber beside the exit of super mirror neutron guide tube facility of KUR.

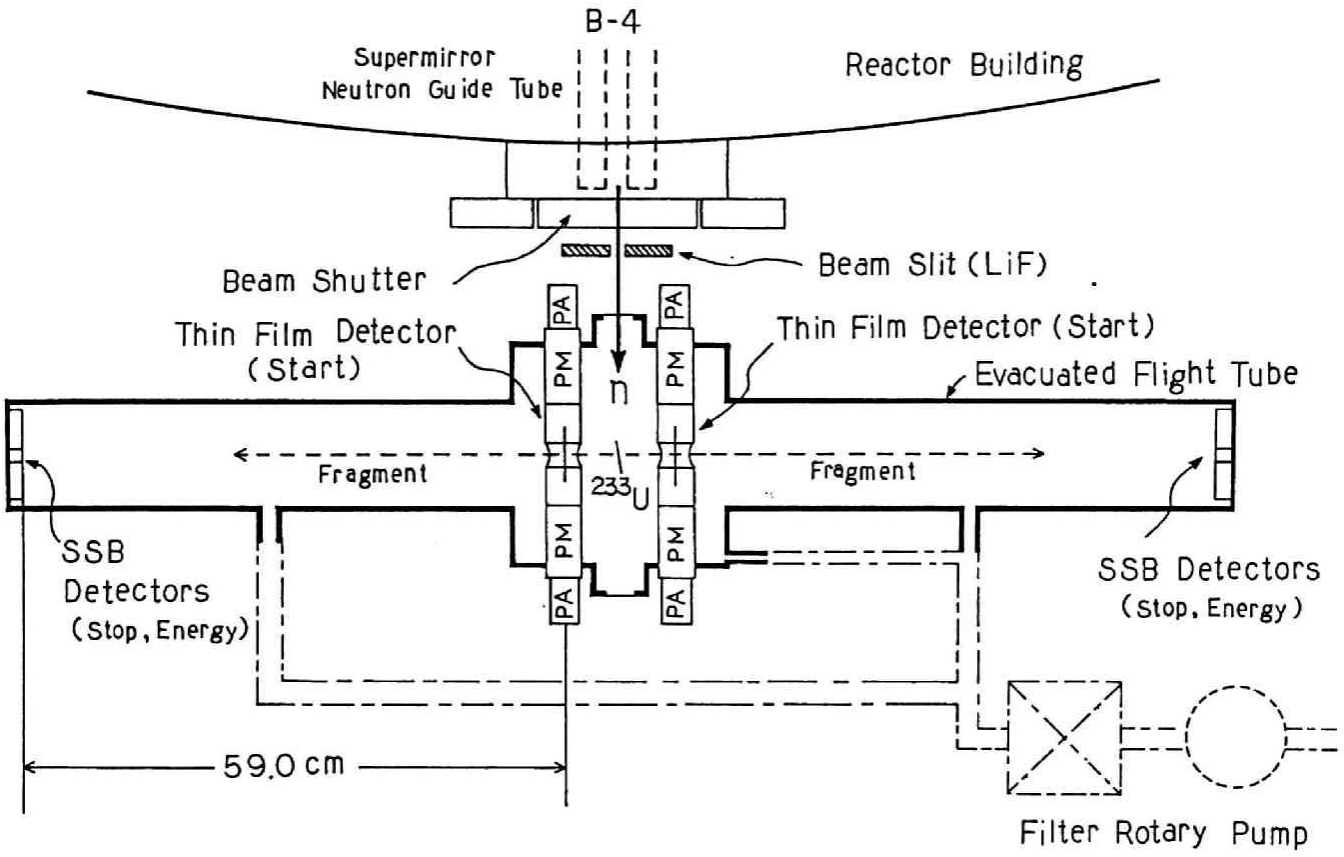

Fig.5.2 The experimental arrangement for double-energy double-velocity measurement. The chamber was set at the exit of the supermirror neutron guide tube of KUR.

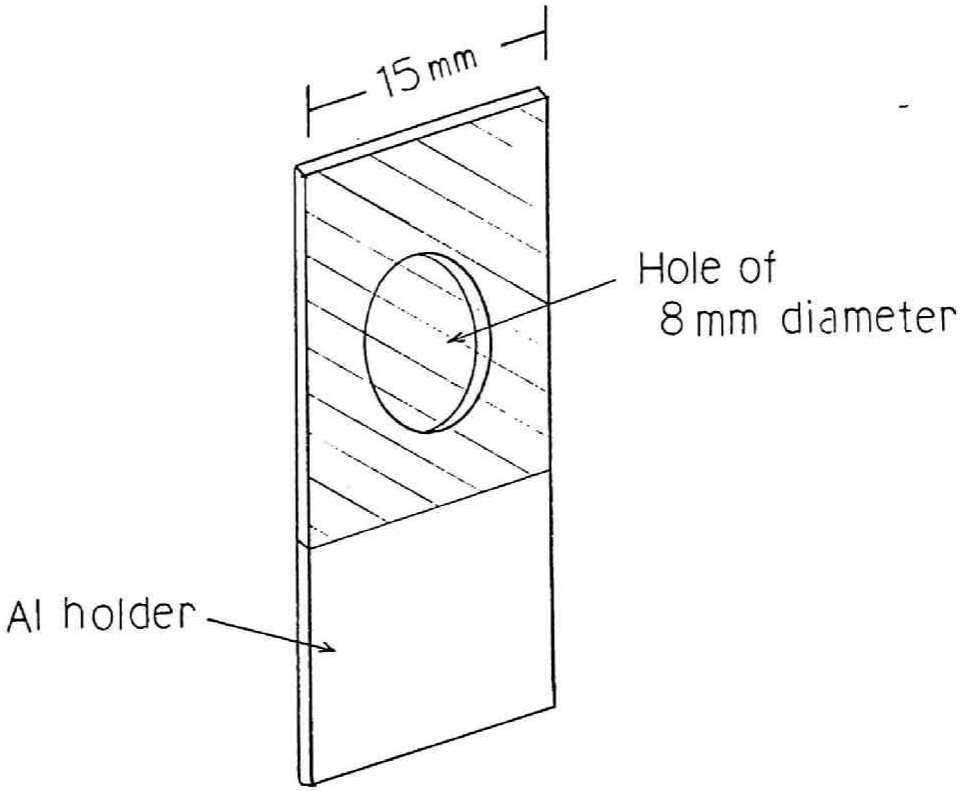

Fig.5.3 The uranium-233 target. The uranium-233 is contained in a film indicated by a hatched area and the film is supported in an aluminum holder.

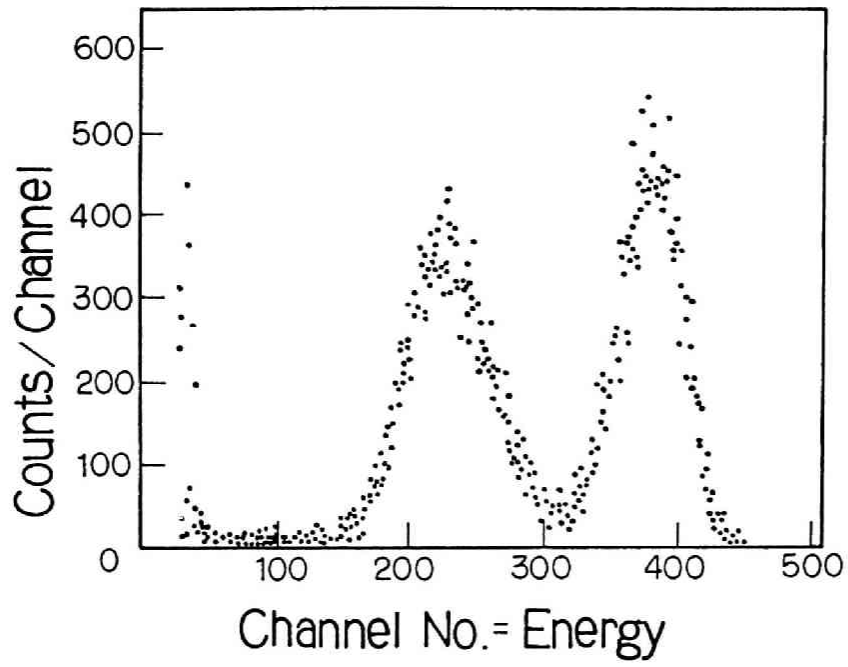

Fig.5.4 Pulse height spectrum of ^{233}U thermal neutron induced fission fragments.

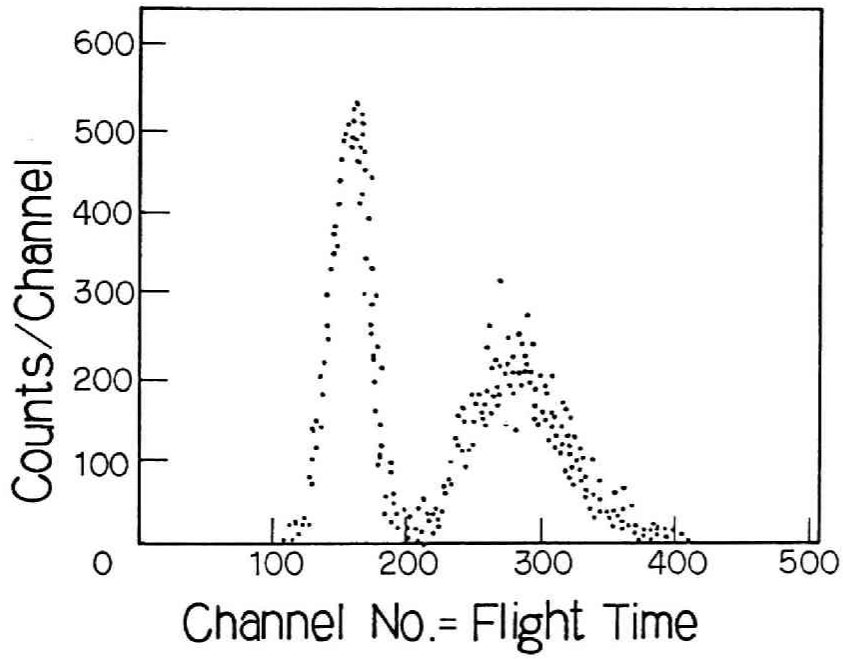

Fig.5.5 Time-of-flight spectrum of ^{233}U thermal neutron induced fission fragments.

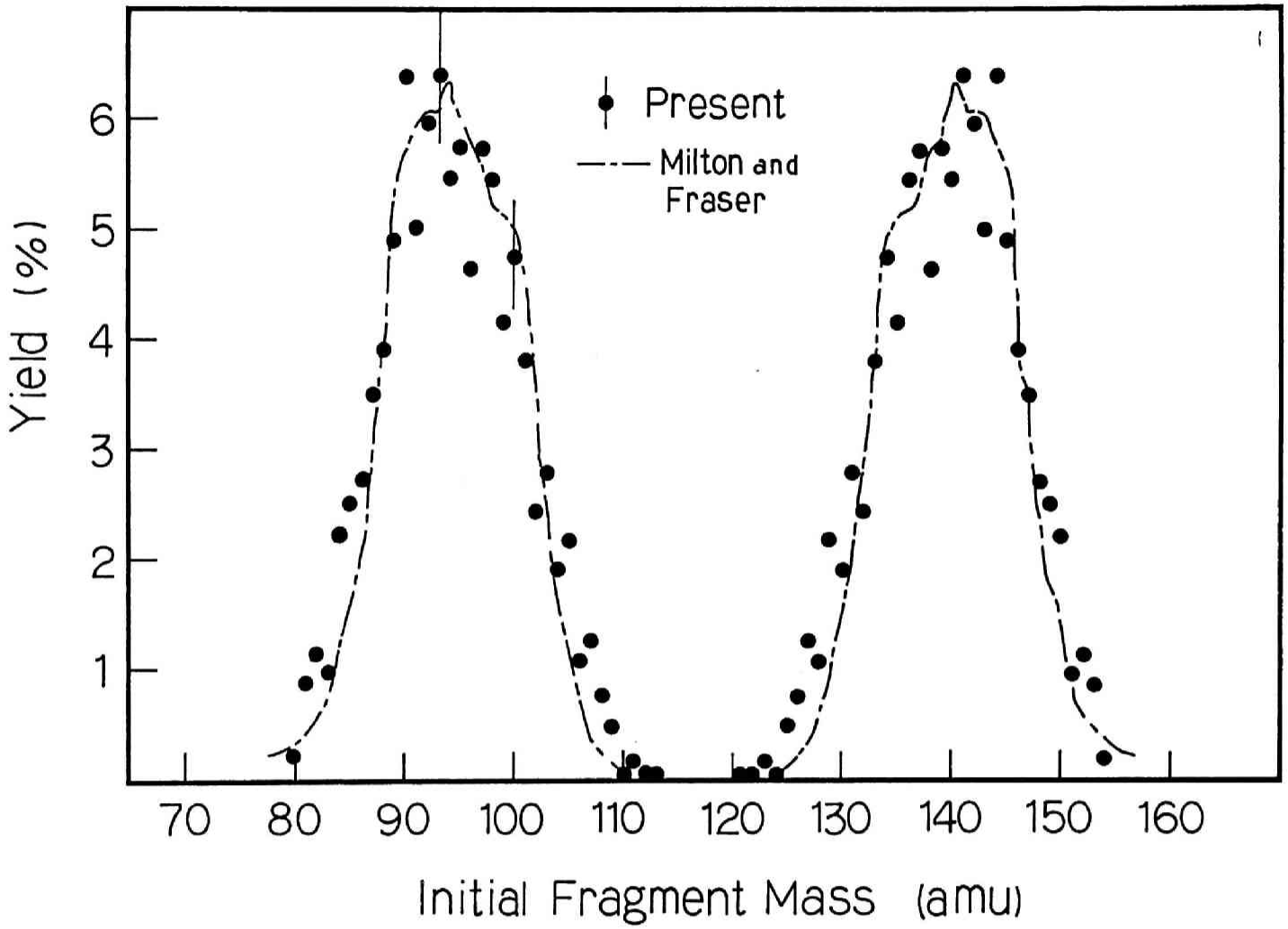

Fig.5.6 Mass distribution of ^{233}U thermal neutron induced fission fragments. For a comparison, the data of Milton and Fraser is also plotted.

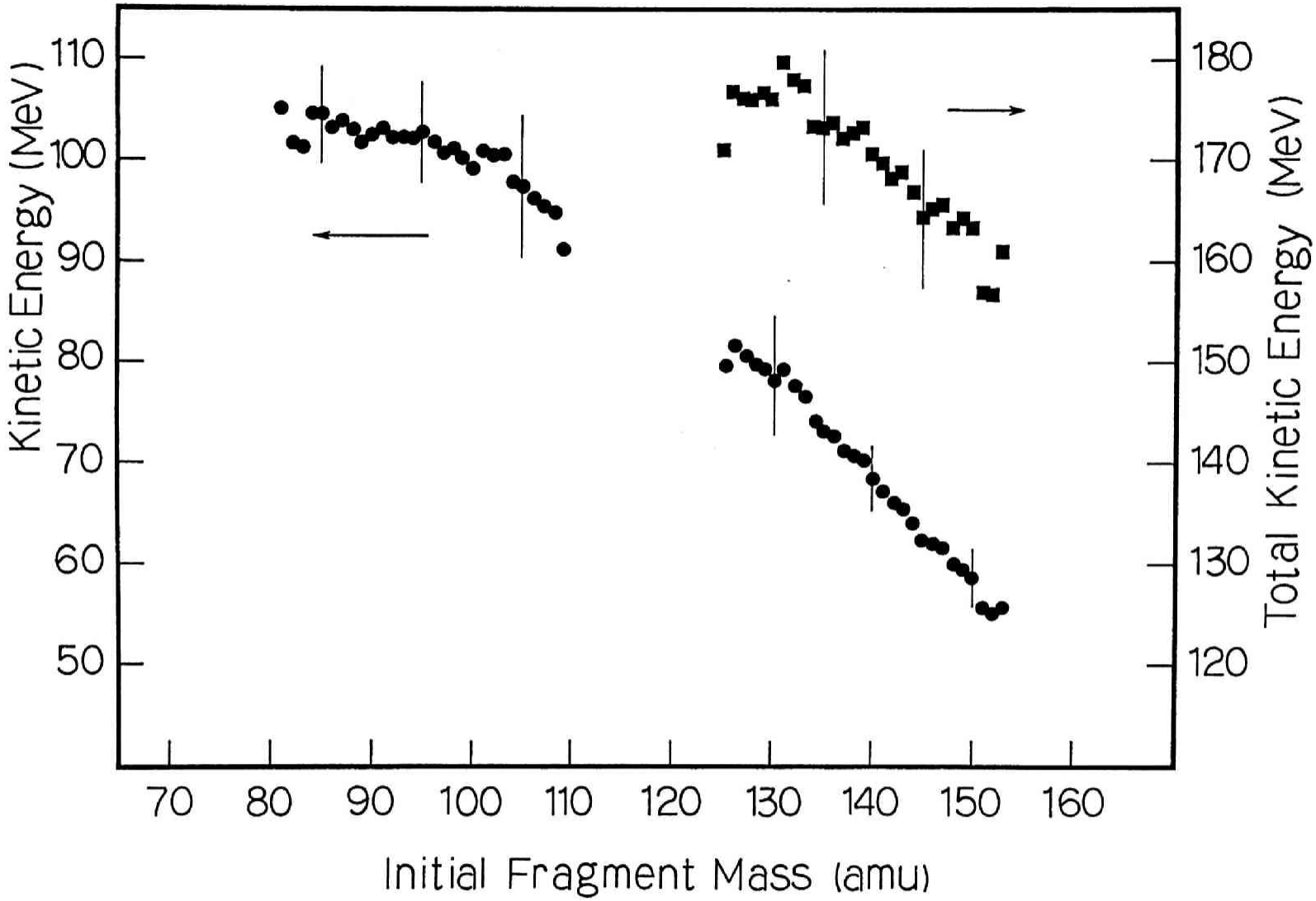

Fig.5.7 Kinetic energy distribution of ^{233}U thermal neutron induced fission fragments.

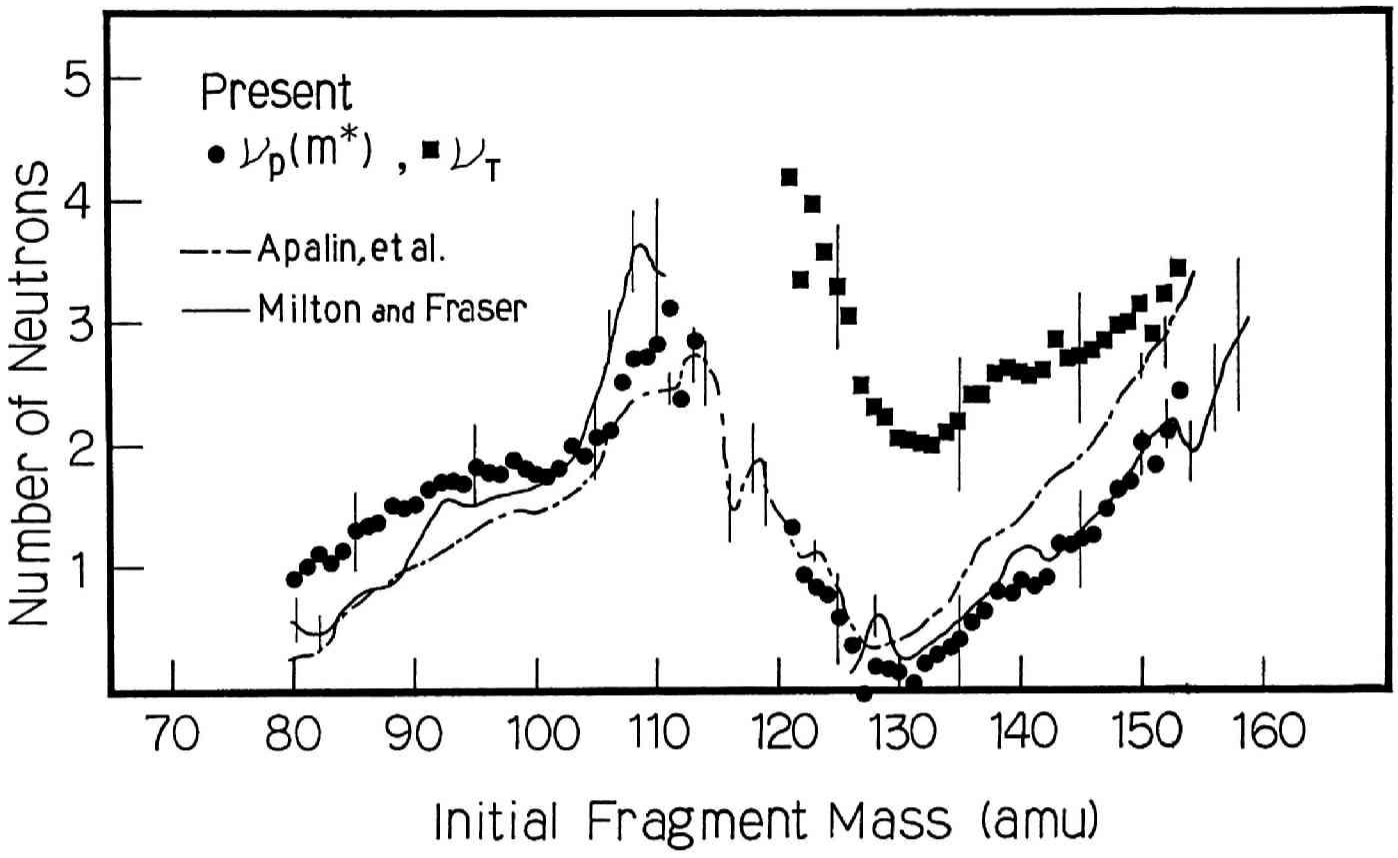

Fig.5.8 Prompt neutron distribution, $\nu_p(m^*)$, of ^{233}U thermal neutron induced fission fragments. The results of Apalin, *et al.* and Milton and Fraser are plotted for comparison.

6. Concluding remarks

In the present study, the double-energy double-velocity measurement system, using thin film detectors (TFDs) as detectors for the start signal of time-of-flight (TOF) and silicon surface barrier detectors (SSBs) for energy and stop signal of TOF, was established. This system is applicable to any fission event, such as spontaneous fission, thermal neutron induced fission, fast neutron induced fission and charged particle induced fission, because it takes start pulses directly from the fission fragments using the TFD.

The characteristics of the detectors were studied theoretically and experimentally. Concerning the TFD, a new model of luminescence production was proposed, which took into account the thickness of the scintillator film[1]. The dependence of the pulse height spectrum of the spontaneous fission fragment on the thickness of the scintillator film was studied experimentally and the results were analyzed using the model of luminescence production[2]. The SSB has two demerits mainly when it is used for heavy ion detection: pulse height defect and plasma delay. To correct for the pulse height defect, a relation was proposed by Schmitt, *et al.*[3]. In order to make certain of the validity of this relation, the author modeled plasma column formation and plasma column erosion. With these models, which closely relate to the plasma delay and the recombination effect, they were calculated quantitatively for the first time[4].

After these studies, the double-energy double-velocity measurement was carried out for the thermal neutron induced fission of ^{233}U, for which data is scarce. As the result of this measurement, the averaged mass numbers, kinetic energies, velocities and number of prompt neutrons of the light and heavy fission fragments were derived[5].

In this chapter, the author points out the works which should be performed in the future.

First of all, the author would like to discuss the

double-energy double-velocity measurement system. The time resolution and the energy resolution of the present system are slightly inferior to the measurement system of Mueller, *et al.*[6], though their system cannot be used for either spontaneous or thermal neutron induced fission. However, both systems have the same problem in the time-of-flight measurement: plasma delay. Even if the plasma delay is studied in detail, the time delay of the output pulse exists as long as the measurement system employs an SSB for stop signal detection. In the future, other stop signal detector should be used. There are two candidates for such a detector; TFD and the channel plate detector (CPD) proposed by Girard, *et al.*[7], which makes use of electrons emitted when a heavy ion impinges upon an SSB. Although the characteristics of the TFD are well reported in by the studies by the present author and other researchers, the heavy ion loses some energy in the scintillator film of the TFD. On the other hand, the time resolution of the CPD proposed by Girard, *et al* is around 150ps and makes the time resolution of this system worse than a TFD system. With respect to reducing the correction, the author prefers the CPD, which does not disturb the heavy ion. In future double-energy double-velocity measurement system; timing detectors which do not disturb the fission fragments and have good time resolution should be used.

On the thin film detector, there is some work left for the future. One is theoretical work to connect the model of the luminescence production for very thin plastic scintillator film described in this study to Birks' formula[8]. This formula predicts the specific luminescence for light particles such as electrons, protons and alpha particles as a function of the specific energy loss in plastic scintillators of usual dimensions. The author expects some interesting features to be observed at the borders of these two models for luminescence production. As an experimental work, the dependence of the pulse height spectrum on the diameter of the hole of the light guide must be studied. Technically, a light guide

which allows large solid angles and can efficiently collect photons should be developed. Associated with the development of the efficient light guide, a technique of preparing thinner scintillator film (less than $10\mu g/cm^2$) must be developed. With these two technical improvement, the velocity of fission fragments will come to be measured more precisely.

Concerning the plasma delay and the recombination effect, the author proposed models[4] which sometimes needed rather daring assumptions. However, these assumptions were indispensable because of the lack of experimental data needed for theoretical consideration. Data required for considerations of the plasma delay and the recombination effect are data which relate the both two phenomena. After such an experiment, the plasma delay and the recombination effect can be analyzed with less assumptions.

As an application of the double-energy double-velocity measurement system, the measurement for the thermal neutron induced fission of ^{233}U was carried out[5]. In the future, this measurement should be performed by the improved measurement system described above. However, the results of this experiment are consistent to and comparable with the other authors' data[9)-11)]. The mass number, kinetic energy and the number of prompt neutrons are stored on a magnetic disk event by event. With this data set, the inertial excitation energy and deformation energy of the fission fragment at the scission point can be studied and the scission configuration can be analyzed.

References

1) Kanno, I. and Nakagome, Y.: Nucl. Instr. and Meth., **A244**, 551 (1986).
2) Kanno, I. and Nakagome, Y.: Nucl. Instr. and Meth., **A251**, 108 (1986).
3) Schmitt, H. W., Gibson, W. M., Neiler, J. H., Walter, F. J. and Thomas, T. D.: "Proceedings of the Symposium on Physics and Chemistry of Fission", Salzburg, IAEA, Vienna, Vol.I, p.531 (1965).
4) Kanno, I.: Rev. Sci. Instr., in press
5) Kanno, I , Nakagome, Y. and Kimura, I.: Nucl. Sci. Technol., to be published.
6) Mueller, R., Naqvi, A. A., Kaeppeler, F. and Dickmann, F.: Phys Rev., **C29**, 885 (1984).
7) Girard, J, Bolore, M. and Pouthas, J.: Nucl. Instr. and Meth., **198**, 557 (1982).
8) Birks, J. B.: "The Theory and Practice of Scintillation Counting", Macmillan, New York (1964).
9) Milton, J. C. D. and Fraser, J. S.: Can. J. Phys., **40**, 1626 (1962).
10) Bennet, M. J. and Stein, W.: Phys Rev., **156**, 1277 (1967).
11) Pleasonton, F.: Phys. Rev., **174**, 1500 (1968).

Acknowledgements

The author would like to thank Professor Itsuro Kimura of KURRI for his guidance of this study, for his encouragement and for his many helpful suggestions in the course of this study.

The author is deeply indebted to Mr. Yoshihiro Nakagome of KURRI for his guidance in experiments and his suggestion and discussion on theoretical works

The supermirror neutron guide tube was used through the courtesy of Professor Sunao Okamoto and Mr. Tsunekazu Akiyoshi, a lecturer of KURRI. The author also acknowledges the crew of KUR for their support in the experimental work.

The author wish to thank Dr. Takaaki Ohsawa of Kyushu University for his discussion on nuclear physics.

Mr. J. S. Ottaviani, a summer exchange graduate student of KURRI, is appreciated for his advice in English expression.

A part of this study was financially supported by Special Project Research on Energy under Grant-in-Aid of Scientific Research of the Ministry of Education, Science and Culture.

The author appreciates his wife Miyuki for her arrangement of tables, graphs and captions, and encouragement in his life.